Doctoral Dissertation

博士論文

Search for right-handed *W* gauge boson decaying into charged lepton and boosted right-handed neutrino in 139 fb^{-1} of $\sqrt{s} = 13$ TeV proton-proton collisions with the ATLAS detector

(ATLAS検出器における**139 fb^{-1}**の陽子陽子衝突データを用いた
重心系エネルギー13 **TeV**における荷電レプトンと
右巻きの重いニュートリノに崩壊する右巻き***W***ボソン探索**)**

A dissertation Submitted for the Degree of Doctor of Philosophy
December 2022

令和4年12月博士（理学）申請

Department of Physics, Graduate School of Science,
The University of Tokyo
東京大学大学院理学系研究科物理学専攻

Reiyo Oishi
大石　玲誉

Doctoral Dissertation

Search for right-handed W gauge boson decaying into charged lepton and boosted right-handed neutrino in 139 fb^{-1} of $\sqrt{s} = 13$ TeV proton-proton collisions with the ATLAS detector

Reiyo Oishi

The University of Tokyo

Abstract

The standard model (SM) gives a successful description for almost the all phenomena of particle physics. However, there are some problems such as the observation of tiny masses of left-handed neutrinos and baryon dominance in the universe. One possible model which solve these inconsistencies is the left-right symmetric model (LRSM) accompanying right-handed neutrinos N_R and right-handed W boson W_R. A search for W_R decaying into N_R, $pp \to W_\mathrm{R}^\pm \to \ell^\pm N_\mathrm{R} \to \ell^\pm \ell^\pm q q'$, in the framework of LRSM is presented in this thesis.

The analysis is based on a proton-proton collisions data at a center-of-mass energy of 13 TeV collected by the ATLAS detector at the Large Hadron Collider in 2015 - 2018, corresponding to an integrated luminosity of 139 fb^{-1}. The search is performed in both electron and muon final states, using a large-radius jet to reconstruct the decay products from the $N_\mathrm{R} \to \ell q q'$, targeting on the phase space with large mass splitting between W_R and N_R, $\Delta M = m(W_\mathrm{R}) - m(N_\mathrm{R})$. Depending on the ΔM, two analysis strategies are considered in the electron channel; one is to identify the electron from the N_R decay as isolated from the large-radius jet; the other is to reconstruct the $N_\mathrm{R} \to e q q'$ as a single large-radius jet. In the muon channel, two muons are always required, since the higher efficiency can be kept even for large ΔM signals. Event selection, strategies of the dominant background estimations are developed.

No excess is observed in all lepton flavour final states and W_R mass is excluded up to 6.4 TeV for the N_R mass of 1.0 TeV at 95% confidence level. Compared to the previous LHC analyses, it corresponds to the expansion of exclusion limits by 1.5 TeV and 1.4 TeV for electron and muon final states, respectively.

Contents

1 Introduction

The Standard Model (SM) consists of 12 fermions and four gauge bosons which mediate interactions between elementary particles, as well as a Higgs boson which generates the Higgs field and gives some particles mass via the Higgs mechanism. Figure 1.1 shows all elementary particles in the SM [1]. The SM is the most successful theory to describe many experimental results. However, it can not explain some observations and appropriate modifications are required. In this section, first two major problems will be discussed: tiny masses of left-handed neutrinos and baryon asymmetry. Then, right-handed W bosons and right-handed neutrinos as a solution of these problems are introduced.

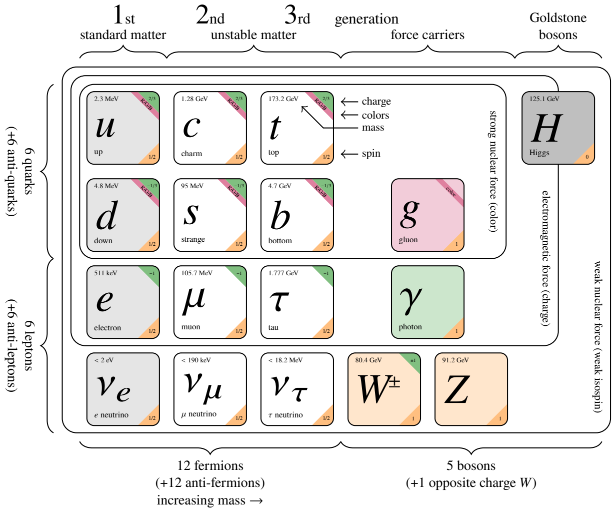

Figure 1.1: Elementary particles in the standard model [2]. The quarks (u, d, c, s, t and b) and leptons (e^-, ν_e, μ^-, ν_μ, τ^- and ν_τ) constitute substance and have spin $1/2$. There are antiparticles of each particle with an opposite charge. The gauge bosons (g, γ, Z, $W^\pm$) are spin 1 particles and mediate interactions between fermions. The Higgs boson (H) is a spin-less particle and generates masses of elementary particles.

1.1 Standard model

SM is a gauge theory that has symmetry with respect to the group $SU(3)_c \times SU(2)_L \times U(1)_Y$. One of the simplest example of a gauge theory is the countless combinations of electromagnetic potential $\mathbf{A}$ and electrostatic potential ϕ that achieve an electric field and a magnetic field satisfying Maxwell's equations with respect to Λ can be prepared as follows:

$$\mathbf{A} \to \mathbf{A}' = \mathbf{A} + \nabla \cdot \mathbf{\Lambda}, \quad \phi \to \phi' = \phi - \frac{\partial \Lambda}{\partial t}.$$

A gauge symmetry in the SM is a symmetry not changing the Lagrangian when the fields representing the particles are modified by certain rules like an unitary transformation.

1.1.1 U(1) gauge transformation

Considering a local gauge transformation for a fermion field $\psi(x)$:

$$\psi(x) \to \psi(x)' = \exp(-iq\alpha(x))\psi(x), \tag{1.1}$$

where $\alpha(x)$ is a function of time and space and can take on different values at different points in space-time. This is a phase transformation **x** and classified as a one dimensional unitary transformation, U(1). For the transformation of equation 1.1, the derivative is also replaced to satisfy the Dirac equation as follows:

$$\partial_\mu \to D_\mu = \partial_\mu + iqA_\mu(x) \tag{1.2}$$

where $A_\mu(x)$ is a gauge field which interacts with the fermion field $\psi(x)$ as follows:

$$\left[i\gamma^\mu \left(\partial_\mu + iqA_\mu(x)\right) - m\right] \psi(x) = 0.$$

For the transformation of the fermion field shown in the equation 1.1, the gauge field A_μ needs to be transformed to restore the Dirac equation as follows:

$$A_\mu(x) \to A'_\mu(x) = A_\mu(x) + \partial_\mu\alpha(x).$$

One significant feature of the gauge field A_μ introduced when assuming U(1) symmetry is that the kinetic term of A_μ is gauge invariant, but the mass term of A_μ is not the case. This predicts that the mass of the particle mediating the interactions related to the U(1) symmetry is exactly zero.

1.1.2 SU(2) gauge transformation

The U(1) gauge transformation is a phase transformation of a field indicating the particle without any change in its flavor. In the weak interaction, two types of fermions are always involved, e.g. the lepton number in beta decay is conserved by a neutrino turning into an electron. The SU(2) transformation is used to describe the reaction of such paired particles. The SU(2) transformation is expressed using three parameters $\boldsymbol{\alpha}$ and a set of Pauli matrices $\boldsymbol{\sigma}$ as follows:

$$\boldsymbol{\alpha} \cdot \boldsymbol{\sigma} = \alpha_1 \begin{pmatrix} 0 & 1 \\ 1 & 0 \end{pmatrix} + \alpha_2 \begin{pmatrix} 0 & -i \\ i & 0 \end{pmatrix} + \alpha_3 \begin{pmatrix} 1 & 0 \\ 0 & -1 \end{pmatrix}.$$

If this matrix is applied to the electron and electron neutrino doublet, this causes mixing:

$$\boldsymbol{\alpha} \cdot \boldsymbol{\sigma} \begin{pmatrix} \psi_{\nu_e} \\ \psi_e \end{pmatrix} = \begin{pmatrix} (\alpha_1 - i\alpha_2)\psi_e + \alpha_3\psi_{\nu_e} \\ (\alpha_1 + i\alpha_2)\psi_{\nu_e} + \alpha_3\psi_e \end{pmatrix}.$$

Then, the gauge transformation in SU(2) is defined as follows:

$$\begin{pmatrix} \psi_{\nu_e} \\ \psi_e \end{pmatrix} \to \begin{pmatrix} \psi'_{\nu_e} \\ \psi'_e \end{pmatrix} = \exp\left(-\frac{i}{2}\boldsymbol{\alpha}(x) \cdot \boldsymbol{\sigma}\right) \begin{pmatrix} \psi_{\nu_e} \\ \psi_e \end{pmatrix}, \tag{1.3}$$

where $\boldsymbol{\alpha(x)}$ is a function of time and space $\mathbf{x}$ and can take on different values at different points in space-time. Assuming that $\alpha(x)$ is small, equation 1.3 is expanded to the first order of α, and the gauge transformation can be written as follows:

$$\begin{pmatrix} \psi_{\nu_e} \\ \psi_e \end{pmatrix} \rightarrow \begin{pmatrix} \psi'_{\nu_e} \\ \psi'_e \end{pmatrix} = \left(1 - \frac{i}{2}\boldsymbol{\alpha}(x) \cdot \boldsymbol{\sigma}\right) \begin{pmatrix} \psi_{\nu_e} \\ \psi_e \end{pmatrix}.$$

The Dirac equation without interaction is not invariant under this gauge transformation, and it is necessary to introduce a covariant derivation D_μ as equation 1.2.

$$\partial_\mu \rightarrow D_\mu = \partial_\mu + \frac{ig}{2}\boldsymbol{W}_\mu(x) \cdot \boldsymbol{\sigma}$$

where g is a coupling constant and $\mathbf{W}_\mu = (W_1, W_2, W_3)$ is a set of the gauge field. The gauge transformation of $\mathbf{W}_\mu$ is defined as follows:

$$W^i_\mu(x) \rightarrow W^{i\prime}_\mu = W^i_\mu + \frac{1}{g}\partial_\mu \alpha_i(x) - \sum_{jk} \epsilon_{ijk} W^j_\mu(x) \alpha_k(x),$$

where ϵ_{ijk} is the structure constants of SU(2). The interaction of the fermion doublet with the gauge field W_μ is invariant. Like the U(1) gauge field, the SU(2) gauge field also requires that the masses of $\mathbf{W}_\mu$ is exactly zero to keep Lagrangian invariant in any SU(2) transformation.

1.1.3 Inconsistency between weak interactions and the SU(2) gauge transformation

The interaction between fermion doubles and gauge fields can be described through the SU(2) gauge transformation. However, the following conditions required by a SU(2) gauge transformation clearly differ from the experimental facts in some aspects.

- Since the SU(2) gauge transformation for the fermion doublet can mix different particles, paired fermions need to have same features, like their masses, to maintain the gauge invariance. This is clearly different from the experimental facts.
- SU(2) gauge invariance requires massless gauge bosons. This means that the interactions can be propagated to infinity distance, but the reach of the weak interaction is short and the masses of the mediating particles need to be heavy.
- The interactions described by the SU(2) with fermion doublets are vector type and conserve parity. However, the weak interaction in reality is a V-A type and the parity is non-conservative.

1.1.4 Glashow-Weinberg-Salam theory

The Glashow-Weinberg-Salam theory [3–5] was proposed as a theory that considers electromagnetic and weak interactions as one gauge theory and is consistent with most of experimental results. This theory is based on a gauge transformation of the direct product of SU(2) and U(1).

1.1.4.1 SU(2) × U(1) gauge transformation

In the SM scope, weak interaction couples to only left-handed doublets and right-handed neutrinos do not exist. Therefore, different gauge transformations are adapted for the left- and right-handed particles. In the following a doublet of the left-handed electron and the electron neutrino and a singlet of the right-handed electron are considered:

$$\begin{aligned} L = \begin{pmatrix} \nu_L \\ e_L \end{pmatrix} = \begin{pmatrix} \frac{1}{2}(1-\gamma_5)\psi_{\nu_e} \\ \frac{1}{2}(1-\gamma_5)\psi_e \end{pmatrix} \rightarrow L' &= \exp\left(-\frac{i}{2}\beta(x)Y\right)\exp\left(-\frac{i}{2}\boldsymbol{\alpha}(x)\cdot\boldsymbol{\sigma}\right)L, \\ &\simeq \left(1-\frac{i}{2}\beta(x)Y-\frac{i}{2}\boldsymbol{\alpha}(x)\cdot\boldsymbol{\sigma}\right)L \\ e_R = \frac{1}{2}(1+\gamma_5)\psi_e \rightarrow e'_R &= \exp\left(-\frac{i}{2}\beta(x)Y\right)e_R \\ &\simeq \left(1-\frac{i}{2}\beta(x)Y\right)e_R, \end{aligned}$$

where Y is called the weak hypercharge and is a generator of U(1) group and $\boldsymbol{\sigma}$ is a set of generator of SU(2) group. The weak hypercharge has the following relationship with charge Q and weak isospin $T^3 \equiv \frac{1}{2}\sigma^3$:

$$Q = T^3 + \frac{Y}{2},$$

The weak hypercharge of L and e_R can be obtained by operating on the charge operator Q and weak isospin T^3 as follows:

$$Q\begin{pmatrix} \nu_L \\ e_L \end{pmatrix} = \begin{pmatrix} 0 \\ -e_L \end{pmatrix}$$

$$T^3\begin{pmatrix} \nu_L \\ e_L \end{pmatrix} = \frac{1}{2}\begin{pmatrix} 1 & 0 \\ 0 & -1 \end{pmatrix}\begin{pmatrix} \nu_L \\ e_L \end{pmatrix} = \frac{1}{2}\begin{pmatrix} \nu_L \\ -e_L \end{pmatrix}$$

Therefore, the weak hypercharge of the left-handed doublet L can be obtained as follows:

$$Y\begin{pmatrix} \nu_L \\ e_L \end{pmatrix} = 2\begin{pmatrix} 0 \\ -e_L \end{pmatrix} - \begin{pmatrix} \nu_L \\ -e_L \end{pmatrix} = -\begin{pmatrix} \nu_L \\ e_L \end{pmatrix}$$

The left-handed doublet is an eigenstate of Y with an eigenvalue of -1. On the other hand, for the right-handed singlet, the eigenvalue of Y is -2 as follows:

$$Qe_R = -e_R, \quad T^3 e_R = 0, \quad 2(Q-T^3)e_R = -2e_R.$$

The gauge fields B_μ and $\mathbf{W}_\mu$ corresponding to the U(1) and SU(2) transformations are introduced. The covariant derivatives are as follows:

$$\begin{aligned} L : \partial_\mu \rightarrow D_\mu &= \partial_\mu + \frac{ig'}{2}B_\mu Y + \frac{ig}{2}\mathbf{W}_\mu\cdot\boldsymbol{\sigma}, \\ e_R : \partial_\mu \rightarrow D_\mu &= \partial_\mu + \frac{ig'}{2}B_\mu Y, \end{aligned}$$

where g and g' are coupling constants for U(1) and SU(2), respectively. The gauge fields are accordingly transformed as follows:

$$\begin{aligned} B_\mu &\longrightarrow B'_\mu = B_\mu + \frac{1}{g'}\partial_\mu\beta, \\ \mathbf{W}_\mu &\longrightarrow \mathbf{W}'_\mu = \mathbf{W}_\mu + \frac{1}{g}\partial_\mu\boldsymbol{\alpha} - \mathbf{W}_\mu\times\alpha. \end{aligned}$$

The SU(2)×U(1) gauge transformation can be performed without changing the following Lagrangian.

$$
\begin{aligned}
\mathcal{L} &= i\bar{L}\gamma^{\mu}\left(\partial_{\mu} + \frac{ig'}{2}B_{\mu}Y + \frac{ig}{2}\mathbf{W}_{\mu}\cdot\boldsymbol{\sigma}\right)L \\
&\quad + i\bar{e}_R\gamma^{\mu}\left(\partial_{\mu} + \frac{ig'}{2}B_{\mu}Y\right)e_R - \frac{1}{4}B_{\mu\nu}B^{\mu\nu} - \frac{1}{4}\mathbf{W}_{\mu\nu}\cdot\mathbf{W}^{\mu\nu} \qquad (1.4) \\
B_{\mu\nu} &= \partial_{\mu}B_{\nu} - \partial_{\nu}B_{\mu} \\
W^{i}_{\mu\nu} &= \partial_{\mu}W^{i}_{\nu} - \partial_{\nu}W^{i}_{\mu} - \sum_{jk}\epsilon_{ijk}W^{j}_{\mu}W^{k}_{\nu}
\end{aligned}
$$

1.1.4.2 Spontaneous symmetry breaking

The gauge invariances corresponding to the electromagnetic and weak interactions require that the mass of the particles representing the gauge fields (gauge particles) are exactly zero. To make the theory more realistic, "Spontaneous symmetry breaking" is introduced. This concept is based on the idea that the Lagrangian, which represents the physical system, is gauge invariant, but the vacuum is not gauge invariant and has a finite expectation value. The Higgs field embodies this idea, and the equations of motion for the gauge particles are modified by the interaction of the vacuum with the Higgs field, as if the gauge particles had finite masses. In the following, the mechanism that gives masses to the gauge particles through the Higgs mechanism is explained.

In the Glashow-Weinberg-Salam theory, a doublet of complex scalar fields ϕ with ϕ^{+} and ϕ^{0} are introduced. The Lagrangian density becomes as follows:

$$\phi = \begin{pmatrix}\phi^{+}\\ \phi^{0}\end{pmatrix},$$

$$\mathcal{L} = -\frac{1}{4}B_{\mu\nu}B^{\mu\nu} - \frac{1}{4}\mathbf{W}_{\mu\nu}\mathbf{W}^{\mu\nu} + (D^{\mu}\phi)^{\dagger}(D_{\mu}\phi) - V(\phi). \qquad (1.5)$$

The third term is the kinetic energy term of the complex scalar field and the fourth term is the potential term. The mass dimension of a scalar field is 1, and in terms of building a renormalizable theory, $V(\phi)$ is generally expressed as follows:

$$V(\phi) = \mu^{2}\phi^{\dagger}\phi + \lambda(\phi^{\dagger}\phi)^{2}.$$

The complex scalar field is decomposed into scalar fields as follows:

$$\phi = \begin{pmatrix}\phi^{+}\\ \phi^{0}\end{pmatrix} = \frac{1}{\sqrt{2}}\begin{pmatrix}\phi^{+}_{R} + i\phi^{+}_{I}\\ \phi^{0}_{R} + i\phi^{0}_{I}\end{pmatrix}.$$

Three of the four scalar fields are used to give finite masses to the three gauge particles mediating the weak interaction, and the remaining one constitutes the Higgs field with finite vacuum expectation value. Thus, this complex scalar field doublet is the minimum requirement to give masses to the gauge particles.

The potential $V(\phi)$ can be expanded using the four scalar fields as follows:

$$V(\phi) = \frac{1}{2}\mu^{2}\left[(\phi^{+}_{R})^{2} + (\phi^{+}_{I})^{2} + \left(\phi^{0}_{R}\right)^{2} + \left(\phi^{0}_{I}\right)^{2}\right] + \frac{1}{4}\lambda\left[(\phi^{+}_{R})^{2} + (\phi^{+}_{I})^{2} + \left(\phi^{0}_{R}\right)^{2} + \left(\phi^{0}_{I}\right)^{2}\right]^{2}.$$

The second term is always positive since every scalar field is real. So the $\lambda > 0$ is required to have a minimum value. When $\mu^2 \geq 0$, this is the case when all four scalar fields have a vacuum expectation value of 0, and the gauge particles can not be given masses. On the other hand, when $\mu^2 < 0$, the potential minima are the case shown below:

$$\left(\phi_R^+\right)^2 + \left(\phi_I^+\right)^2 + \left(\phi_R^0\right)^2 + \left(\phi_I^0\right)^2 = \frac{-\mu^2}{\lambda}.$$

At this stage, the four scalar fields are equivalent and there is a degree of freedom for scalar field transformation. However, if the vacuum state is the gauge transformed so that one scalar field has a vacuum expectation value $v = \sqrt{-\mu^2/\lambda}$, the symmetry that existed between scalar fields is broken. This is called spontaneous symmetry breaking.

1.1.4.3 Higgs mechanism

Gauge particles gain masses by interacting with the Higgs field, so mass terms appear in the kinetic energy term in equation 1.5:

$$\begin{aligned}
(D^\mu\phi)^\dagger(D_\mu\phi) &= \frac{1}{2}(0, v)\left(\frac{g'}{2}B_\mu + \frac{g}{2}\mathbf{W}_\mu \cdot \boldsymbol{\sigma}\right)\begin{pmatrix}0\\v\end{pmatrix} \\
&= \frac{g^2v^2}{8}\left(W^{1\mu} - iW^{2\mu}\right)\left(W^1_\mu + iW^2_\mu\right) + \frac{v^2}{8}\left(gW^{3\mu} - g'B^\mu\right)\left(gW^3_\mu - g'B_\mu\right) \\
&= \frac{1}{2}M_W 2\left(W^{+\mu}W^-_\mu + W^{-\mu}W^+_\mu\right) + \frac{1}{2}M_Z^2 Z^\mu Z_\mu.
\end{aligned}$$

The quantities corresponding to the gauge fields $W^\pm_\mu, Z_\mu$ and a mass-less gauge field for a photon A_μ which is defined as the orthogonality field with respect to Z_μ and masses M_W, M_Z are defined as follows:

$$W^\pm_\mu = \frac{1}{\sqrt{2}}\left(W^1_\mu \mp iW^2_\mu\right), \quad Z_\mu = \frac{gW^3_\mu - g'B_\mu}{\sqrt{g^2 + g'^2}}, \quad A_\mu = \frac{g'W^3_\mu + gB_\mu}{\sqrt{g^2 + g'^2}},$$

$$M_W = \frac{gv}{2}, \quad M_Z = \frac{\sqrt{g^2 + g'^2}v}{2}.$$

The gauge invariance requires that the mass of the gauge particles should be zero. The gauge particles are vector bosons with spin 1 and have two degree of freedom. However, in the interaction with the Higgs field, having masses restores one degree of freedom. This can be interpreted as the absorption of three of four degrees of freedom possessed by the complex scalar field. The other one degree makes non-zero vacuum expectation value. Such a mechanism is called Higgs mechanism.

1.1.4.4 Interactions with leptons

The interactions between leptons and gauge fields can be found in equation 1.4. Rewriting B_μ and W^3_μ in terms of the A_μ which is formed by a photon and Z_μ which is formed by a neutral weak gauge particle, the result is as follows:

$$
\begin{aligned}
\mathcal{L} &= i\bar{L}\gamma^\mu\left(\frac{ig'}{2}B_\mu Y + \frac{ig}{2}\boldsymbol{W}_\mu\cdot\boldsymbol{\sigma}\right)L + i\bar{e}_R\gamma^\mu\frac{ig'}{2}B_\mu Y e_R \\
&= -\frac{1}{2}\bar{\nu}_L\gamma^\mu\left(\frac{gg'(Y+1)}{\sqrt{g^2+g'^2}}A_\mu - \frac{g'^2Y-g^2}{\sqrt{g^2+g'^2}}Z_\mu\right)\nu_L \\
&\quad -\frac{1}{2}\bar{e}_L\gamma^\mu\left(\frac{gg'(Y-1)}{\sqrt{g^2+g'^2}}A_\mu - \frac{g'^2Y+g^2}{\sqrt{g^2+g'^2}}Z_\mu\right)e_L \\
&\quad -\frac{1}{2}\bar{e}_R\gamma^\mu\left(\frac{gg'Y}{\sqrt{g^2+g'^2}}A_\mu - \frac{g'^2Y}{\sqrt{g^2+g'^2}}Z_\mu\right)e_R \\
&\quad -\frac{g}{\sqrt{2}}\left(\bar{\nu}_L\gamma^\mu W_\mu^+ e_L + \bar{e}_L\gamma^\mu W_\mu^- \nu_L\right).
\end{aligned}
\tag{1.6}
$$

Substituting the value of the weak hypercharge and defining the coupling constant between an electron and a photon as e, the relation between e and g, g' is as follows:

$$
e = \frac{gg'}{\sqrt{g^2+g'^2}} = g\sin\theta_W,
$$

where θ_W is known as the Weinberg angle and represents the mixing of the U(1) and SU(2) gauge transformations. The Lagrangian density of equation 1.6 is summarized for each gauge field as follows:

$$
\begin{aligned}
\mathcal{L} &= -\left[-e\left(\bar{e}\gamma^\mu e\right)\right]A_\mu \\
&\quad -\frac{g}{2\cos\theta_W}\left[\bar{\nu}\gamma^\mu\frac{1-\gamma_5}{2}\nu + \bar{e}\gamma^\mu\left(2\sin^2\theta_W - \frac{1-\gamma_5}{2}\right)e\right]Z_\mu \\
&\quad -\frac{g}{\sqrt{2}}\left(\bar{\nu}\gamma^\mu\frac{1-\gamma_5}{2}eW_\mu^+ + \bar{e}\gamma^\mu\frac{1-\gamma_5}{2}\nu W_\mu^-\right).
\end{aligned}
$$

The first term represents the interaction between the electron current and photon A_μ (electromagnetic interaction). Photons couple with the same strength regardless of whether they are left-handed or right-handed. Neutrinos have no charge and do not couple to photons. The second term is the coupling between leptons and the neutral weak boson Z. It represents the weak interaction involving the current, which does not change its charge. The third term represents a weak interaction that changes charge and couples to the charged weak boson $W^\pm$. It can be seen that the charged weak interaction is not present only in the left-handed component, whereas the neutral weak interaction also contributes to the right-handed component.

Similar to gauge particles, fermion masses can be produced by interactions with the Higgs field. The following Lagrangian density is assumed for the interaction of electrons with the Higgs field [5]:

$$
\mathcal{L} = -g_e\left(\overline{L}\phi e_R + \overline{e}\phi^\dagger L\right),
\tag{1.7}
$$

where g_e indicates the coupling constant between an electron and the Higgs field, which is called the Yukawa coupling. Using the vacuum expectation value of the complex scalar field that constitutes the SU(2) doublet, equation 1.7 is expanded as follows:

$$
\begin{aligned}
\mathcal{L} &= -\frac{g_e}{\sqrt{2}}\left[\left(\overline{\nu}_L, \overline{e}_L\right)\begin{pmatrix}0\\ v\end{pmatrix}e_R + \overline{e}_R(0, v)\begin{pmatrix}\nu_L\\ e_L\end{pmatrix}\right] \\
&= -\frac{g_e v}{\sqrt{2}}\left(\overline{e}_L e_R + \overline{e}_R e_L\right) = -\frac{g_e v}{\sqrt{2}}\overline{e}e.
\end{aligned}
$$

The parameter g_e is related to the electron mass m_e by the following equation:

$$m_e = \frac{g_e v}{\sqrt{2}}. \tag{1.8}$$

From equation 1.8, the coupling constant between fermions and the Higgs field has a liner relation with their masses.

1.1.5 SU(3) gauge transformation

The SU(2) gauge transformation is that of a field describing the particles mediating the weak interactions. In the strong interaction, three states of a certain fermion are involved. The SU(3) transformation is used to describe the reaction among such states. The SU(3) transformation is expressed using eight parameters $\boldsymbol{\alpha}$ and a set of Gell-Mann matrices $\boldsymbol{\lambda}$ as follows:

$$\begin{aligned}\boldsymbol{\alpha}\cdot\frac{1}{2}\boldsymbol{\lambda} &= \frac{\alpha_1}{2}\begin{pmatrix}0&1&0\\1&0&0\\0&0&0\end{pmatrix}+\frac{\alpha_2}{2}\begin{pmatrix}0&-i&0\\i&0&0\\0&0&0\end{pmatrix}+\frac{\alpha_3}{2}\begin{pmatrix}1&0&0\\0&-1&0\\0&0&0\end{pmatrix}+\frac{\alpha_4}{2}\begin{pmatrix}0&0&1\\0&0&0\\1&0&0\end{pmatrix}\\ &+\frac{\alpha_5}{2}\begin{pmatrix}0&0&-i\\0&0&0\\i&0&0\end{pmatrix}+\frac{\alpha_6}{2}\begin{pmatrix}0&0&0\\0&0&1\\0&1&0\end{pmatrix}+\frac{\alpha_7}{2}\begin{pmatrix}0&0&0\\0&0&-i\\0&i&0\end{pmatrix}+\frac{\alpha_8}{2\sqrt{3}}\begin{pmatrix}1&0&0\\0&1&0\\0&0&-2\end{pmatrix}.\end{aligned}$$

The gauge transformation in SU(3) is defined as follows:

$$\begin{pmatrix}\psi_R\\\psi_G\\\psi_B\end{pmatrix}\rightarrow\begin{pmatrix}\psi'_R\\\psi'_G\\\psi'_B\end{pmatrix}=\exp\left(-\frac{i}{2}\boldsymbol{\alpha}(x)\cdot\frac{1}{2}\boldsymbol{\lambda}\right)\begin{pmatrix}\psi_R\\\psi_G\\\psi_B\end{pmatrix} \tag{1.9}$$

where $\boldsymbol{\alpha}$ is a function of time and space $\mathbf{x}$ and can take on different values at different points in space-time and R, G, B are a quantity exchanged by the strong interaction and are called color charge. Assuming that $\alpha(x)$ is small, equation 1.9 is expanded to the first order of α, and the gauge transformation can be written as follows:

$$\begin{pmatrix}\psi_R\\\psi_G\\\psi_B\end{pmatrix}\rightarrow\begin{pmatrix}\psi'_R\\\psi'_G\\\psi'_B\end{pmatrix}=\left(1-\frac{i}{2}\boldsymbol{\alpha}(x)\cdot\frac{1}{2}\boldsymbol{\lambda}\right)\begin{pmatrix}\psi_R\\\psi_G\\\psi_B\end{pmatrix}.$$

It is necessary to introduce a following covariant derivative to restore the Dirac equation:

$$\partial_\mu \rightarrow D_\mu = \partial_\mu - \frac{ig}{2}\mathbf{G}^a_\mu(x)\cdot\boldsymbol{\lambda}^a,$$

where g is a strong coupling constant and $\mathbf{G}_\mu = (G_1, G_2, G_3, G_4, G_5, G_6, G_7, G_8)$ is a set of the gauge field. They are called gluons. The gauge transformation of $\boldsymbol{G}_\mu$ is defined as follows:

$$G^i_\mu(x) \rightarrow G^{i\prime}_\mu(x) = G^i_\mu(x) + \frac{1}{g}\partial_\mu\epsilon^i - \sum_{jk} f_{ijk}G^j_\mu(x)\epsilon_k(x),$$

where f_{ijk} is the structure constants of SU(3). The interaction of the fermion triplet with the gauge field $\boldsymbol{G}_\mu$ is invariant. The masses of $\boldsymbol{G}_\mu$ is exactly zero to keep Lagrangian invariant in any SU(3) transformation.

1.2 Remaining problems

1.2.1 Finite masses of the left-handed neutrinos

One of the most important properties of neutrinos is neutrino oscillation to change the neutrino flavors associated with the passage of time. Neutrinos were thought to be mass-less particles in the SM. However, observation of neutrino oscillations unveiled their finite masses [6, 7]. In the following, the necessity of neutrino masses is discussed with the Schrödinger picture if the neutrino oscillation exist.

The flavor eigenstates of neutrinos $|\nu_\alpha\rangle$ $(\alpha = e, \mu, \tau)$ can be expressed as linear functions of mass eigenstates $|\nu_i\rangle$ $(i = 1, 2, 3)$ with a 3×3 unitary matrix U which is called Pontecorvo-Maki-Nakagawa-Sakata (PMNS or simply MNS) matrix [8, 9] as follows:

$$|\nu_\alpha\rangle = \sum_{i=1}^{3} U_{\alpha i}|\nu_i\rangle. \tag{1.10}$$

Since the PMNS matrix is unitary, there are nine independent parameters in total. Three of them are rotation angle parameters $(\theta_{12}, \theta_{13}, \theta_{23})$. Others are phase parameters, but if neutrinos are Dirac particles, five out of six parameters can be absorbed by the phase of left-handed leptons because they do not have mass terms in the Lagrangian. The remaining phase parameter δ is known as the Dirac CP phase. Whereas, in the case of Majorana neutrinos, due to the loss of a degree of freedom for left-handed neutrinos, two additional phase parameters, λ_1 and λ_2 which are known as Majorana CP phases, remain. With these parameters, the PMNS matrix can be written as follow.

$$\boldsymbol{U} = \begin{pmatrix} c_{12}c_{13} & c_{13}s_{12} & e^{-i\delta}s_{13} \\ -c_{23}s_{12} - e^{i\delta}c_{12}s_{13}s_{23} & c_{12}c_{23} - e^{i\delta}s_{12}s_{13}s_{23} & c_{12}s_{23} \\ s_{12}s_{23} - e^{i\delta}c_{12}c_{23}s_{13} & -e^{i\delta}c_{23}s_{12}s_{13} - c_{12}s_{23} & c_{13}c_{23} \end{pmatrix} \begin{pmatrix} e^{i\lambda_1} & 0 & 0 \\ 0 & e^{i\lambda_2} & 0 \\ 0 & 0 & 1 \end{pmatrix},$$

where $c_{ij} = \cos\theta_{ij}$ and $s_{ij} = \sin\theta_{ij}$.

The time evolution of a mass eigenstate can be written as:

$$\begin{aligned} i\frac{d}{dt}|\nu_i(t)\rangle &= \mathcal{H}|\nu_i(t)\rangle = E_i|\nu_i(t)\rangle \\ |\nu_i(t)\rangle &= exp(-iE_it)|\nu_i(0)\rangle, \end{aligned}$$

where $\mathcal{H}$ and E_i are the Hamiltonian and expected energy of mass eigenstate $|\nu_i\rangle$. Hence, from equation 1.10, the flavor eigenstate $|\nu_\alpha\rangle$ at a time t can be written as:

$$|\nu_\alpha(t)\rangle = \sum_i U_{\alpha i}\exp(-iE_it)|\nu_i(0)\rangle \tag{1.11}$$

In the case of the ultra-relativistic limit, E_i can be expressed as:

$$E_i = \sqrt{p_i^2 + m_i^2} \sim p_i + \frac{m_i^2}{2E_i},$$

hence, equation 1.11 becomes as follows:

$$|\nu_\alpha(t)\rangle = \sum_i U_{\alpha i}\exp(-ip_it)\exp\left(-\frac{im_i^2t}{2E_i}\right)|\nu_i(0)\rangle.$$

As the same analogy, the flavor eigenstate $\langle \nu_\beta(t')|$ at a time t' becomes as follows:

$$\langle \nu_\beta(t')| = \sum_j U^\dagger_{\beta j} \exp(ip_j t') \exp\left(\frac{im_j^2 t'}{2E_j}\right) \langle \nu_j(0)|$$

The transition amplitude $\langle \nu_\beta(t')|\nu_\alpha(t)\rangle$ can be decomposed to be:

$$\langle \nu_\beta(t')|\nu_\alpha(t)\rangle = \sum_i U_{\alpha i} U^\dagger_{\beta i} \exp\left[-ip_i(t-t')\right] \exp\left[-\frac{im_i^2(t-t')}{2E_i}\right]$$

The $\nu_\alpha(0) \longrightarrow \nu_\beta(t)$ transition probability $P(\nu_\alpha(0) \longrightarrow \nu_\beta(t))$ is calculated below:

$$\begin{aligned}
P(\nu_\alpha(0) \longrightarrow \nu_\beta(t)) &= |\langle \nu_\beta(t)|\nu_\alpha(0)\rangle|^2 \\
&= \left|\sum_i U_{\alpha i} U^\dagger_{\beta i} \exp(ip_i t) \exp\left(\frac{im_i^2 t}{2E_i}\right)\right|^2 \\
&= \sum_i \sum_j U_{\alpha i} U^\dagger_{\beta i} U^\dagger_{\alpha j} U_{\beta j} \exp[i(p_i - p_j)t] \exp\left[i\left(\frac{m_i^2}{2E_i} - \frac{m_j^2}{2E_j}\right)t\right] \\
&= \sum_i \sum_j U_{\alpha i} U^\dagger_{\beta i} U^\dagger_{\alpha j} U_{\beta j} \exp\left(\frac{i\Delta_{ij} t}{2E}\right),
\end{aligned}$$

where $\Delta_{ij} \equiv m_i^2 - m_j^2$ is a mass squared difference. In the above calculation, it is assumed that the momentum and energy of all mass eigenstates are the same. According to this equation, neutrino oscillation can occur only when there is a non-zero mixing angle ($\theta_{ij} \neq 0$) and at least two neutrino masses are not degenerated ($m_i \neq m_j$).

Since there are no right-handed neutrinos in the SM, the Dirac mass term can not be formed. If the neutrino masses are derived from unknown physics at the Planck scale, it is too small compared to the observations of neutrino oscillations. Physics at a scale smaller than the Planck scale is needed. In section 1.3, heavy right-handed neutrinos are introduced at a moderate energy scale and they leads to the derivation of masses of the left-handed neutrinos.

1.2.2 Baryon asymmetry

The constituents of the current universe are made up of matter with little anti-matter and observations of cosmic background radiations have led to a detailed investigation of the baryon dominance in the university. As conditions for generating non-zero baryon numbers, the following three conditions, known as the Sakharov conditions [10], are required to produce the matter and anti-matter imbalance.

1. **Baryon number violation**
   The initial condition of the baryon number is 0. The baryon number violation is needed to produce the baryon asymmetry.
2. **C-symmetry and CP-symmetry violation**
   If the C- or CP-symmetry is preserved, the amount of a certain matter is the same as one of its anti-matter.

3. **Interactions out of thermal equilibrium**
   Under conditions of a perfect thermal equilibrium, since the particles and anti-particles have the same mass due to CPT-invariance, the counter-reaction of the condition 1 above also occurs in the same amount, so the matter and anti-matter are present in the same amount and can not make the baryon asymmetry.

A model called an electroweak baryogenesis [11, 12] is an attempt to explain the baryon number dominance within the framework of the SM. The baryon number is broken by the effect of quantum anomalies, and the C- and CP-symmetry are broken by the weak interactions. However, the third condition of interactions out of thermal equilibrium, can not be explained. The CP violation is also too small to explain the production of sufficient baryon number. Therefore, a theory beyond the SM must be required to enhance CP violation and explain the deviation from thermal equilibrium.

In the following, the relation between the baryon number and the lepton number and the lepton number violation which indirectly induces the baryon number violation are explained. Furthermore, the necessity for left-handed and right-handed particles to interact with different fields is also explained.

Baryon and lepton currents are defined as follows:

$$\begin{aligned} j_B^\mu &= \frac{1}{3}\sum_{i=1}^{3}(\overline{Q_L}\gamma^\mu Q_L + \overline{q_R^U}\gamma^\mu q_R^U + \overline{q_R^D}\gamma^\mu q_R^D) \\ j_L^\mu &= \sum_{i=1}^{3}(\overline{L_L}\gamma^\mu L_L + \overline{l_R}\gamma^\mu l_R) \end{aligned}$$

where Q_L and L_L is a quark and lepton doublet, respectively. q_R^U, q_R^D and l_R is a singlet of a quark and lepton as follows:

$$Q_L = \begin{pmatrix} u_L \\ d_L \end{pmatrix}, \quad q_R^U = u_R, \quad q_R^D = d_R, \quad L_L = \begin{pmatrix} e_L \\ \nu_{e_L} \end{pmatrix}, \quad l_R = e_R.$$

By using the Dirac and adjoint Dirac equations, the preservation of a current of a spinor ψ can be proven:

$$\begin{aligned} \partial_\mu(\overline{\psi}\gamma^\mu\psi) &= (\partial_\mu\overline{\psi})\gamma^\mu\psi + \overline{\psi}\partial_\mu\gamma^\mu\psi \\ &= \overline{\psi}\overleftarrow{\not{\partial}}\psi + \overline{\psi}\not{\partial}\psi \\ &= im\overline{\psi}\psi - im\overline{\psi}\psi = 0. \end{aligned}$$

Hence, the baryon and lepton currents are also preserved and the baryon number B and lepton numbers L given by equation 1.12 are also preserved in classical fields,

$$B \equiv \int d^3x j_B^0 \quad , L \equiv \int d^3x j_L^0. \tag{1.12}$$

However, due to a quantum anomaly [13], such a conservation law is broken and the baryon and lepton currents are not preserved in quantized fields as follows:

$$\partial_\mu j_B^\mu = \partial_\mu j_L^\mu = \frac{N_g}{32\pi^2}g^2\left\{F_{\mu\nu}(L)\tilde{F}^{\mu\nu}(L) - F_{\mu\nu}(R)\tilde{F}^{\mu\nu}(R)\right\},$$

where N_g is three which corresponds to the number of fermion families, g indicates a coupling constant which is assumed to be common for both left- and right-handed interactions and $F_{\mu\nu}(L)$ and $F_{\mu\nu}(R)$ are the field strength coupling to left-handed and right-handed particles, respectively. From the above equation, it is clear that $B - L$ is preserved. In case both left and right-handed particles are connected to the same gauge field, like QED and QCD, this quantum anomaly vanished. Therefore, the minimum extension to achieve baryon and lepton number violation to the SM is to introduce the weak interaction to right-handed particles and couple them with different fields from the left-handed one.

Above a phase transition temperature where the separation of the electromagnetic and weak interactions occurs, the cross-section of the process that exchanges lepton and baryon numbers, known as the sphaleron process [14], increases rapidly. Therefore, the baryon-dominated universe is also explained by creating lepton numbers and converting them to baryon numbers.

1.3 Right-handed neutrinos

While preserving the gauge symmetry of the SM, right handed neutrinos ν_R are introduced as follows:

$$\begin{aligned}
\mathcal{L} &= \mathcal{L}_{\text{SM}} + \mathcal{L}_{\nu_R,\text{kinematics}} + \mathcal{L}_{\nu_R,\text{mass}} \\
\mathcal{L}_{\nu,\text{kinematics}} &= \overline{\nu_R} i \partial\!\!\!/ \nu_R \\
\mathcal{L}_{\nu,\text{mass}} &= -y_\alpha \overline{L_L}_\alpha \Phi \nu_{R\alpha} - \frac{M_R}{2} \overline{\nu_R^c} \nu_R + h.c.
\end{aligned}$$

The first term of $\mathcal{L}_{\nu,\text{mass}}$ is the Dirac mass term coming from the vacuum expectation value (VEV) of the Higgs field Φ. The second term is the Majorana mass term and M_R is a mass scale independent of the VEV. The Majorana mass term is not necessarily required to explain neutrino masses but is essential to explain the baryon-dominated universe from the lepton number breaking.

The Seesaw mechanism [15–17] naturally accounts for tiny masses of left-handed neutrinos. Here, let us assume the case of a single neutrino generation. The neutrino mass term can be written as follows:

$$-\mathcal{L}_{\nu,\text{mass}} = \frac{1}{2} \begin{pmatrix} \overline{\nu_L} & \nu_R^c \end{pmatrix} \begin{pmatrix} 0 & m_L \\ m_L & M_R \end{pmatrix} \begin{pmatrix} \nu_L^c \\ \nu_R \end{pmatrix} + h.c.$$

Eigenvalues of the above mass matrix are:

$$\lambda = \frac{1}{2} \left(M_R \pm \sqrt{M_R^2 - 4m_L^2} \right). \tag{1.13}$$

Assuming that M_R has a very high energy scale compared to m_L, equation 1.13 becomes as follows:

$$\begin{aligned}
m_\nu &= -\frac{m_L^2}{M_R}(1 + \mathcal{O}(\theta^2)) \\
M_N &= M_R(1 + \mathcal{O}(\theta^2))
\end{aligned}$$

where θ is m_L/M_R. The m_ν and M_N correspond to the mass of a left-handed and a right-handed neutrino, respectively. The larger the M_N the smaller the m_ν is, hence this mechanism is called the Seesaw mechanism. In the above explanation, right-handed neutrinos are assumed to be gauge singlets. This scenario is called the Type-I seesaw mechanism. However, right-handed neutrinos do not have to be gauge singlets. For example, some models introduce SU(2) triplet scalars or fermions, which are called Type-II [18, 19] and Type-III [20] seesaw mechanisms, respectively.

As shown in Section 1.2.2, baryon asymmetry can be explained in terms of the lepton number breaking. In particular, the lepton number breaking scenario due to the decay of heavy right-handed neutrinos is called the leptogenesis [21]. Since right-handed neutrinos are Majorana particles and antiparticles of them are identical to themselves, they can produce lepton numbers. A part of these lepton numbers is converted to baryon numbers via the sphaleron process.

There is no limit on the number of generations of the right-handed neutrinos, but when considering theoretical models that follow a larger group than the SM, the number of generations for right-handed neutrinos is probable to be also three, as for left-handed neutrinos.

1.4 Target N_R and W_R particles

The Left-Right Symmetric Model [15, 17, 22–28] (LRSM) is based on the following gauge group:

$$G_\mathrm{LRSM} = SU(2)_L \times SU(2)_R \times U(1)_{\tilde{Y}}, \tag{1.14}$$

plus a symmetry between the left and right sectors. Quarks and leptons are completely left-right symmetric

$$Q_{L,R} = \begin{pmatrix} u \\ d \end{pmatrix}_{L,R}, \quad L_{L,R} = \begin{pmatrix} \nu \\ e \end{pmatrix}_{L,R},$$

where ν_R represents a right-handed neutrino. The U(1) gauge group has a charge $\tilde{Y}$ different to the standard model hypercharge. Relation between the charge and the weak hypercharge expressed in equation 1.1.4.1 in SM is modified by adding $SU(2)_R$ group as follows:

$$Q = T_L^3 + T_R^3 + \frac{\tilde{Y}}{2},$$

where T_L^3 and T_R^3 is the third generator of $SU(2)_L$ and $SU(2)_R$, respectively. Similar to the equation 1.1.4.1, the weak hypercharge $\tilde{Y}$ is obtained for L_L and Q_L as follows:

$$\tilde{Y}L_L = \tilde{Y}\begin{pmatrix} \nu_L \\ e_L \end{pmatrix} = 2\begin{pmatrix} 0 \\ -e_L \end{pmatrix} - \begin{pmatrix} \nu_L \\ -e_L \end{pmatrix} = -\begin{pmatrix} \nu_L \\ e_L \end{pmatrix},$$

$$\tilde{Y}Q_L = \tilde{Y}\begin{pmatrix} u_L \\ d_L \end{pmatrix} = 2\begin{pmatrix} \frac{2}{3}u_L \\ -\frac{1}{3}d_L \end{pmatrix} - \begin{pmatrix} u_L \\ -d_L \end{pmatrix} - \begin{pmatrix} 0 \\ 0 \end{pmatrix} = \frac{1}{3}\begin{pmatrix} u_L \\ d_L \end{pmatrix}.$$

These equations imply that $\tilde{Y} = B - L$ and LRSM adapts it as the charge of $U(1)$ group.

The SM introduces a symmetric complex scalar field doublet which is spontaneously broken and gives a non-zero vacuum expectation value. Consequently weak bosons get finite masses. The LRSM, on the other hand, introduces two complex fields scalar triplets $\Delta_L \in (1_L, 3_R, 2), \Delta_R \in (1_L, 3_R, 2)$ and a bi-doublet $\Phi \in (2_L, 2_R, 0)$ [29], according to the gauge group of equation 1.14:

$$\Phi = \begin{bmatrix} \phi_1^0 & \phi_2^+ \\ \phi_1^- & \phi_2^0 \end{bmatrix}, \quad \Delta_{L,R} = \begin{bmatrix} \Delta^+/\sqrt{2} & \Delta^{++} \\ \Delta^0 & -\Delta^+/\sqrt{2} \end{bmatrix}_{L,R},$$

One of the complex triplets gives masses to the right-handed weak bosons and the other one for left-handed weak bosons. The vacuum expectation value of the right-handed triplet is large than the left-handed one, resulting right-handed weak bosons having much larger masses than the SM weak bosons.

The spontaneously symmetry breaking in LRSM is done with two steps. At the first stage of the breaking, according to [29], the G_{LRSM} downs to the $SU(2)_L \times U(1)$ group:

$$\langle \Delta_L \rangle = 0, \quad \langle \Delta_R \rangle = \begin{bmatrix} 0 & 0 \\ v_R & 0 \end{bmatrix}.$$

At the next stage, the neutral components Φ develop a vacuum expectation value and break the $SU(2)_L \times U(1)$ down to $U(1)_{\text{EM}}$ group:

$$\langle \Phi \rangle = \begin{bmatrix} v_1 & 0 \\ 0 & v_2 \end{bmatrix},$$

where $v_{1,2}$ are real and positive, $M_W^2 = g^2 v^2 \equiv g^2(v_1^2 + v_2^2)$ and $g \equiv g_L = g_R$ denotes the SU(2) gauge coupling constants. In turn, Δ_L develops a tiny vacuum expectation value $\langle \Delta_L \rangle \propto v^2/v_R$.

The right-handed gauge boson masses are expressed as follows [30]:

$$\begin{aligned} M_{W_{\text{R}}}^2 &\simeq g^2 v_R^2, \\ M_{Z_R}^2 &\simeq 2(g^2 + g_{B-L}^2) v_R^2 \simeq 3 M_{W_{\text{R}}}^2. \end{aligned} \tag{1.15}$$

As shown in equation 1.15, the mass of the right-handed Z boson is heavier than the right-handed W boson ($M_{Z_R} \simeq 1.7 M_{W_{\text{R}}}$), and the W_{R} mass limit is more important for LRSM. In the above, the mixing of the left- and right-handed gauge bosons, which is expressed as a product of vacuum expectation values of v_1 and v_2, is not taken into account.

The target of this thesis searches for the production of the heavy right-handed bosons with the subsequent decay to the final state containing two charged SM leptons and two quarks: $W_{\text{R}} \rightarrow N_{\text{R}}\ell \rightarrow W_{\text{R}}^* \ell\ell \rightarrow \ell\ell jj$ (i.e. Keung-Senjanović process [31] in Figure 1.2). The left-right mixing is not considered and N_{R} is produced as an intermediate state in the decay of W_{R}. When $m(W_{\text{R}}) > m(N_{\text{R}})$, the on-shell W_{R} mass can be reconstructed from the invariant mass of the $\ell\ell jj$ system. Alternatively, when $m(W_{\text{R}}) < m(N_{\text{R}})$, the second W_{R} in the decay chain is on-shell and can be reconstructed from the invariant mass of the jj system.

If the N_{R} are Majorana particles, N_{R} can account for the masses of the known neutrinos via the Type-I Seesaw mechanism. In the Type-I Seesaw mechanism within LRSM, masses of the N_{R} are coupled to the ν_L masses through a mixing matrix. In minimum Seesaw mechanisms, the right-handed bosons typically have a mass around the Grand Unification Scale, but particular parameter values can be found where N_{R} and W_{R} can have masses in the GeV-TeV range, i.e. within the energy reach of the LHC. The Type-I Seesaw mechanism requires both the known ν_L and hypothetical N_{R} to be Majorana particles, allowing lepton number violating processes.

The decay chain considered in this analysis is below:

$$pp \rightarrow W_{\text{R}} \rightarrow \ell N_{\text{R}} \rightarrow \ell\ell q q'.$$

In the following, a lepton produced from W_{R} decay is named leading lepton and one produced from N_{R} decay is named sub-leading lepton. In this analysis, the case where the W_{R} has a large mass and a small momentum is considered, so the leading lepton has a larger momentum. The lepton flavors considered in this thesis are electron and muon, and no flavor mixing is assumed.

In case the N_{R} is a Majorana particle, 50 % of events have the same-sign lepton pair. On the other hand, assuming a Dirac particle, the opposite-sign lepton pair is ideally expected in all events. The actual

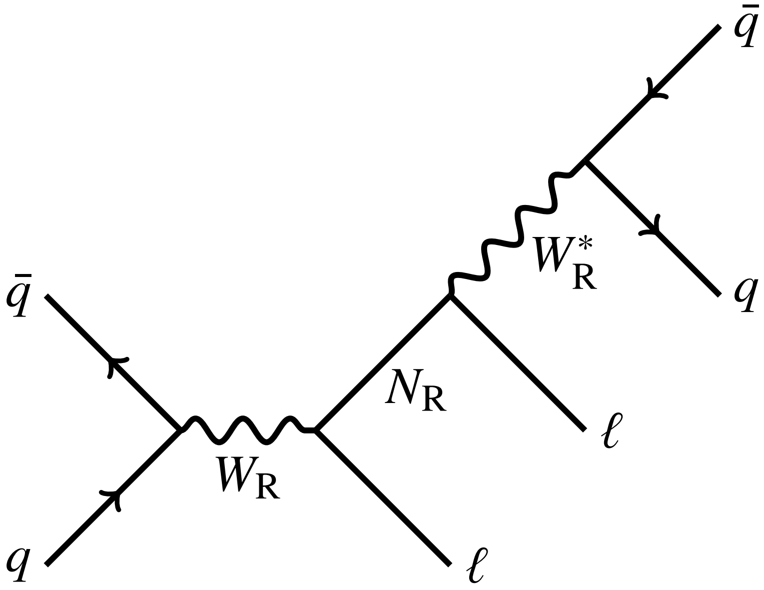

Figure 1.2: Feynman diagram for the Keung-Senjanović process [31], shown for the $m(W_R) > m(N_R)$ case. For the inverted mass hierarchy, first W_R in the decay chain is off-shell (as shown by a * in the second W_R above), rather than the second one.

analysis is performed assuming that the N_R is a Majorana particle, and the case of a Dirac particle is also interpreted.

The characteristic signature at the detector depends on the balance between the mass of the W_R and N_R; if W_R and N_R have similar masses, all final state particles are reconstructed separately, which is called "resolved" analysis. On the other hand, if $W_R > N_R$ case, the two quarks from off-shell W_R are recognized as a single jet by boosting N_R, resulting in an event with two leptons and one large-R jet, which is called "boosted" analysis. In the boosted analysis, hadrons from N_R decay are reconstructed as a single large-radius (large-R) jet. This thesis focuses on boosted analyses.

1.5 Previous and future experimental constrains

1.5.1 Results of the ATLAS and CMS analysis

Searches in the boosted channels have been performed by ATLAS [32–34] and CMS [35–38]. The latest exclusion limits for electron and muon final states by ATLAS (80 fb^{-1}) are shown in Figure 1.3, and CMS (138 fb^{-1}) in Figure 1.4. In both ATLAS and CMS analyses, the sensitivity in the electron channel was lower than the muon channel in the large $\Delta M = m(W_R) - m(N_R)$ region for example the mass point $(m(W_R), m(N_R)) = (5\text{ TeV}, 100\text{ GeV})$ was not covered in electron channel. This was because the reconstruction efficiency of the electron from the N_R decay is dropped in this mass region due to hadron activities closeby the sub-leading electron.

In both the ATLAS and CMS analyses, the number of observed data in the electron channels exceeded the number of backgrounds estimated using MC. The global significance for ATLAS and CMS was 2.4σ and 2.8σ, respectively.

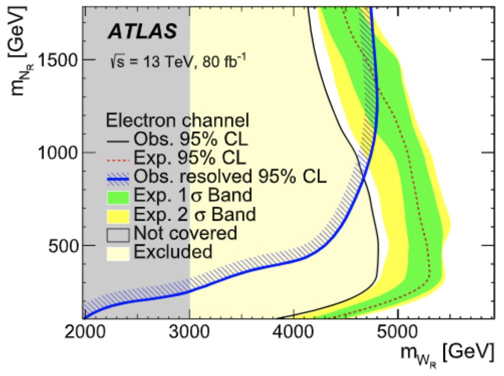

(a) Electron final state

(b) Muon final state

Figure 1.3: Observed (black solid line) and expected (red dashed line) at 95 % confidence level in the $m(W_\mathrm{R})$ and $m(N_\mathrm{R})$ 2-D plane by ATLAS in electron (a) and muon (b) final state for boosted topology. The exclusion limits with resolved topology are overlaid by the blue line [34].

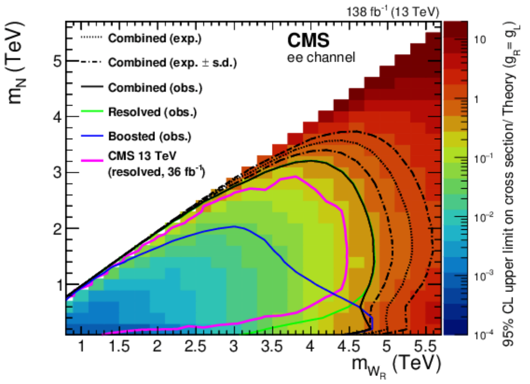

(a) Electron final state

(b) Muon final state

Figure 1.4: Observed (black solid line) and expected (black dashed line) at 95 % confidence level in the $m(W_\mathrm{R})$ and $m(N_\mathrm{R})$ 2-D plane by CMS in electron (a) and muon (b) final state. Constraints from boosted topology only, resolved only and combined are shown as solid blue, solid green and dashed black line [38], respectively.

1.5.2 Constraints from the other experiments

Some of the other experiments, for example, neutrino-less double beta decay and lepton-flavor violation searches, can give constraints on the target signal of this analysis. Each experiment has its own unique phase space in the two-dimensional planes of $m(W_\mathrm{R})$ and $m(N_\mathrm{R})$ masses. Furthermore, future lepton collider can be used to search for the model as well.

Meson Mixing

The LRSM can enhance the flavor changing neutral current (FCNC) processes, such as $K - \bar{K}$ and $B_{d,s} - \bar{B}_{d,s}$ oscillations, by the contribution of the W_{R} in the box diagram. The lower limit on the mass of the W_{R} from the current results [39] is about 3 TeV, assuming equal mixing matrices for left- and right-handed quarks, as shown by the pale red exclusion line in Figure 1.5. This is a strong motivation to search for sub-TeV W_{R} in this analysis.

Neutrinoless Double Beta Decay

The Majorana right-handed neutrino with the electron flavor and W_{R} boson can contribute to the neutrinoless double beta decay ($0\nu\beta\beta$) diagram. Assuming purely right-handed contribution to the $0\nu\beta\beta$ decay, the non-observation of this lepton number violating process can be used to set limits on the masses of the W_{R} and N_{R} in the LRSM. The decay amplitude of that process is:

$$G_F^2 m_{W_L}^4 \sum_{i \in \text{flavor}} \frac{|V_{ei}^2|}{m_{N_{Ri}} m_{W_R}^4},$$

where m_{W_L}, m_{W_R} and $m_{N_{Ri}}$ are masses of W_{L}, W_{R} and i-th N_{R}, and V_{ei} is the mixing of left-handed electron neutrino and i-th right-handed neutrino N_{R} [40]. This equation shows that the half-life time of the $0\nu\beta\beta$ is proportional to the multiplication of $m_{W_R}^4$ and $m_{N_{Ri}}$. the current limits on the half-life time of $0\nu\beta\beta$ corresponds to the small value of the upper boundary on the N_{R} mass ($m_{N_{Ri}} <$ const.$/m_{W_R}^4$). The excluded region by the `GERDA` experiment using ^{76}Ge target [41] is shown by the violet exclusion line in Figure 1.5. The region of $m_{W_R} > 3$ TeV and N_{R} mass around 100 GeV is not covered until the future ton-scale $0\nu\beta\beta$ experiments reach 10^{27} yr sensitivity. This region is one of the the main targets of this thesis.

Table 1.1: Isotopes of interest and observed limits of half-life time for various neutrinoless double beta decay experiments.

Collaboration	Isotope of interest	Limit at 90% C.L. [years]
`CUPID` [42]	^{82}Se	4.6×10^{24}
`CUORE` [43]	^{130}Te	3.2×10^{25}
`GERDA` [41]	^{76}Ge	1.8×10^{26}
`KamLAND-Zen` [44]	^{136}Xe	1.07×10^{26}
`EXO-200` [45]	^{136}Xe	3.5×10^{25}

Expected sensitivity of the ILC

Future lepton colliders, e.g. International Linear Collider (ILC), can also search for W_{R} and N_{R} in the LRSM. In the large $\Delta M = m(W_{\mathrm{R}}) - m(N_{\mathrm{R}})$ region, the dominant right-handed neutrino production process is the following decay mode:

$$e^+e^- \longrightarrow N_{\mathrm{R}}N_{\mathrm{R}} \longrightarrow e^{\pm}e^{\mp} + 4j.$$

The cross section of the above decay process strongly depends on the initial beam polarization. The expected sensitivities in two polarization scenarios; one is no polarization (0,0) and the other is (80%, −30%) polarization for electron and positron, are shown in Figure 1.5. The W_{R} masses up to 6.5 TeV with a 500 fb^{-1} integrated luminosity at $\sqrt{s} = 500$ GeV can be excluded at the N_{R} mass around 100 GeV [46] as shown the black exclusion line in Figure 1.5. The exclusion reach with the 250 GeV option is expected to be lower.

This analysis can cover the region which will be covered by future ton-scale $0\nu\beta\beta$ experiments and ILC, by using the LHC Run 2 data.

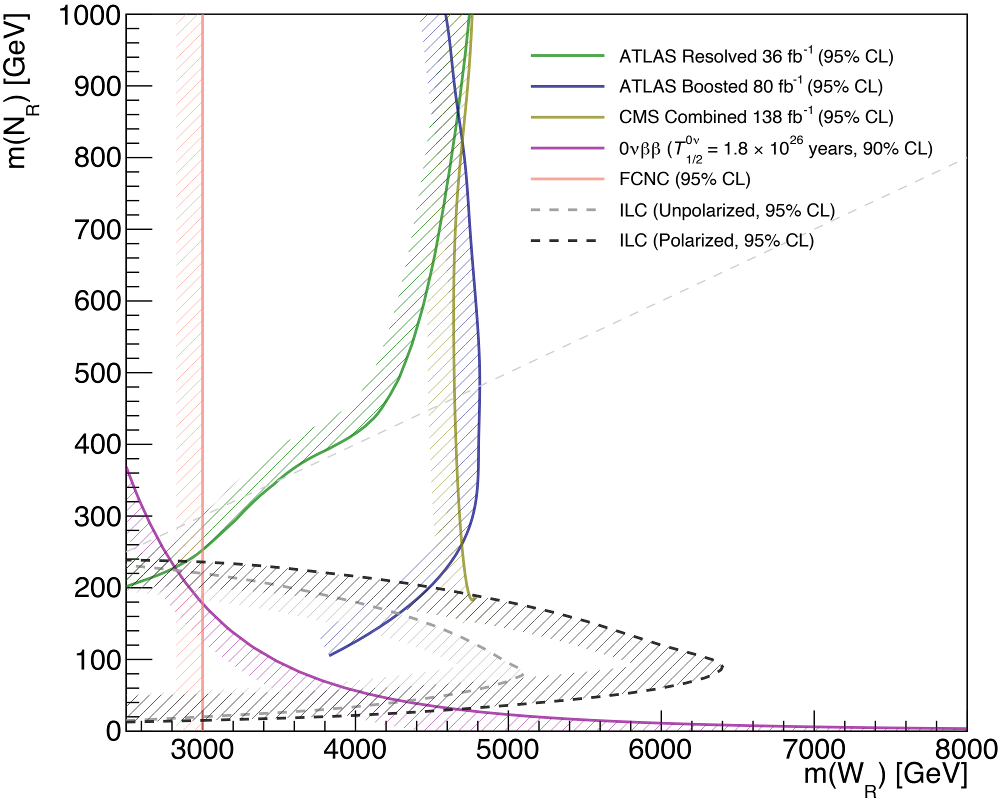

Figure 1.5: Expected and observed 95% CLs in W_R mass and N_R mass plane. Black and gray exclusion lines represent the CL from ILC with and without the initial beam polarization at $\sqrt{s}$ = 500 GeV [46], respectively. 90% CLs from the neutrino less double beta decay [41] and 95% CLs from the meson mixing [39] are shown as purple and pale red exclusion lines, respectively. 95% CLs with ATLAS resolved analysis with 36 fb^{-1} [33], ATLAS boosted analysis with 80 fb^{-1} [34] and CMS analysis with 138 fb^{-1} [38] introduced in Section 1.5.1 are shown as green, blue and dark yellow exclusion lines, respectively.

1.6 Strategy of LRSM search in boosted topology

In this thesis, different approaches are used to increase sensitivity in the electron and muon final states. For the electron channel, a new signal region that requires only one electron in an event is introduced to explore $W_R \gg N_R$ phase spaces. This is an orthogonal region with the one that was used in the previous analysis [34] by the required electrons numbers. The final sensitivities are derived by a statistically combination of these two regions. For the muon channel, the sensitivities are improved by re-optimizing the signal region that requires two muons. Schematic views of above regions are shown in Figure 1.6. In addition to the above updates, every signal regions are changed to use the reconstructed W_R mass shape more while taking into account the robustness of the background estimation.

This thesis is organized as follows. Chapter 2 explains an overview of the LHC experiment and ATLAS detectors. Chapter 3 provides an overview of the dataset and Monte Carlo simulation samples. Chapter 4 describes details of reconstructed objects with the ATLAS detector. Chapter 5 shows details of analysis

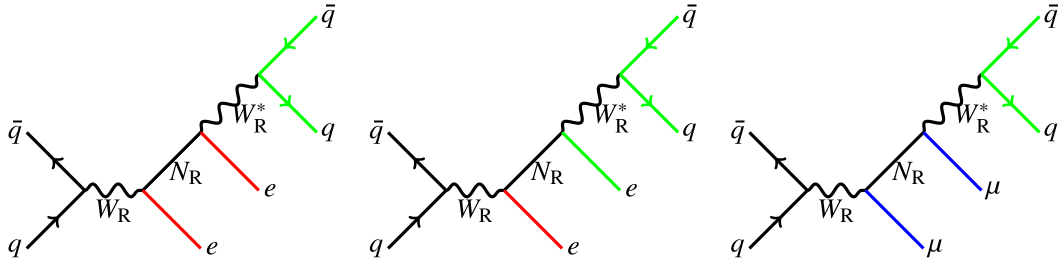

(a) Two electron channel (b) One electron channel (c) Two muon channel

Figure 1.6: Definition of three different channels. Regions are classified by the flavor and the number of leptons required in an event. The colored particles are the final state particles; red is reconstructed as electrons, blue as muons, green as jets.

strategies to maximize sensitivity. Chapter 7 describes the background of statistical treatments of the detector and theoretical effects. Chapter 9 provides the results for searching right-handed particles followed by Chapter 10 discussing interpretations of the results and giving the conclusion of this thesis.

2 LHC-ATLAS experiment

2.1 Large Hadron Collider (LHC)

The Large Hadron Collider (LHC) [47] shown in Figure 2.1 is the world's most powerful facility for particle physics research hosted by the European Organization for Nuclear Research (CERN). It is a superconducting collider located about 100 m underground in Geneva, Switzerland, that is capable of accelerating proton beams to a center-of-mass energy of $\sqrt{s}$ = 13 TeV[1].

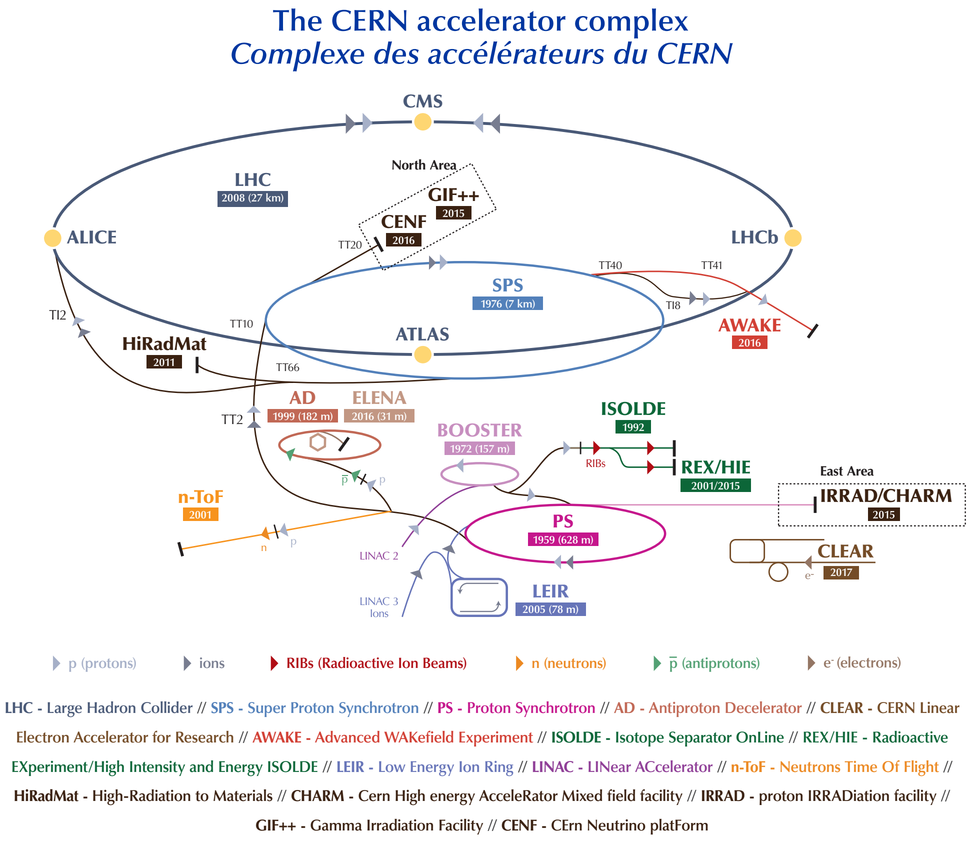

Figure 2.1: The schematic view of the CERN accelerator complex [48]. The LHC is the dark blue line in a complex chain of particle accelerators. The smaller machines are used in a chain to help boost the particles to their final energies and provide beams to a whole set of smaller experiments.

---

[1] It was designed to achieve to a center-of-mass energy of 14 TeV.

Protons are produced by a duoplasmatron source at 100 keV and accelerated by a linear accelerator (LINAC2) to 50 MeV. This is followed by a circular boosted (BOOSTER) where the protons attain energies of 1.4 GeV. Finally, the Proton Synchrotron (PS) and the Super Proton Synchrotron (SPS) accelerate the protons to 26 GeV and 450 GeV, respectively. After that protons are injected to the LHC and accelerated by following circular trajectories due to the magnetic fields produced from superconducting dipole magnets. These magnets are cooled to temperatures below 2 K using superfluid Helium.

ATLAS (A Toroidal LHC Apparatus) [49], CMS (Compact Muon Solenoid) [50], ALICE (A Large Ion Collider Experiment) [51] and LHCb (Large Hadron Collider beauty) [52] detectors are installed at the LHC. ATLAS and CMS are used for a comprehensive search for new physics and precise measurements of the SM processes. ALICE is used for the investigation of the phenomenon known as quark-gluon plasma that occurs in the early universe. LHCb aims for studies of phenomena relating to bottom quarks like CP symmetry violation.

The instantaneous luminosity is defined as:

$$L = \frac{f_{\text{rev}} n_b N_b^2}{4\pi\epsilon\beta_{x,y}} F,$$

where f_{rev} is the number of times a proton rotates through the LHC ring per second, n_b is the number of bunches carrying a proton bundle, N_b is the number of protons per bundle, ϵ is the initial geometric emittance, $\eta_{x,y}$ is the beam size in x-y plane and F is the geometric luminosity reduction factor. The typical values of these parameters for each year are shown in Table 2.1.

Table 2.1: Selected LHC parameters of pp collisions at $\sqrt{s} = 13$ TeV in 2015-2018 [53]. The values are representative of the best accelerator performance during normal physics operation. In 2017 run, two different conditions were applied. “8b4e“ denotes a pattern of eight bunches separated by 25 ns followed by a four bunch-slot gap.

Parameter	2015	2016	2017	2018
Frequency (f_{rev} [Hz])	11253	11253	11253	11253
Bunch spacing [ns]	25	25	25/8b4e	25
Maximum number of colliding bunch pairs (n_b)	2232	2208	2544/1909	2554
Typical proton bunch population ($N_b/10^{11}$ protons)	1.1	1.1	1.1/1.2	1.1
Emittance (η [m])	0.3	0.3	0.3	0.3
Beam size in x-y plane ($\beta_{x,y}$ [μm])	0.8	0.4	0.3	0.3-0.25
Geometric luminosity reduction factor (F)	0.94	0.94	0.94	0.94

2.2 ATLAS detector

The ATLAS detector, shown in Figure 2.2, is a 44 m long and 25 m height and 7000 t weight multi purpose detector. The total number of readout channel from the detector is about 160 million, and the cable length is approximately 3000 km. It consists of sub detectors with different particle detector techniques and has a complex magnet system.

The ATLAS adopts a right-handed coordinate system, defining the z-axis as the direction of the beam axis, the x-axis as the axis from the center of the detector to the center of the LHC ring, and the y-axis as the axis perpendicular to them. At the same time, the pesudorapidity η, which indicates the position with respect to

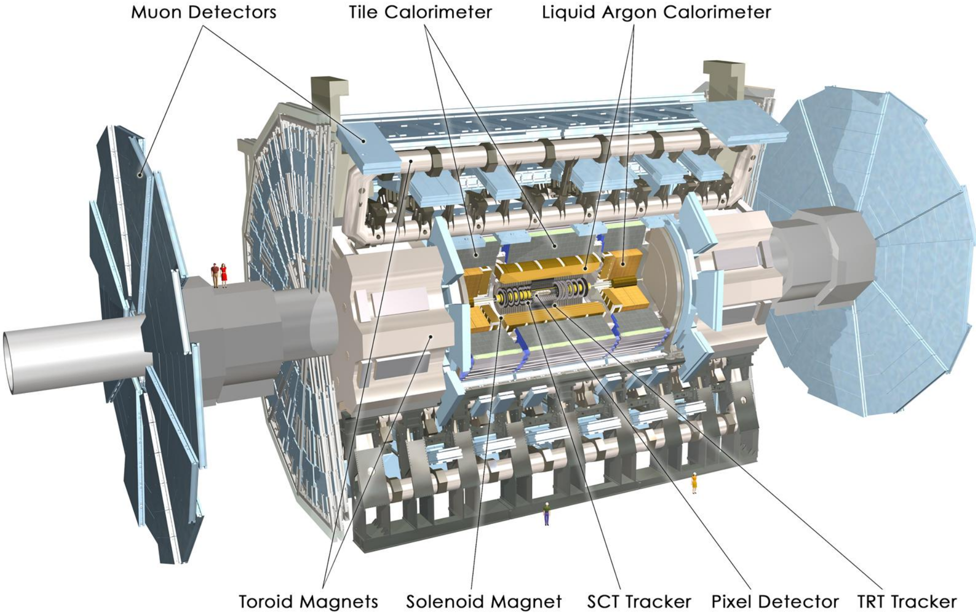

Figure 2.2: The schematic view of the ATLAS detector [49].

the beam axis, and the azimuth angle ϕ, indicates the rotation with respect to the beam axis, are used to denote the locations of particles.

The rapidity y is a variable related to the Lorentz transformation of the particle with respect to the beam axis direction, and is defined as follow:

$$y = \frac{1}{2}\ln\left(\frac{E+P_z}{E-P_z}\right) = \ln\left(\frac{E+P_z}{\sqrt{p_T^2+m^2}}\right) \tag{2.1}$$

where E, p_z, p_T, m represent energy, momentum respect to the beam axis, momentum in the direction orthogonal to the beam axis and the invariant mass, respectively. In considering a Lorentz transformation of the particle with respect to the beam axis, the rapidity, shown in equation 2.1, varies by using variables $\beta = v/c = \tanh\Delta$ and γ which correspond to the difference between the reference system and the transformed systems as follows:

$$\begin{aligned} y \rightarrow y' &= \frac{1}{2}\ln\left(\frac{E'+P'_z}{E'-P'_z}\right) = \frac{1}{2}\ln\left(\frac{\gamma E+\beta\gamma P_z+\gamma Pz+\beta\gamma E}{\gamma E+\beta\gamma P_z-\gamma Pz-\beta\gamma E}\right) \\ &= y+\frac{1}{2}\ln\left(\frac{1+\beta}{1-\beta}\right) = y+\Delta \end{aligned} \tag{2.2}$$

As shown in equation 2.2, the rapidity between different particles does not depend on the choice of a frame. Since the maximum rapidity of a particle depends on its energy and maximum energy of a particle is half of the center of energy in the center of mass system, the maximum value of the rapidity can be calculated as follows:

$$y^{CM}_{max} = \frac{1}{2}\ln\left(\frac{\frac{\sqrt{s}}{2}+\sqrt{\frac{s^2}{4}-m^2}}{\frac{\sqrt{s}}{2}-\sqrt{\frac{s^2}{4}-m^2}}\right) = \frac{1}{2}\ln\left(\frac{\left(\frac{\sqrt{s}}{2}+\sqrt{\frac{s^2}{4}-m^2}\right)}{m^2}\right) \simeq \ln\frac{\sqrt{s}}{m}$$

The maximum value of the rapidity depends on the mass of a particle. The pesudorapidity is a massless approximation of the the rapidity and expressed using the polar angle θ from the center point of the detector as follows:

$$\eta = \frac{1}{2}\ln\left(\frac{E + E\cos\theta}{E - E\cos\theta}\right) = -\ln\left(\tan\frac{\theta}{2}\right) \tag{2.3}$$

As the definition of equation 2.3, η can take $\pm\infty$ and represents the position in the beam axis direction.

2.2.1 LUCID-2

The LUCID-2 (LUminosity Cherenkov Integrating Detector) [53] is a dedicated luminosity monitor. This was updated during the long shutdown between Run 1 and Run 2 experiment to cope with the higher luminosity. LUCID-2 consists of two modules (A and C) placed around the beam-pipe and symmetrical with respect to the interaction points, at 17 m from it. Each module consists of 16 PMTs, grouped by 4×4 groups with ^{207}Bi radioactive sources deposited on the windows for calibration purpose. In addition, there are also 4 bundles of quartz fibers read out by PMTs located 1.5 m away from the detector in a lower radiation area.

2.2.2 Magnet system

The magnet system [54] used in the ATLAS experiment is divided into three components, Central Solenoid, Barrel Toroid and Endcap Toroid, all of which are superconducting magnets, as shown in Figure 2.3. The magnetic field of the Central Solenoid is 2 T, provided for the accurate charged particle track reconstruction inside the inner tracker, and consists of a 5.3 m long and 2.4 m diameter single-phase coil. Since it is installed inside the calorimeter, a low molecular weight substance is used. Each of the Barrel Toroid and Endcap Toroid are divided into eight sub-magnets and installed along the beam axis. They are used for the purpose of bending the muon trajectories. The strength of the magnetic field is varied depending on the area of the detector.

2.2.3 Inner detector

The inner detector [55] illustrated in Figure 2.4 is located closest to the interaction point. The inner detector is 6.2 m long and 2.1 m in diameter, and is divided into a barrel region and an end cap region, covering up to $|\eta| \leq 2.5$. The barrel region is a cylinder-shaped detector, while in the end cap region, the detector structure is perpendicular to the beam axis. The 2 T magnetic field from the central solenoid bends the trajectories of the charged particles, and momenta can be measured from their curvature. The inner detector consists of Pixel Detector (Pixel), Semi-Conductor Tracker (SCT), and Transition Radiation Tracker (TRT).

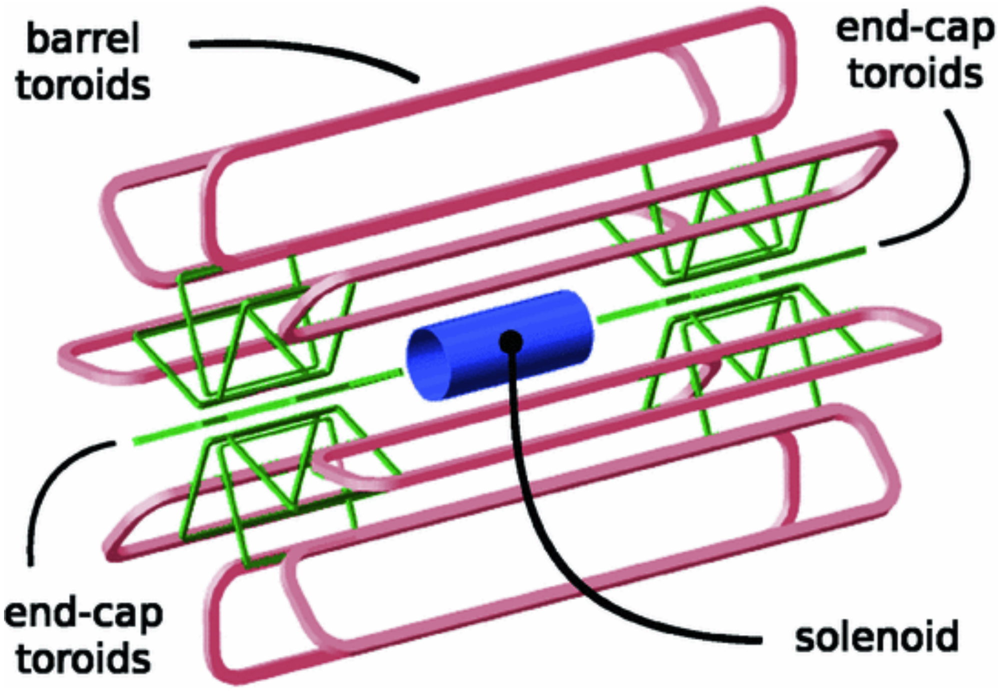

Figure 2.3: The magnet system [54] in the ATLAS experiment.

2.2.4 Calorimeter

Calorimeters illustrated in Figure 2.5 are divided into the electromagnetic calorimeter [56] used for detecting electrons and photons and the hadron calorimeter [57] used for detecting hadron activities. Whole-area electromagnetic calorimeter and end-cap and forward area hadron calorimeter use liquid argon as a detector layer due to its high radiation resistance, and different materials as an absorber (lead, copper or tungsten), depending on the area of the detector. Input particles cause a cascade shower, whereby electrons ionized from the liquid argon atoms are read out as a signal. The energy of the input particles has a very good linearity with the number of ionized electrons. Hadron calorimeter in the barrel-region is called tile calorimeter and have iron as the absorber and plastic scintillator as the detector.

All the calorimeters are sampling calorimeter, and the energy resolution is generally expressed by the following [58]:

$$\frac{\sigma(E)}{E} = \frac{a}{E} \oplus \frac{b}{\sqrt{E}} \oplus c.$$

The first term is called the noise term and represents the contributions of noise and pileup effects and is predominant at low energy region. The second term is called the sampling term, which depends on the conditions of the active and absorber layers, and it dominant in the energy range of 10 to 100 GeV. The third term is called the constant term and has the largest contribution in the high energy region. Typical values of them are listed in Table 2.2.

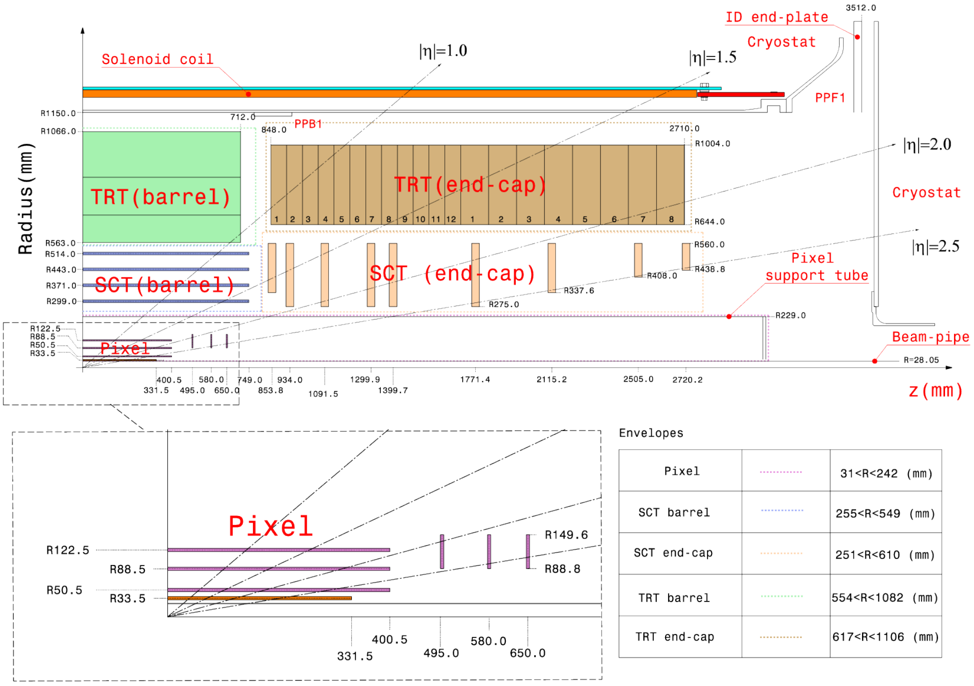

Figure 2.4: The inner detector [55] in the ATLAS detector.

Table 2.2: The typical value of noise term, sampling term and constant term for the electromagnetic calorimeter. Electron energy measurements with a module of the EM barrel LAr calorimeter had been studies in the range from 10 to 245 GeV impinging at $\eta = 0.687$ during test beam [58].

Parameter	Typical value
Noise term a	$0.25\ \% \cdot \text{GeV}$
Sampling term b	$10.1 \pm 0.1\ \% \cdot \sqrt{\text{GeV}}$
Constant term c	$0.17 \pm 0.04\ \% \cdot \text{GeV}$

2.2.4.1 Electromagnetic calorimeter

The electromagnetic calorimeter covers $|\eta| < 4.9$ and is a three-layer detector. It is a very finely divided detector in the η direction, fine enough to identify the two photons from π^0 decay. It has as characteristic accordion structure, which can eliminate the insensitive region in the ϕ direction.

2.2.4.2 Hadron calorimeter

The hadron calorimeter is installed outside the electromagnetic calorimeter because hadrons only drop part of their energy into the electromagnetic calorimeter. The hadron calorimeter relies on the strong interaction to measure the energy of the hadrons and stops them not to reach to the muon spectrometer.

The gap between hadronic calorimeter barrel and extended barrel and electromagnetic calorimeter barrel and end-cap sections which has $1.37 < |\eta| < 1.52$ is known as “crack-region“. Special cells made by

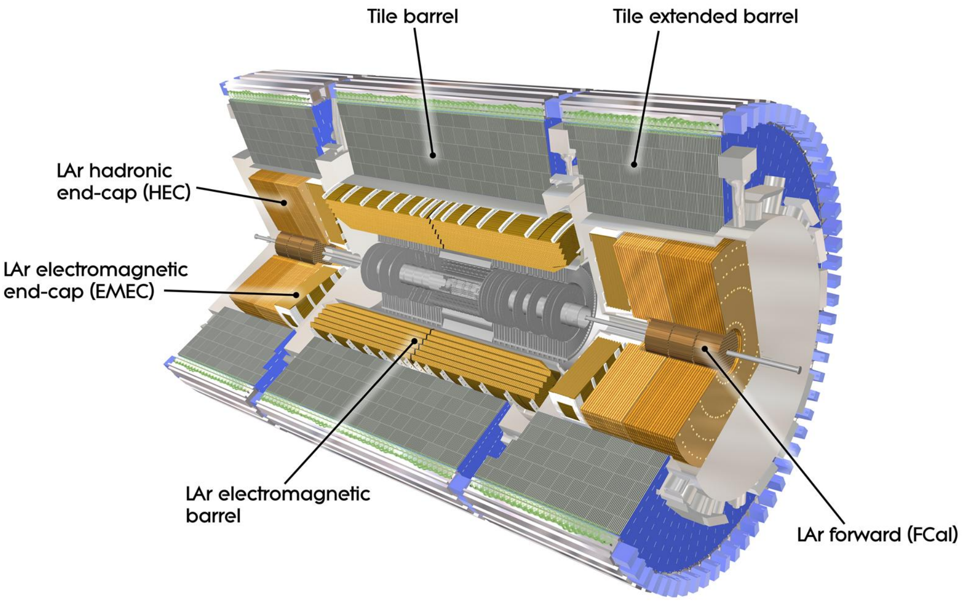

Figure 2.5: The calorimeters [57] in the ATLAS detector.

scintillators are installed.

2.2.5 Muon spectrometer

The muon spectrometer [59] shown in Figure 2.6 is located at the outermost layer of the detector because muon, which has a small cross-section of bremsstrahlung thanks to its large mass compared to the electron, are not absorbed by the calorimeter except for neutrinos. For the accurate momentum measurement, the magnetic field from the toroid magnet is used to bend the muon orbit with respect ti the r-z plane. The muon spectrometer consists of Monitored Drift Tubes (MDT), Thin-Gap Chambers (TGC), Resistive-Plate Chambers (RPC) and Cathode Strip Chambers (CSC). TGC and RPC are used for trigger issuances.

2.3 Trigger and data acquisition system

One of the biggest challenges in the ATLAS detector is to select and acquire events of interest from the large amount of proton collision data. The ATLAS detector is exposed to proton collision data at 25 ns intervals during Run 2, reducing the event acquisition rate from 40 MHz of nominal bunch crossing to 1 kHz. ATLAS has a two-stage triggering system, with first-stage triggering performed by a hardware-based Level One (L1) trigger, followed by a software-based High-Level Trigger (HLT). For events passing the conditions of L1 trigger, all detector information is stored in the Readout Driver (ROD) and sent to the Data Acquisition (DAQ) system. Subsequently, events fulfilling the conditions of HLT are stores in a large storage for physics analysis.

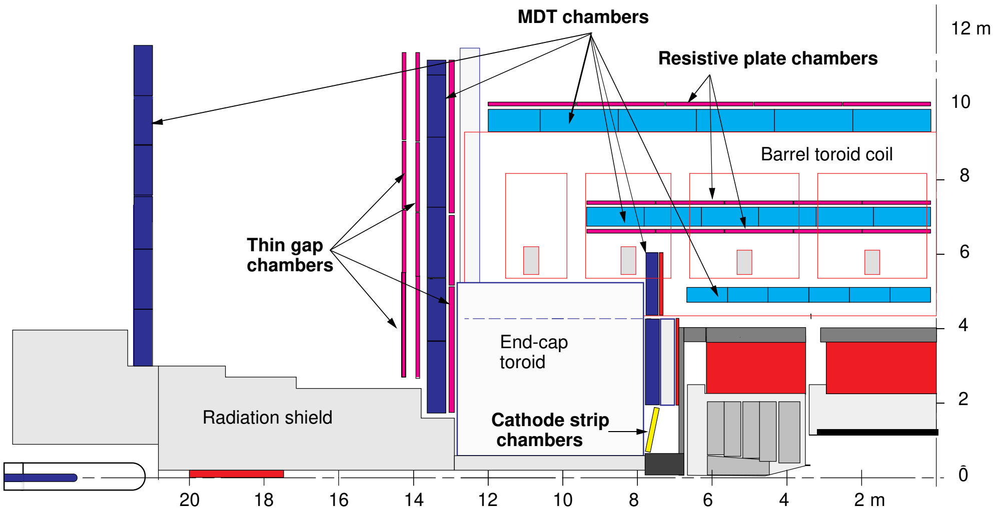

Figure 2.6: The schematic of r-z cross section view of the muon spectrometer [59].

2.3.0.1 L1 trigger

The L1 trigger [60] roughly surveys high momentum muons, electrons, photons, jets and tau particles and $E_{\mathrm{T}}^{\mathrm{miss}}$ described in section 4.10 within 2.5 μs using limited detector information. This can reduce the collection frequency from 40 MHz to 100 kHz. L1 trigger further defines the ‘Region of interest (RoI)‘, which is information about the rough energy distribution, and sends them to the High level trigger.

2.3.0.2 HLT

The high level trigger [61–64] performs a more detailed investigation of the detector information and trigger recipes that depend on the particle of interest, with an event storing time of about 550 ms. Finally, the collection frequency is reduced to about 1 kHz.

3 Dataset and Monte-Calro samples

3.1 Dataset

The data used in this analysis were collected during 2015, 2016, 2017 and 2018 at $\sqrt{s} = 13$ TeV. The combined 2015-2018 integrated luminosity is 139 fb^{-1} with the uncertainty of 1.7 % [65], obtained using the LUCID-2 detector for the primary luminosity measurements. Table 3.1 shows the integrated luminosity for each year.

Table 3.1: Summary of integrated luminosity for each year.

Year	Integrated luminosity in fb^{-1}
2015	3.22
2016	33.0
2017	44.3
2018	58.5
Total	139

Another important parameter related to the instantaneous luminosity is the average number of inelastic interactions per bunch crossing, known as the pile-up. The average number of pile-up per bunch crossing in the dataset is 33.7. The pile-up degrades the performance of the reconstructed physics objects and makes the identification of vertices and the reconstruction of tracks more difficult. The detector response can be longer than the duration time of 25 ns between two different bunches and be affected by not only the present bunch (in-time pile-up) but also pile-up from previous and following bunches (out-time pile-up). The cumulative luminosity, delivered by the LHC, recorded by ATLAS, saved for physics analysis, and the luminosity as a function of pile-up are shown in Figure 3.1.

3.2 Trigger

Since the signal event in this analysis has an isolated lepton with a large momentum in clean environment, such a lepton is used as the trigger condition. Several unprescaled[1] HLT (single lepton trigger) following the L1, as listed in Table 3.2, are used to maximize the data statistics.

"L1EM20" means that the L1 trigger imposes an transverse energy threshold of 20 GeV or higher on EM objects reconstructed in the electromagnetic calorimeter. “V” and “H” indicate that the E_{T} correction is made for the η direction and the hadron calorimeter information is not used in the construction of the EM

---

[1] For example, if the momentum of the lepton required by the trigger is low and the trigger rate is high, more trigger accepts may be issued than allowed. In such a case, the event rate to be obtained may be intentionally reduced, which is called prescale.

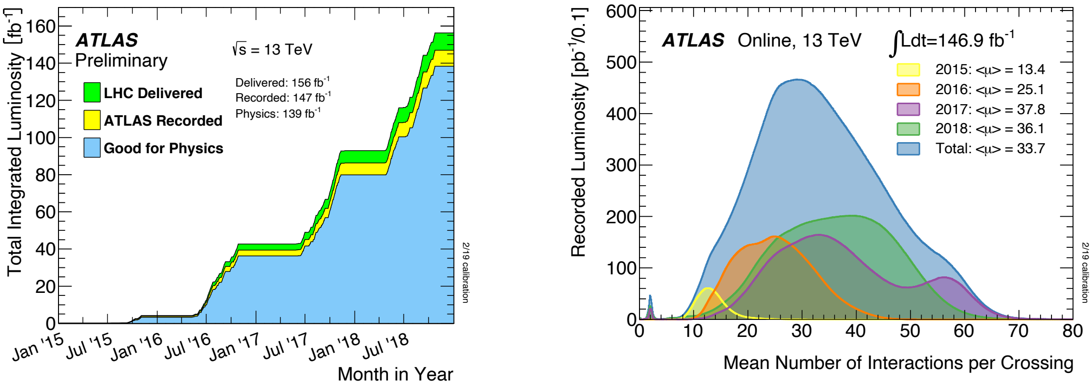

(a) Integrated luminosity

(b) Interactions per bunch

Figure 3.1: (a) The integrated luminosity delivered to LHC (green) and ATLAS (yellow) in Run 2 period [66]. The blue histogram shows the one recorded for physics analysis after requiring the data quality. (b) The luminosity recorded by ATLAS as a function of mean number of proton interactions per bunch crossing in Run 2 period [66].

objects, respectively. On the other hand, "L1MU15" means that muon p_T above 15 GeV is required in the L1 trigger.

The numbers following "HLT_e" or "HLT_mu" indicate the E_T or p_T threshold in HLT. The "lhmedium" and "lhloose" denote the requirement of an electron identification using the likelihood discriminant of the multivariate techniques. The "nod0" means no information on the impact parameter is used. "ivarmedium" and "iloose" represent the additional requirements of an isolation.

Table 3.2: A summary of trigger requirements. A logical OR is performed for a given year.

Channel	2015	2016, 2017 and 2018
Electron	HLT_e24_lhmedium_L1EM20VH HLT_e60_lhmedium HLT_e120_lhloose	HLT_e26_lhtight_nod0_ivarloose HLT_e60_lhmedium_nod0 HLT_e140_lhloose_nod0
Muon	HLT_mu20_iloose_L1MU15 HLT_mu50	HLT_mu26_ivarmedium HLT_mu50

3.3 Monte-Calro samples

Monte Carlo (MC) simulated samples are used to model both the background and signal processes. The full set of simulated samples is summarized in Table 3.3. The generated events are processed through a simulation of the ATLAS detector geometry and response using GEANT4 [67], and through the same reconstruction software as the one used in the collected data.

The effect of pile-up is also included in the simulation [68]: simulated events are re-weighted to reproduce the actual pile-up distribution as shown in Figure 3.1(b). The simulated event is then multiplied by (1/0.99) and (1/1.07) to realize the mean of observed pile-up and vertex, respectively. The middle value of them

(1/1.03) is used as nominal and (1/0.99) and (1/1.07) are applied as up and down type pile-up re-weighting scale factor. respectively.

3.3.1 General description of inclusive cross-section

An inclusive cross section σ for $pp \longrightarrow X$ calculated at n-th order in perturbation theory is factorized into a "hard part" $\hat{\sigma}_{ij}$ and "normalization parts" $f_{i,j}$ as follows:

$$\sigma = \sum_{i,j} \int dx_1 f_i(x_1, \mu_F^2) \int dx_2 f_j(x_2, \mu_F^2)\ \hat{\sigma}_{ij}(x_1, x_2, \mu_R^2),$$

where x_1 and x_2 represent longitudinal momentum fractions of struck partons in two different protons and $f_{i,j}$ are known as parton density functions (PDF) which are probability density functions for finding a parton with a certain scale x.

PDF is obtained by fitting many data from various experiments with a certain function.

μ_F and μ_R are known as a factorization scale and a renormalisation scale, respectively. μ_F is introduced to cure the ultraviolet divergences which appear because of large momentum in the loops of the Feynman diagrams. On the other hand, μ_R is introduced to cure the infrared divergences which appear because either a virtual or a real particle can reach a zero momentum, or a massless particle radiates another massless particles.

The "hard part" $\hat{\sigma}$ is expanded with the series of a strong coupling constant α_s as follows:

$$\hat{\sigma}^n = \alpha_s \hat{\sigma}^1 + \alpha_s^2 \hat{\sigma}^2 + \cdots + \alpha_s^n \hat{\sigma}^n + O(\alpha_s^{n+1})$$

In this analysis, MC samples with up to next-to-next leading order (NNLO) corresponding to second order expansion are used. The strong coupling constant α_s is also determined experimentally. The renormalisation group equation is then used in the MC generator to predict the value of α_s at different energy scales that appear in the generated process.

The PDFs are obtained by fitting many data from various experiments with a certain function for the parton content of the proton at a given scale. The Dokshitzer-Gribov-Lipatov-Altarelli-Parisi evolution equations [69–71] are then used to estimate the PDFs at different scales.

The cross section above is at parton level. Most MC samples are then converted to a cross section at hadron level by interfacing to showering and hadronization generators. In that process, (I) events with N partons and (II) events with N-1 partons plus one hard radiation from the shower indicate the same physical phenomenon, and only one of them needs to be selected. This is called parton-jet matching, which uses a certain cutoff scale to determine whether to retrieve (I) or (II).

3.3.2 Simulated signal samples

The signal events described by the LRSM is implemented in the MADGRAPH_AMC@NLO [72] generator at leading-order (LO) using FeynRules [73]. For the simulated signal produced MADGRAPHAMC@NLO is interfaced to PYTHIA8.230 [74] for parton showering. The A14 parameter set [75] is used for tuning the shower. The NNPDF3.1NLO [76] parton distribution function set enters in the matrix element calculation and the NNPDF2.3LO [77] is used in the parton shower.

The simulation includes a Majorana N_R with a 50 % mixture of same-sign and opposite-sign lepton pairs. This enables studies in both the opposite-signal and same-sign channels. The generated signal mass points and their cross section are shown in Figure 3.2. In the case of a Dirac N_R, only opposite-sign leptons can produced so that the measured cross-section can be double that simulated samples. The signal samples do not include lepton flavour-mixing, although this is a free parameter of the model and could be studied in the future.

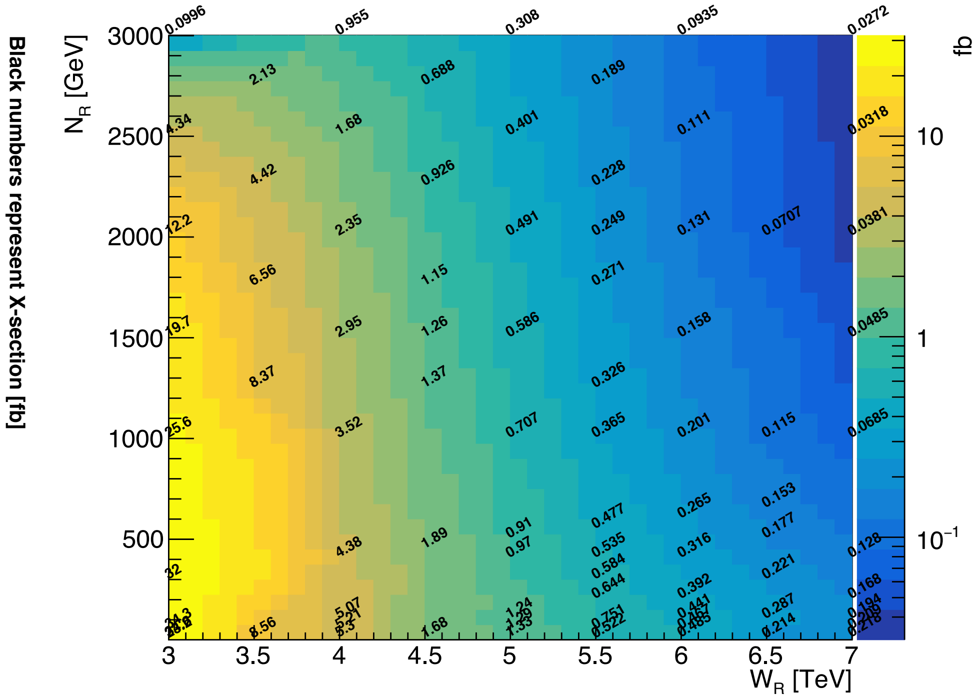

Figure 3.2: Generated MC signal points in the 2D plane of W_R mass and N_R mass. Black numbers represent the cross-section.

3.3.3 Simulated background samples

The production of W/Z boson in association with jets is simulated with the NNPDF3.0NNLO PDF set and the ATLAS configuration of SHERPA 2.2.11 [78], which includes matrix elements for up to five partons at LO and up to two partons at NLO. They are calculated with the COMIX [79] and OPENLOOPS [80] libraries and matched with the SHERPA parton shower [81] using the MEPS@NLO prescription with a set of tuned parameters developed by the SHERPA authors.

For the background contributions originating from the QCD multijet is generated using PYTHIA 8.230 [82] with LO matrix elements for dijet production which are matched to the parton shower. The renormalisation and factorisation scales are set to the geometric mean of the squared transverse masses of the two outgoing particles in the matrix element, $\hat{p}_T = \sqrt{(p_{T,1}^2 + m_1^2)(p_{T,2}^2 + m_2^2)}$. The NNPDF2.3LO PDF set [83] is used in the matrix element generation, the parton shower, and the simulation of the multi-parton interactions. The A14 set of tuned parameters is used.

The production of γ in association with jets is simulated with the ATLAS configuration of SHERPA 2.2.2 [78] as well as W/Z boson production. Matrix elements are calculated for up to two partons at NLO and four partons at LO. The NNPDF3.0NNLO set of parton distribution functions is used in the SHERPA parton shower.

For the background contributions originating from the top-quark related processes were modelled using the POWHEG-BOX v2 [84–87] generator at NLO with the NNPDF3.0NLO PDF set. The events were interfaced with PYTHIA 8.230 [82] for the parton shower and hadronization modelling with the A14 tune and the NNPDF3.0NLO set of PDFs. Top quark decay is modeled using MADSPIN [84, 88] to preserve spin correlations. The decays of bottom and charm hadrons are performed by EVTGEN 1.6.0 [89] program in all top-quark processes.

The diboson (WW, WZ, ZZ) processes decaying into four leptons and at least one quark are simulated with the ATLAS configuration of SHERPA 2.2.2 and SHERPA 2.2.1 [78] generator with NNPDF3.0NNLO set [76], which includes matrix elements for no or one parton at NLO and up to three partons at LO.

The MC samples generated at NLO prediction are normalized to the cross section at NNLO prediction.

Table 3.3: Simulated signal and background samples. The corresponding event generator, parton shower, cross-section normalization, PDF set used for the matrix element and set of tuned parameters are shown for each sample. The generator cross-section of the generator used to generate the sample is used where not specifically stated otherwise.

Physics process	Generator	PDF set	Cross-section normalization	Parton shower	Tune
Signal	MADGRAPH_AMC@NLO	NNPDF3.1NLO	LO	PYTHIA 8.230	A14
$W(\to \ell\nu)$ + jets	SHERPA 2.2.11	NNPDF3.0NNLO	NNLO	SHERPA	SHERPA
$Z(\to \ell\bar{\ell})$ + jets	SHERPA 2.2.11	NNPDF3.0NNLO	NNLO	SHERPA	SHERPA
γ+jets	SHERPA 2.2.2	NNPDF3.0NNLO	NNLO	SHERPA	SHERPA
QCD multi-jet	PYTHIA 8.230	NNPDF2.3LO	LO	PYTHIA 8.230	A14
$t\bar{t}$	POWHEG-BOX v2	NNPDF3.0NNLO	NNLO	PYTHIA 8.230	A14
single-top	POWHEG-BOX v2	NNPDF3.0NNLO	NNLO	PYTHIA 8.230	A14
di-boson	SHERPA 2.2.1	NNPDF3.0NNLO	NNLO	SHERPA	SHERPA

4 Object reconstruction and identification

In this section, details of the object selection are described. The physics objects to reconstruct the final discriminant ($m(W_\mathrm{R})$) are electrons, muons and large-R jets. Small-R jets and missing transverse energy is also used to select the signal candidate events.

4.1 Charged track

When a charged particle passes through the inner detector, it leaves signals at each layer of them. By combining them in the following three steps [90], the trajectory of a charged particle is reconstructed as a "track".

1. Charged particle reconstruction begins by clustering the signals in each later of the inner detector. The three-dimensional clusters are called "space-points".
2. Seed-tracks are created based on these space-points. Then, preliminary tracks are formed by using a combinatorial Kalman filter [91]. There are still different tracks having the same space-points and are needed to solve these ambiguities.
3. A "track score" is introduced to assign a quality to each track. Track score depends on the position of space-points, expected trajectory which is not observed and the χ^2 of the track fit. Tracks with bad quality are eventually discarded, and the remaining tracks are required to pass minimum conditions shown in Table 4.1. d_0^BL and z_0^BL are the transverse and longitudinal impact parameter with respect to the beam line.

Table 4.1: Charged track criteria.

Feature	Value
p_T	500 MeV
$\lvert\eta\rvert$	< 2.5
$\lvert d_0^\mathrm{BL}\rvert$	< 2.0 mm
$\lvert z_0^\mathrm{BL}\sin\theta\rvert$	< 3.0 mm

4.2 Primary vertex

The points where at least two tracks intersect are called vertexes, and multiple vertexes are generated due to the pile-up at a single bunch crossing. A primary vertex is defined as the most energetic vertex, which is defined as the largest $\sum p_\mathrm{T}^2$, where p_T is the transverse momentum of the associated tracks.

4.3 Topological Cluster

The energy deposited by particles in each cell of the calorimeter is combined to form a topological cluster (topo-cluster) [92]. The three-dimensional information of the calorimeter cells is used to reconstruct the topo-cluster, and the sum of the energies of the grouped cells is assigned as the energy that the topo-cluster has. At the same time, the direction of the incident particles is also observed. The condition to include a calorimeter cell as a component of a topo-cluster is given below:

$$\varsigma_{\mathrm{cell}}^{\mathrm{EM}} = \frac{E_{\mathrm{cell}}^{\mathrm{EM}}}{\sigma_{\mathrm{noise,cell}}^{\mathrm{EM}}}$$

where $\varsigma_{\mathrm{cell}}^{\mathrm{EM}}$ is a cell signal significance which represents a significance of energy deposit relative to the noise $\sigma_{\mathrm{cell}^{\mathrm{EM}}}$ and $E_{\mathrm{cell}}^{\mathrm{EM}}$ is the energy measured in the calorimeter cell. Both quantities are measured by the EM energy scale. The energy deposit by electron and photons is correctly handled with the EM energy scale, and any corrections for hadrons are not taken into account.

The following steps are used to reconstruct topo-clusters.

1. A proto-cluster, a candidate of topo-cluster, reconstruction starts from a seed cell having $\varsigma_{cell}^{EM} > 4$.
2. If a neighboring cell fulfil $|\varsigma_{cell}^{EM}| > 2$, the cell is merged into the proto-cluster. As long as the conditions are met, the step 2 is repeated.
3. If a neighboring cell fulfil $2 \geq |\varsigma_{cell}^{EM}| > 0$, the cell is merged into the proto-cluster and the loop is broken.

In case two different proto-clusters are adjacent to each other, and they are close to each other separated by a cell satisfying $|\varsigma_{cell}^{EM}| > 2$, they are merged.

4.4 Jet

Quarks and gluons are observed in the detector as a set of particles, which looks like a spray, due to the hadronization process. Hadrons interact with the detector materials and leave a signal with a wider radius than that of the EM object. Jet energy measurements can be improved by making complete use of the information from both the tracking and topo-cluster, which is known as a particle-flow object [93] behaving as a single particle. The energy deposit of particle-flow object is formed by replacing the topo-cluster's energy with the momenta of tracks that are matched to the topo-cluster. Jet reconstruction is performed by combining the particle-flow objects with the anti-k_t algorithm [93]. The anti-k_t algorithm uses the distance d_{ij} between different particle-flow objects as an indicator below:

$$d_{ij} = min\left(\frac{1}{p_{\mathrm{T},i}^2}, \frac{1}{p_{\mathrm{T},j}^2}\right)\frac{\Delta R_{ij}^2}{R^2},$$

where $p_{\mathrm{T},i}$ and $p_{\mathrm{T},j}$ are the p_{T} of the i-th and j-th particle-flow objects and ΔR_{ij} is the angular distance between them given by the following:

$$\Delta R_{ij} = \sqrt{(\eta_i - \eta_j)^2 + (\phi_i - \phi_j)^2}.$$

R is a parameter and corresponds to the cone size. $R = 0.4$ is used to form small-R jet.

The algorithm calculates the smallest d_{ij} and $d_{iB} = 1/p_{\mathrm{T},i}^2$. If the d_{ij} is smaller than d_{iB}, two particle-flow objects, labeled i-th and j-th, are merged into a new object which is re-labeled as i-th. This procedure is repeated until the d_{iB} becomes the smallest. This i-th object is recognized as a jet and the all used particle-flow objects in the jet are removed from the list of particle-flow objects, and then the anti-k_t algorithm is applied to the remaining particle-flow objects.

Energy of topo-clusters are scaled at EM scale, so jets handling hadron objects need to be calibrated with following methods. This is done with several steps by comparing MC and data [94].

Origin correction

The origin correction corrects the direction of jet to point to the hard-scattering vertex from the center of the detector while keeping the jet energy constant. This correction improves the η resolution.

Pile-up correction

Pile-up produces soft backgrounds and can obscure the energy of the jets. In-time and out-time pile-up are canceled out with area-based and residual pile-up correction as follows:

$$p_{\mathrm{T}}^{\mathrm{corr}} = p_{\mathrm{T}}^{\mathrm{reco}} - \rho \times A - \alpha(\eta) \times (N_{\mathrm{vertex}} - 1) - \beta(\eta) \times \mu,$$

where $p_{\mathrm{T}}^{\mathrm{reco}}$ and $p_{\mathrm{T}}^{\mathrm{corr}}$ represent jet p_{T} at the EM scale and corrected scale, respectively. The second term corresponds to the area-based pile-up correction. ρ is an average p_{T} density measured in the events. The third and fourth terms correspond to the residual correction based on the number of reconstructed vertex N_{vertex} and the mean number of inelastic interactions per bunch crossing μ. α and β are coefficients which are functions of η.

Absolute MC-based calibration

To calibrate the energy of the reconstructed jet at the EM scale topo-clusters, MC samples are used. The comparison of the reconstructed energy with the truth jet's energy, where the truth jet is formed by performing anti-k_t algorithm against stable and visible truth particles, by using the MC truth information is performed. The correction is performed depending on the η and E_{T} of a target jet. The calibration factors are derived by fitting $E_T^{\mathrm{reco}}/E_T^{\mathrm{truth}}$ with a gaussian function.

Global sequential calibration

Since the number of color charges is different between quark- or gluon-origin jets, the calorimeter responses are different as well. A quark-origin jet tends to have hadrons with higher p_{T} and fewer accompanied particles than a gluon-origin jet. Not only calorimeter and tracking information but also muon spectrometer is used to correct jet energies. This correction improves the agreements between data and MC to within 2-4%.

Residual in situ calibration

As the final step, the differences between MC and data are corrected using the response $R_{\mathrm{in\ situ}}$ which is p_{T} ratio of a jet against other well-measured reference object like Z boson and photon. The ratio of the $R_{\mathrm{in\ situ}}$ between data and MC is used to correct the jet p_{T} as a function of p_{T} and η.

The above procedures correct only jet energy scale responses, but the resolution of energy response are still needed to be calibrated.

The jet energy resolution is parameterized as a function of three terms [95],

$$\frac{\sigma_{p_\mathrm{T}}}{p_\mathrm{T}} = \frac{N}{p_\mathrm{T}} \oplus \frac{S}{\sqrt{p_\mathrm{T}}} \oplus C,$$

where N indicates the effect of noise derived from electronic noise and pile-up effects, S indicates the sampling term, and C is a p_T independent constant term. The jet energy resolution is measured with observed data in 2017 corresponding to an integrated luminosity of 44 fb^{-1}. For the central pesudorapidity region, γ+jets and Z+jets events are used to measure with good precision. On the other hand, in the forward pesudorapidity region, dijet events give the most precise determination of the resolution. Typical values for jets with a radius parameter $R = 0.4$ shown in Table 4.2.

Table 4.2: Three constants for jet energy resolution measured for jets with radius parameter $R = 0.4$ [93].

$\lvert\eta\rvert$ range	N [GeV]	S [$\sqrt{\mathrm{GeV}}$]	C
(0.0, 0.8)	4.12 ± 0.74	0.74 ± 0.10	0.023 ± 0.003
(0.8, 1.2)	3.66 ± 0.75	0.64 ± 0.13	0.039 ± 0.009
(1.2, 2.1)	4.27 ± 0.75	0.58 ± 0.15	0.034 ± 0.007
(2.1, 2.8)	3.38 ± 0.65	0.26 ± 0.36	0.050 ± 0.010

The baseline criteria for reconstructed jet are summarized in Table 4.3.

Table 4.3: Small-R jet selection criteria.

Feature	Value
Radius parameter R	0.4
p_T	> 20 GeV
$\lvert\eta\rvert$	< 4.0
Mass	> 0 GeV

4.5 B-tagging

Jets derived from b-quarks, b-jets, have some characteristics such as a longer life time than other quarks and a secondary vertex that is displaced from the primary vertex. Based on these features, a b-tagging algorithm, to determine whether each jet is b-quark induced or not, is applied. In this analysis, DL1r [96] b-tagging algorithm is used.

DL1r performs identification using a deep learning neural network, and the input includes discriminant variables constructed by a recurrent neural network, which can take advantages of spatial and kinematic correlations between different tracks generated from the same b-quark. This approach has been found to improve performance primarily for jet with high p_T [97].

The working points are defined by a single cut value on the discriminant output distribution. 77% working point, which is expected to provide the best signal sensitivity, is employed in this analysis. In a sample of simulated SM $t\bar{t}$ events, the rejection factors of 600 and 11 are achieved for light-flavour and charm jets, respectively. The performance of the b-tag strongly depends on the p_T of a jet; the efficiency decreases from 65% when the b-jet p_{T} is about 500 GeV to 10% when the p_{T} is about 2 TeV. To compensate for the mis-modelling of the MC with respect to the data, a scale factor is adapted according to the jet p_{T}.

4.6 Electron

Electrons sometimes emit photons by bremsstrahlung, which in turn produce a electron-positron pair. By repeating these processes, a cascade shower is formed in the calorimeter. In addition, since the electrons are charged particles, they leave trajectories in the inner detector. Electrons are reconstructed with these two information.

There are several basic definitions of electrons in different working points and they are generally common to all ATLAS analysis. These basic definitions are based on three categories: electron reconstruction, identification and isolation. Most analyses then choose one of the basic working points and complement it with additional specific analysis cuts.

The electron reconstruction efficiency measured with 2015 and 2016 data is greater than 98% in almost all the phase space [98]. In order to account for differences in simulation and data, scale factors are applied to reconstructed electrons in MC. The scale factors are expressed in bins of electron p_{T} and η. They differ from unity up to 0.5% in all of the bins at most. In addition, transverse (d_0) and longitudinal (z_0) track parameters with respect to a primary vertex are used to ensure that an electron originates from a primary vertex.

There is no guarantee that objects reconstructed as electrons, are truly electrons. The main sources of fake electrons are jets and electron from photon conversions. In this analysis, two general working points are used to discriminate between prompt and fake electrons by using a multivariate likelihood fit of the tracking and calorimeter information. The identification working points used are `Medium` for baseline electron and `Tight` for signal like events. The efficiencies for identifying a prompt electron with $E_{\mathrm{T}} = 40$ GeV are 93% and 80% for the `Medium` and `Tight` operating points, respectively [99]. The electrons tagged by the `Tight` working point are a subset of electrons tagged by the `Medium` working point. Dedicated scale factors are needed to use these electron identification working points as well as the electron reconstruction.

There are several working points for the isolation category. They depend on the degree of separation of the electron from other objects and how widely the energy is distributed. They are determined based on how much of the energy deposit is centered in the range of $\Delta R < 0.2$, labelled as $p_{\mathrm{T}}^{\mathrm{topoetcone20}}$, with respect to the electron:

$$p_{\mathrm{T}}^{\mathrm{topoetcone20}}/p_{\mathrm{T}}^{e} < \max(3.5\ \mathrm{GeV}/p_{\mathrm{T}}^{e}, 0.015) \qquad \text{for } \texttt{FCHighPtCaloOnly}$$

$$p_{\mathrm{T}}^{\mathrm{topoetcone20}}/p_{\mathrm{T}}^{e} < 0.2 \qquad \text{for } \texttt{FCLoose}.$$

Scale factors for the isolation are also needed to be applied to ensure the data-to-MC agreement.

The definition of electrons used in analyses is summarized in Table 4.4. The “Baseline” electron definition is used to count up the number of leptons in an event. The “Leading” electron is defined base on the characteristic of electrons in the signal-like events, and is required at the event selection stage.

The electron used in this analysis has a flag called `Ambiguity`. This is a variable that indicates whether the reconstructed electron is a prompt electron or it is recognized as an electron from a photon conversion. Electrons from photon conversions often have a track with the opposite sign to the track associated to the

Table 4.4: Electron selection criteria.

Feature	Baseline electron	Leading electron
$\lvert\eta\rvert$	(0.0, 1.37] or [1.52, 2.47]	
p_T	> 25 GeV	> 200 GeV
Track to vertex association	$\lvert d_0/\sigma(d_0)\rvert < 5.0$ $\lvert\Delta z_0 \sin\theta\rvert < 0.5$ mm	
Identification	`Medium`	`Tight`
Isolation	`FCLoose`	`FCHighPtCaloOnly`

electron in the vicinity. In that case, `Ambiguity` > -1 is assigned, otherwise -1. The `Ambiguity` flag is a non-calibrated variable as a common ATLAS analysis one, so that possible shape variations are taken into account as discussed in Section 7.3.

4.7 Muon

Since muons have small energy loss due to bremsstrahlung, they pass through the calorimeter and leave information in muon spectrometers. In addition, they leave signals in the inner trackers as well. Reconstruction of muon, muon candidates are reconstructed in the inner tracker and muon spectrometer, and then they are combined by a matching algorithm [100].

There are several working points in the muon identification: `Loose`, `Medium`, `Tight` and `High-`p_T [101]. Muon identification depends on the number of hits in the detectors. `Medium` and `Tight` are used in this analysis. They requires two precision stations which have at least three hist in the MDT and CSC detectors. Muons passing `Tight` are a subset of those passing `Medium` and fulfil further requirements on compatibility of the charge to the momentum and absolute difference between the p_T observed in the inner tracker and muon spectrometer.

There are several working points in the muon isolation: `FCVeryLoose`, `FCLoose`, `FCMedium` and `FCTight` [101]. `FCTight` is used in this analysis. They depends on the energy spreadness in the inner tracker and calorimeter. Track-based isolation is defined as the scalar sum of the p_T of the tracks associated with the primary vertex in a given $\Delta R = \min(10\ \mathrm{GeV}/p_\mathrm{T}^{\mu}, 0.3)$ around the muon, excluding the track associated to the muon, labelled as $p_\mathrm{T}^{\mathrm{varcone30}}$. Calorimeter-based isolation is defined as the sum of the transverse energy of calorimeter cell clusters in a cone size of $\Delta R < 0.2$ around the muon subtracting the energy deposit of the muon itself, labelled as $E_\mathrm{T}^{\mathrm{topoetcone20}}$. `FCTight` requires the following conditions:

$$p_\mathrm{T}^{\mathrm{topoetcone20}}/p_\mathrm{T}^{\mu} < 0.15, \quad E_\mathrm{T}^{\mathrm{varcone30}}/p_\mathrm{T}^{\mu} < 0.04.$$

The reconstruction efficiency is measured by $Z \to \mu\mu$ events, and except for the region of $\lvert\eta\rvert < 0.1$, the efficiency is more than 98 %.

Two set of muon selection requirements are defined for this analysis. Muon satisfying these criteria are referred to as Baseline and Leading muons, as defined in Table 4.5. Leading muons are used in the signal region, while Baseline muons are used to count up the number of leptons in an event.

Table 4.5: Muon selection criteria.

Feature	Baseline muon	Leading muon
$\|\eta\|$	(0.0, 2.5]	
p_{T}	> 28 GeV	> 200 GeV
Track to vertex association	$\|d_0/\sigma(d_0)\| < 3.0$ $\|\Delta z_0 \sin\theta\| < 0.5$ mm	
Identification	`Medium`	`Tight`
Isolation	N/A	`FCTight`

The baseline muon does not require any isolation requirement in order to reconstruct the sub-leading muon without the influence of hadron activities from N_{R} decay. This can improves signal sensitivity especially in the low N_{R} mass region by a factor of 10.

4.8 Photon

Photons do not play an important role in this analysis, but they are used for the validation of the γ+jets estimation in the SR. The reconstruction of the photon depends on the measurement of the electromagnetic shower formed in the electromagnetic calorimeter. Rectangular clusters formed in the calorimeter cells are seeded to form the photons. It is also required that the energy deposit in the hadronic calorimeter be small or absent. Photons with no tracks associated with the cluster are called as ”unconverted photons”, while photons with a pair of oppositely-charged tracks are called as a ”converted photon” [102].

There are several working points in the photon identification: `Loose` and `Tight` [103]. The `Loose` selection depends on shower shapes in the second layer of the electromagnetic calorimeter and on the energy deposited in the hadronic calorimeter. The `Tight` selection requires additional information from the most inner layer of the calorimeter, and are separately optimised for unconverted and converted photons, to account for the generally broader lateral shower profile of the latter.

There are several working points in the photon isolation as well: `FCLoose`, `FCTight` and `FCTightCaloOnly`. They depend on the transverse energy flow in the calorimeter and inner tracker. The calorimeter isolation $E_{\mathrm{T,iso}}$ is obtained by summing the E_{T} in the calorimeter in cones around the direction of the photon candidate, $E_{\mathrm{T,iso}}^{\mathrm{topoetcone40}}$ for $\Delta R < 0.4$ and $E_{\mathrm{T,iso}}^{\mathrm{topoetcone20}}$ for $\Delta R < 0.2$. The track isolation $p_{\mathrm{T,iso}}$ is obtained by summing the p_{T} of all the tracks with p_{T} above 1 GeV excluding the tracks relating to photon conversions in a cone around the direction of the photon candidate with a fixed cone size of $\Delta R < 0.2$, labelled as $p_{\mathrm{T,iso}}^{\mathrm{etcone20}}$. `FCLoose` and `FCTightCaloOnly` are used in this analysis and they are defined as follows:

$$\begin{aligned} E_{\mathrm{T,iso}}^{\mathrm{topoetcone40}}/E_{\mathrm{T}}^{\gamma} &< 0.022 + 2.45\ \mathrm{GeV}/E_{\mathrm{T}}^{\gamma} && \text{for } \texttt{FCTightCaloOnly} \\ E_{\mathrm{T,iso}}^{\mathrm{topoetcone20}}/E_{\mathrm{T}}^{\gamma} < 0.065, \quad p_{\mathrm{T,iso}}^{\mathrm{etcone20}}/E_{\mathrm{T}}^{\gamma} &< 0.05 && \text{for } \texttt{FCLoose}. \end{aligned}$$

The reconstruction efficiency is measured depending on the photon energy [104]. The photon efficiency increases with increasing E_{T}, from about 60 % (50 %) for unconverted (converted) photon at $E_{\mathrm{T}} = 10$ GeV to over 90 % at $E_{\mathrm{T}} = 100$ GeV.

Two set of photon selection requirements are defined for this analysis. Photon satisfying these criteria are referred to as Baseline and Leading photons, as defined in Table 4.6. Baseline photons are used to count up the number of photons, while Leading photons are prepared to recognize signal like events.

Table 4.6: Photon selection criteria.

Feature	Baseline photon	Leading photon
$\lvert\eta\rvert$	(0.0, 1.37] or [1.52, 2.47]	
p_{T}	> 25 GeV	> 200 GeV
Identification	`Loose`	`Tight`
Isolation	`FCLoose`	`FCTightCaloOnly`

4.9 Overlap removal

The above objects are reconstructed in parallel by combining the detector information. There are many cases where a single particle is reconstructed as different objects. For example, since electrons and jets leave similar signals in the calorimeter, they are often reconstructed as both objects. To avoid double counting of a single particle, a procedure called “overlap removal“ is applied by following procedures shown in Table 4.7.

Table 4.7: The order of overlap removal. Baseline leptons shown in Table 4.4 and 4.5 and photon shown in Table 4.6 are used in below overlap removal prescription. ΔR is calculated by $\sqrt{(\phi_{\text{Reference}} - \phi_{\text{Target}})^2 + (y_{\text{Reference}} - y_{\text{Target}})^2}$ where y denotes the rapidity.

Step	Reference	Target	Criterion
1.	Electron	Electron	If there is a shared track, softer electron is discarded.
2.	Muon	Electron	If there is a shared track, any electrons are discarded.
3.	Electron	Muon	If there is a shared track, any muons are discarded.
4.	Jet	Electron	If $\Delta R < 0.2$ and jet is not b-tagged and electron p_{T} is greater than 100 GeV, any electrons are discarded.
5.	Electron	Jet	If $\Delta R < 0.4$, any jets are discarded.
6.	Muon	Jet	If $\Delta R < 0.4$, any muons are discarded.

In many typical ATLAS analyses, the jet-muon overlap removal (jets and muons are used as reference and target object, respectively) is performed. However, in this analysis, this overlap removal is not used to improve the reconstruction efficiency of the sub-leading muons.

For an event with electrons in the final state, as described in Section 5, one electron and two electrons channels are defined. With the same analogy, one muon channel can be defined. However there is a significant disadvantage in one muon channel. Due to the lack of sub-leading muon, its energy deposit can not be handled and W_{R} and N_{R} mass reconstructions become inaccurate. It is mainly noticeable when the sub-leading muon is generated close to the large-R jet, resulting in a significant loss of sensitivity in phase space where $N_{\mathrm{R}}/\,W_{\mathrm{R}}$ is small.

4.10 Missing Transverse Energy ($E_{\mathrm{T}}^{\mathrm{miss}}$)

Since the LHC is a proton-proton collision experiment, only transverse energy is conserved to be zero. Longitudinal energy is not conserved because the energies of the quarks and gluons in the protons are not determined. Therefore, if there is a bias in the reconstructed energy distribution in the x-y plane, it is interpreted as an invisible particle, like a neutrino, flying in the opposite direction of the bias, which can't be observed by detector. Hence, by using the vector sum of the reconstructed object's energy, the missing transverse energy ($E_{\mathrm{T}}^{\mathrm{miss}}$) is defined as follows.

$$E_{\mathrm{T}}^{\mathrm{miss}} = -\sum E_{\mathrm{T}}^{\mathrm{jet}} - \sum E_{\mathrm{T}}^{\mathrm{e}} - \sum E_{\mathrm{T}}^{\mu} - \sum E_{\mathrm{T}}^{\gamma} - \sum E_{\mathrm{T}}^{\text{soft term}}$$

where $\sum E_{\mathrm{T}}^{\mathrm{jet}}$, $\sum E_{\mathrm{T}}^{\mathrm{e}}$, $\sum E_{\mathrm{T}}^{\mu}$ and $\sum E_{\mathrm{T}}^{\gamma}$ are the transverse energy obtained from the vector sum of reconstructed jets, electrons, muons, and photons, respectively. The soft term, $\sum E_{\mathrm{T}}^{\text{soft term}}$, is defined as the vector sum of tracks derived from the primary vertex, but not used for other object reconstructions [105].

Among the components of the $E_{\mathrm{T}}^{\mathrm{miss}}$, hard terms have their own dedicated energy calibration system, so it is only necessary to estimate the uncertainties derived from the soft term. These uncertainties are estimated by decomposing the soft term into two components, one perpendicular to the hard term and the other parallel to the hard term, and comparing the data and MC.

4.11 Large radius jet

The reconstruction of hadronically-decaying heavy particles often form a large radius jet (large-R jet). It means that it is possible to reconstruct most of the decay particles derived from a heavy particle as a single jet, which is often used in new particle searches.

The large-R jets are reconstructed by combining calibrated small-R jets by using the anti-k_t algorithm with a radius parameter of 1.0 [106]. These large-R jets are trimmed by discarding any constituent small-R jets which have less than 5% of a large-R jet's p_{T}.

The largest advantage of combining small-R jets to form large-R jets is that large-R jets with small masses can be used for analysis. Since large-R jets are used for the purpose of reconstructing decay products from N_{R}, this helps in the search for signals with small N_{R} masses. Also, by using calibrated small-R jets, there is no need to consider additional systematic uncertainty for the large-R jets.

5 Event selection

In this section event level criteria to define signal regions are discussed. These criteria are optimized to maximize $S/\sqrt{B}$, where S and B indicate the number of signal and background events, for a benchmark signal mass point for each signal region. The benchmark mass point is selected from the mass points not excluded in the previous analysis. It is confirmed that the optimization does not depend significantly on the signal mass point used as a benchmark.

In the signal events, very high-p_{T} lepton and right-handed neutrino N_{R} from W_{R} decay are produced back-to-back in the x-y plane. In this topology, the angular distance between two quarks from N_{R} decay is getting small depending on ΔM, and they form a single large-R jet in the detector level reconstruction. In this analysis, at least two quarks of N_{R} origin can not be separated and are components of the large-R jet. For higher ΔM signals, the large-R jet geometrically overlaps with the lepton from the N_{R} decay.

In the muon channel, this second muon can be identified even for very high ΔM signals, since muon-jet overlap removal and any isolation requirements for sub-leading muon are deactivated. Signal region is defined by requiring two muons in an event (SR2mu).

On the other hand, electrons are reconstructed using calorimeter in the similar way as jets, so the electron from N_{R} decay is indistinguishable from jets depending on the mass difference between W_{R} and N_{R}. Therefore, signal regions are defined according to the number of electrons in an event (SR1e and SR2e has exactly one and two reconstructed electron, respectively).

The final discriminant is the W_{R} mass reconstructed with the large-R jet and the leading lepton ($m_{\ell J}$) for SR1e, and the large-R jet and two leptons ($m_{\ell\ell J}$) for SR2e and SR2mu. Every signal regions are required to have W_{R} mass greater than 3 TeV and regions with W_{R} mass less than 3 TeV are used as control or validation regions. More details of region definitions for control and validation regions can be found in Section 6.

In this analysis, following seven background processes are considered: W+jets, QCD multi-jet, γ+jets, Z+jets, $t\bar{t}$, single-top and di-boson. Other minor processes account for less than 1 % and they are negligibly small.

5.1 Preselection

Number of large-*R* jets

Exactly one large-R jet in an event is required. As shown in Figure 5.1(a), 5.2(a) and 5.3(a), about 90 % of the signal events have only one large-R jet. Especially in one electron channel, limiting the number of objects in an event has the advantage to ensure that the kinematics of the QCD multi-jet can be well modeled by using the leading order MC samples except for its normalization.

Table 5.1: Definition of the signal regions.

Variable	SR1e	SR2e	SR2mu
Number of large-R jets	1		
Number of electrons	1	2	0
Number of muons	0	0	2
Number of additional leptons	0		
Number of b-tagged jets	0		
Leading lepton p_{T}	$>$ 200 GeV		
Leading lepton identification	`LHTight`		`Tight`
Leading lepton isolation	`FCHighPtCaloOnly`		`FCTight`
Sub-leading lepton p_{T}	N/A	$>$ 26 GeV	$>$ 28 GeV
$E_{\mathrm{T}}^{\mathrm{miss}}$	$<$ 200 GeV		N/A
$\cos\theta$	$>$ 0.7	N/A	
$\Delta\eta$ between large-R jet and electron	$<$ 2.0	N/A	
$\Delta\phi$ between large-R jet and leading lepton	$>$ 2.0		
Di-lepton p_{T}	N/A		$>$ 200 GeV
Di-lepton mass	N/A	$>$ 200 GeV	
W_{R} mass	$>$ 3 TeV		

Leading lepton selection

The lepton from W_{R} decay, which is called the leading lepton, is highly boosted and well isolated. Since the target W_{R} mass is TeV scale, similar p_{T} with a large-R jet can be expected for the leading lepton. Thus, same p_{T} threshold with large-R jet of 200 GeV is used. The p_{T} distribution for each SR is shown in Figure 5.1(b), 5.2(b) and 5.3(b). In addition, since the leading lepton is found in a clean environment, the tighter identification and isolation shown in Section 4.6 and 4.7 are imposed.

$\Delta\phi$ between the leading lepton and large-R jet

Since the mass of W_{R} is assumed to be heavy, the momentum of the W_{R} is small and the leading electron and the large-R jet from a W_{R} decay is produced back-to-back in the x-y plane. To enhance such topology, $\Delta\phi > 2.0$ is applied as shown in Figure 5.1(c), 5.2(c) and 5.3(c).

Number of b-tagged jets

Most of the $t\bar{t}$ and single top background events have at least one b-tagged jet as shown in Figure 5.1(d), 5.2(d) and 5.3(d). To suppress them, zero b-tagged jet in an event is required. Especially in two lepton channels, the number of $t\bar{t}$ can be reduced by a factor of 10, allowing it to be treated as a minor background.

5.2 Definition of one electron signal region (SR1e)

SR1e is introduced to improve the sensitivity in the largest ΔM phase space. It requires exactly one reconstructed electron from W_{R} decay and one large-R jet reconstructed from the entire decay products of the N_{R} ($N_{\mathrm{R}} \to eqq' \to J$). The large-$R$ jet mass is expected to peak around the N_{R} mass. The signal region is optimized for the signal events at the benchmark mass point $(m(W_{\mathrm{R}}), m(N_{\mathrm{R}}))$ = (5 TeV, 50 GeV) against the SM background events.

$\Delta\eta$ between the electron and the large-R jet

In terms of the suppression of QCD multi-jet and γ+jets events, $\Delta\eta = |\eta_e - \eta_J| < 2.0$ is applied. The background events produced in a t-channel diagram with a large W_{R} mass tend to have a large $\Delta\eta$. On the other hand, the most of the on-shell W_{R} signals are generated in s-channel process and they have smaller $\Delta\eta$ as shown Figure 5.5(a). With this criterion, QCD multi-jet and γ+jets events can be reduced by a factor of 4.

Missing transverse energy ($E_{\mathrm{T}}^{\mathrm{miss}}$)

While signal events ideally have zero $E_{\mathrm{T}}^{\mathrm{miss}}$, some background processes, in particular W+jets, $t\bar{t}$ and single top, have real $E_{\mathrm{T}}^{\mathrm{miss}}$ from neutrinos. The $E_{\mathrm{T}}^{\mathrm{miss}}$ upper cut can reduce a part of them as shown in Figure 5.5(b); the $E_{\mathrm{T}}^{\mathrm{miss}}$ is required to be smaller than 200 GeV. Furthermore, $E_{\mathrm{T}}^{\mathrm{miss}}$ is used to define the control and validation regions for background estimation described in Section 6.1.

Decay angle by assuming $W \to e\nu$ decay ($\cos\theta$)

Due to the upper cut on the $E_{\mathrm{T}}^{\mathrm{miss}}$ and leading lepton p_{T}, the W+jets events are strongly biased to have a large $\cos\theta$ where θ is the decay angle of the electron from W_L boson decay in the rest frame of the W_L boson. The W_L boson rest frame is computed from $E_{\mathrm{T}}^{\mathrm{miss}}$ and the leading electron by assuming that the W_L boson mass is 80.4 GeV and $E_{\mathrm{T}}^{\mathrm{miss}}$ is derived only from a neutrino by solving the following equations for $p_{\nu,z}$.

$$\begin{aligned} E_{\mathrm{T}}^{\mathrm{miss}} &= \sqrt{p_{\nu,x}^2 + p_{\nu,y}^2} \\ M_W^2 &= (E_e + E_\nu)^2 - (\vec{p}_e + \vec{p}_\nu)^2 \\ E_\nu &= \sqrt{p_{\nu,x}^2 + p_{\nu,y}^2 + p_{\nu,z}^2} \end{aligned}$$

The $p_{\nu,z}$ can have an imaginary value. In that case, the imaginary part is discarded and the only real part is used for the cosθ calculation. When two real different solutions are available, the lowest solution is selected. To enhance the signal events, as shown in Figure 5.5(c), cos$\theta > 0.7$ is applied.

The definition of SR1e is summarized in Table 5.1. The mass distribution is shown in Figure 5.5(d). After applying all of the selections above, the number of background in the signal region is found to be 12.7±3.2, while the signal is 25.8±5.1 at the pre-fit level, corresponding to $S/\sqrt{B} = 7.1$ for 139 fb^{-1}.

The most dominant background processes in the signal region are $W(\to e\nu)$+jets, QCD multi-jet and γ+jets events shown in Figure 5.4.

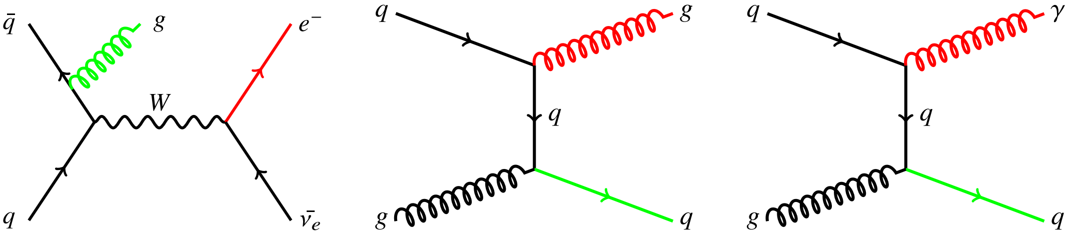

(a) $W(\rightarrow e\nu)$+jets (b) QCD multi-jet (c) γ+jets

Figure 5.4: Feynman diagrams of dominant backgrounds in SR1e. The red and green colored particles are reconstructed as electrons and large-R jets, respectively.

5.3 Definition of two electron signal region (SR2e)

At the intermediate ΔM phase space, a second electron can be identified close to the large-R jet as shown in Figure 5.9(b). Sub-leading electron p_{T} distribution can be found in Figure 5.9(a). By requiring it, smaller background events are expected than SR1e. SR2e is optimized to maximize the sensitivity for the signal events at the benchmark mass point $(m(W_{\mathrm{R}}), m(N_{\mathrm{R}}))$ = (5 TeV, 500 GeV) against the SM background events. Events with exactly two electrons and one large-R jet in an event are selected.

Di-electron mass

The two electrons' invariant mass peaks around Z boson mass as shown in Figure 5.6(a). Di-electron mass greater than 200 GeV is required. This cut decreases the Z+jets yields by a factor of 100.

$E_{\mathrm{T}}^{\mathrm{miss}}$

For further reduction of W+jets and $t\bar{t}$ events, $E_{\mathrm{T}}^{\mathrm{miss}} < 200$ GeV is applied as shown in Figure 5.6(b).

The definition of SR2e is summarized in Table 5.1. The mass distribution is shown in Figure 5.6(c). After applying all of the selections above, the number of background in the signal region is found to be 13.3 ± 3.6, while the signal is 25.8 ± 5.1 at the pre-fit level, corresponding to $S/\sqrt{B} = 7.1$ for 139 fb^{-1}.

The most dominant background process in the signal region is the $Z(\rightarrow ee)$+jets shown in Figure 5.7(a). The contributions from QCD multi-jet and γ+jets processes are negligibly small.

5.4 Definition of two muon signal region (SR2mu)

SR2mu is optimized to maximize the sensitivity for the signal events at the benchmark mass point $(m(W_{\mathrm{R}}), m(N_{\mathrm{R}}))$ = (5 TeV, 500 GeV) against the SM background events. Events with exactly two muons and one large-R jet in an event are selected. Sub-leading muon p_{T} and ΔR between the large-R jet distributions are shown in Figure 5.9(c) and 5.9(d), respectively. Sub-leading muon can be identified close to the large-R jet.

Di-muon mass

The two muons' invariant mass peaks around Z boson mass as shown in Figure 5.8(a). Thus, di-muon mass greater than 200 GeV is required as well as SR2e. This cut decreases the Z+jets yields by a factor of 100.

Di-muon p_T

To suppress the contribution from top-quark related background as shown in Figure 5.8(b). di-muon p_T greater than 200 GeV cut is also applied. Due to the high p_T muon from W_R decay, its resolution getting worse. To keep the signal efficiency, any $E_\mathrm{T}^\mathrm{miss}$ cut is not employed.

The definition of SR2mu is summarized in Table 5.1. The mass distribution is shown in Figure 5.8(c). After applying all of the selections above, the number of background in the signal region is found to be 5.3±2.5, while the signal is 22.6±4.3 at the pre-fit level, corresponding to $S/\sqrt{B} = 9.2$ for 139 fb^{-1}.

The most dominant process in the signal region is the $Z(\rightarrow \mu\mu)$+jets shown in Figure 5.7(b).

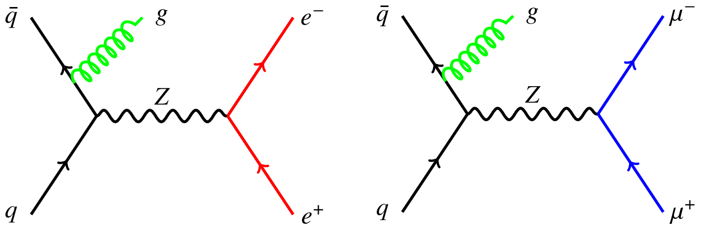

(a) $Z(\rightarrow ee)$+jets (b) $Z(\rightarrow \mu\mu)$+jets

Figure 5.7: Feynman diagrams of dominant backgrounds in SR2e and SR2mu. The red, blue and green colored particles are reconstructed as electrons, muons and large-R jets, respectively.

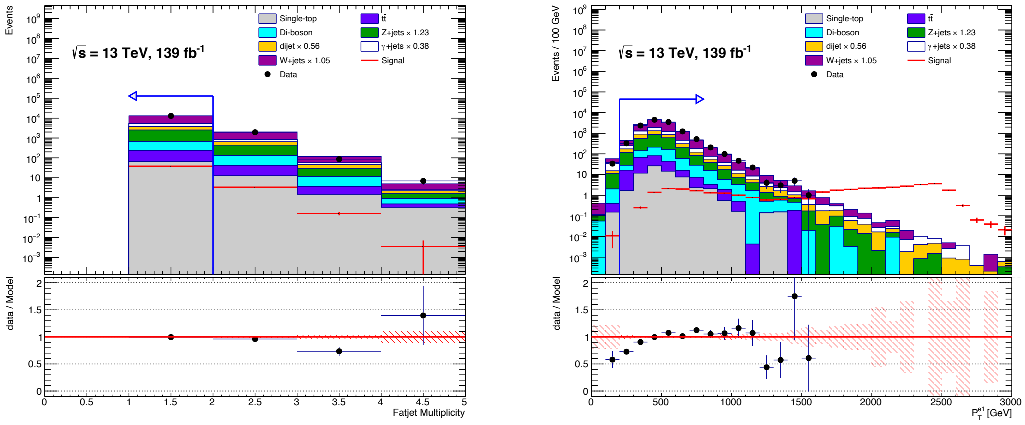

(a) Large-R jet multiplicity

(b) Electron p_T

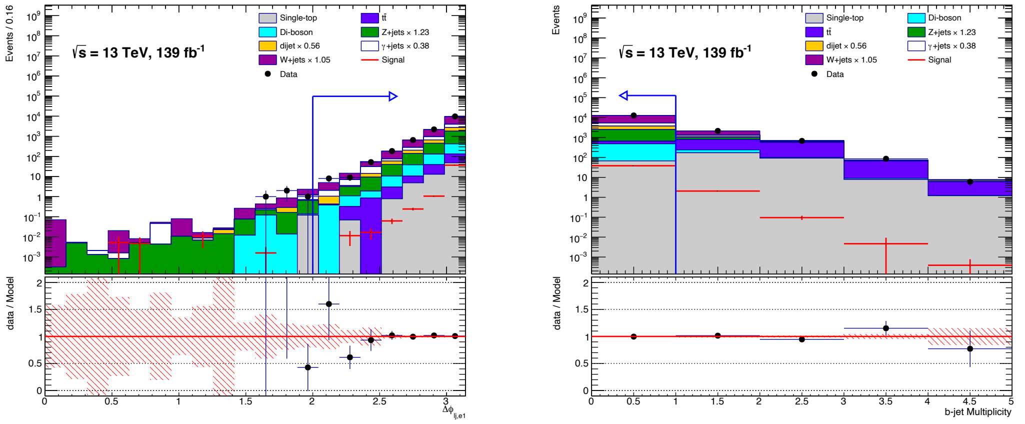

(c) $\Delta\phi$ between large-R jet and electron

(d) b-tagged jet multiplicity

Figure 5.1: Distributions of variables used in the preselection in one electron channel. The red histograms represent the shape of the reference signal events of $(m(W_R), m(N_R)) = (5\text{ TeV}, 50\text{ GeV})$. Overflowed and underflowed events are merged in the closest bin in each distribution. Blue vertical line and horizontal arrow show the value and direction of a certain cut to define SR1e, respectively. All the cuts enumerated in Table 5.1 except a variable shown in each sub-label are applied. (a) shows the large-R jet multiplicity distribution. (b) shows the electron p_T distribution. (c) shows the $\Delta\phi$ between large-R jet and electron distribution. (d) shows the b-tagged jet multiplicity distribution. The number of W+jets, QCD multi-jet, γ+jets and Z+jets yields are normalized with normalization factors shown in the legend which are obtained by dedicated CRs. The ratios of data over MC and statistical uncertainties are displayed as black points and red hashed histograms in the bottom panels, respectively.

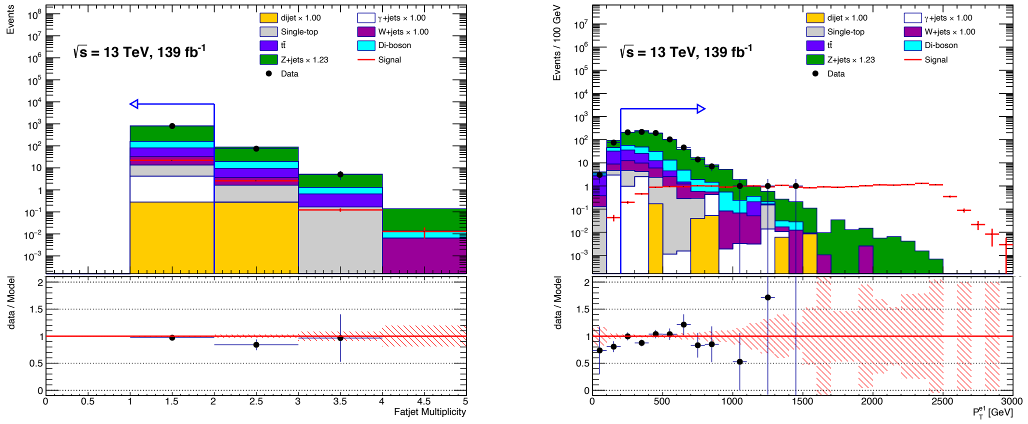

(a) Large-R jet multiplicity

(b) Leading electron p_T

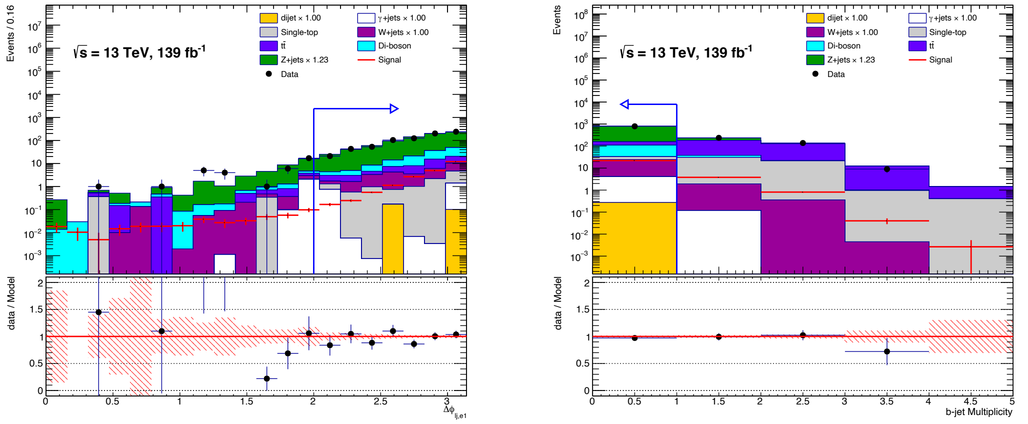

(c) $\Delta\phi$ between large-R jet and electron

(d) b-tagged jet multiplicity

Figure 5.2: Distributions of variables used in the preselection in two electron channel. The red histograms represent the shape of the reference signal events of $(m(W_R), m(N_R))$ = (5 TeV, 500 GeV). Overflowed and underflowed events are merged in the closest bin in each distribution. Blue vertical line and horizontal arrow show the value and direction of a certain cut to define SR2e, respectively. Every cuts enumerated in Table 5.1 except a variable shown in each sub-label are applied. (a) shows the large-R jet multiplicity distribution. (b) shows the leading electron p_T distribution. (c) shows the $\Delta\phi$ between large-R jet and leading electron distribution. (d) shows the b-tagged jet multiplicity distribution. The number of Z+jets yield is normalized with a normalization factor shown in the legend which is obtained by a dedicated CR. The ratios of data over MC and statistical uncertainties are displayed as black points and red hashed histograms in the bottom panels, respectively.

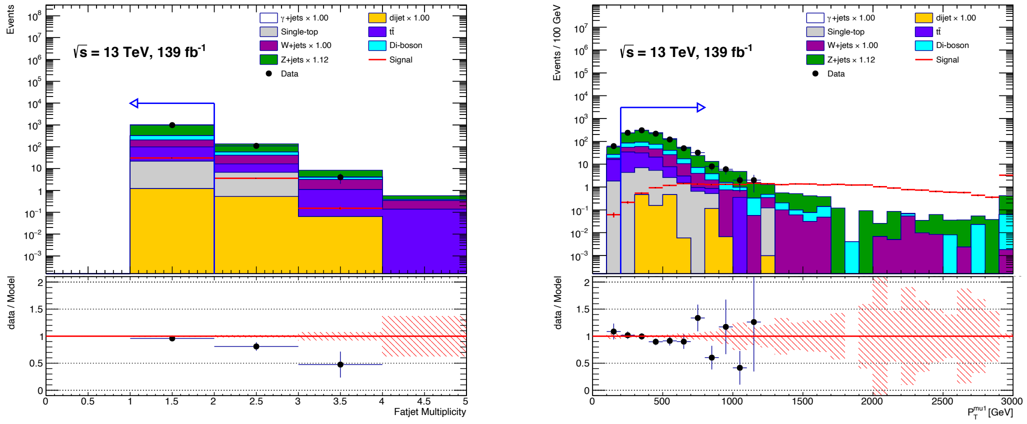

(a) Large-R jet multiplicity

(b) Leading muon p_T

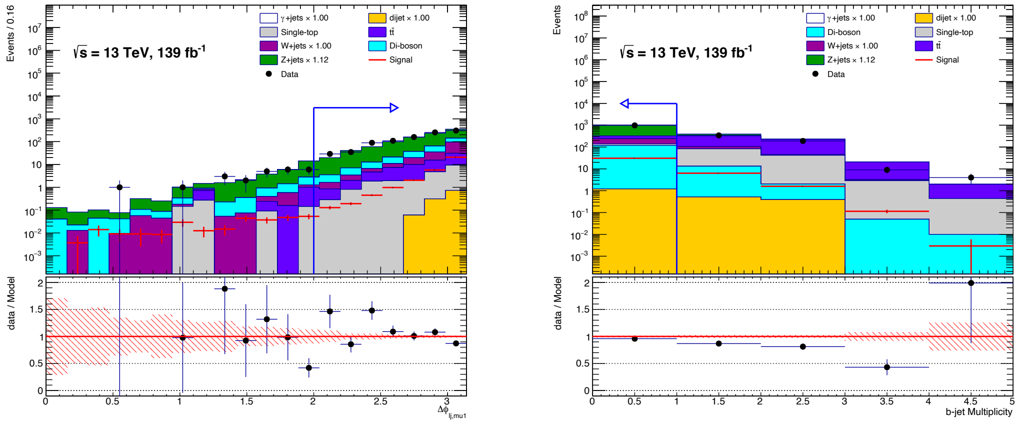

(c) $\Delta\phi$ between large-R jet and muon

(d) b-tagged jet multiplicity

Figure 5.3: Distributions of variables used in the preselection in two muon channel. The red histograms represent the shape of the reference signal events of $(m(W_R), m(N_R))$ = (5 TeV, 500 GeV). Overflowed and underflowed events are merged in the closest bin in each distribution. Blue vertical line and horizontal arrow show the value and direction of a certain cut to define SR2mu, respectively. Every cuts enumerated in Table 5.1 except a variable shown in each sub-label are applied. (a) shows the large-R jet multiplicity distribution. (b) shows the leading muon p_T distribution. (c) shows the $\Delta\phi$ between large-R jet and leading muon distribution. (d) shows the b-tagged jet multiplicity distribution. The number of Z+jets yield is normalized with a normalization factor shown in the legend which is obtained by a dedicated CR. The ratios of data over MC and statistical uncertainties are displayed as black points and red hashed histograms in the bottom panels, respectively.

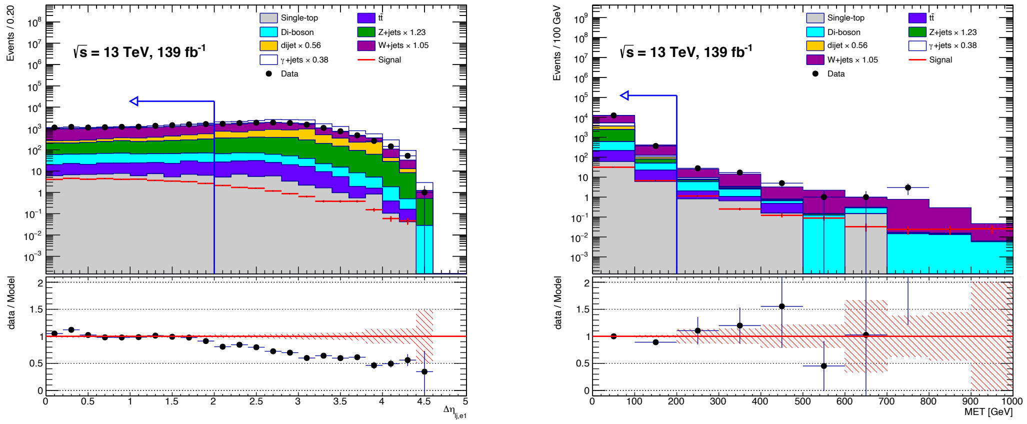

(a) $\Delta\eta$ between electron and large-R jet

(b) $E_{\mathrm{T}}^{\mathrm{miss}}$

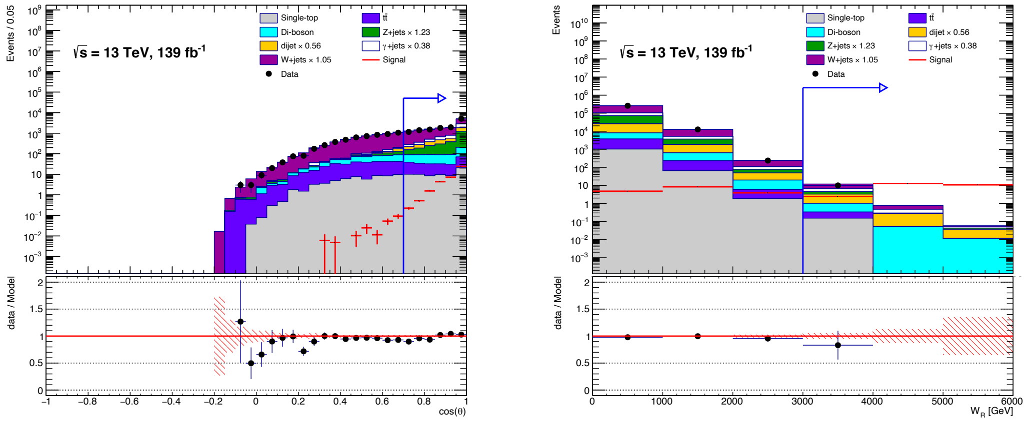

(c) $\cos\theta$

(d) m_{eJ}

Figure 5.5: Distributions of variables used in the additional selection in one electron channel. The red histograms represent the shape of the reference signal events of $(m(W_{\mathrm{R}}), m(N_{\mathrm{R}})) = (5\,\mathrm{TeV}, 50\,\mathrm{GeV})$. Overflowed and underflowed events are merged in the closest bin in each distribution. Blue vertical line and horizontal arrow show the value and direction of a certain cut to define SR1e, respectively. All cuts enumerated in Table 5.1 except a variable shown in each sub-label are applied. (a) shows the $\Delta\eta$ between large-R jet and electron distribution. (b) shows the $E_{\mathrm{T}}^{\mathrm{miss}}$ distribution. (c) shows the distribution of the electron helicity angle computed by assuming the standard model W boson decay. Due to the relatively balanced electron p_{T} and $E_{\mathrm{T}}^{\mathrm{miss}}$, W+jets, $t\bar{t}$, diboson and single top background have a wide distribution. On the other hand, QCD multi-jet and Z+jets backgrounds which have no $E_{\mathrm{T}}^{\mathrm{miss}}$ in truth level mainly are biased in the large value side. (d) shows the distribution of invariant mass of a large-R jet and an electron which corresponds to W_{R} mass. The number of W+jets, QCD multi-jet, γ+jets and Z+jets yields are normalized with normalization factors shown in the legend which are obtained by dedicated CRs. The ratios of data over MC and statistical uncertainties are displayed as black points and red hashed histograms in the bottom panels, respectively.

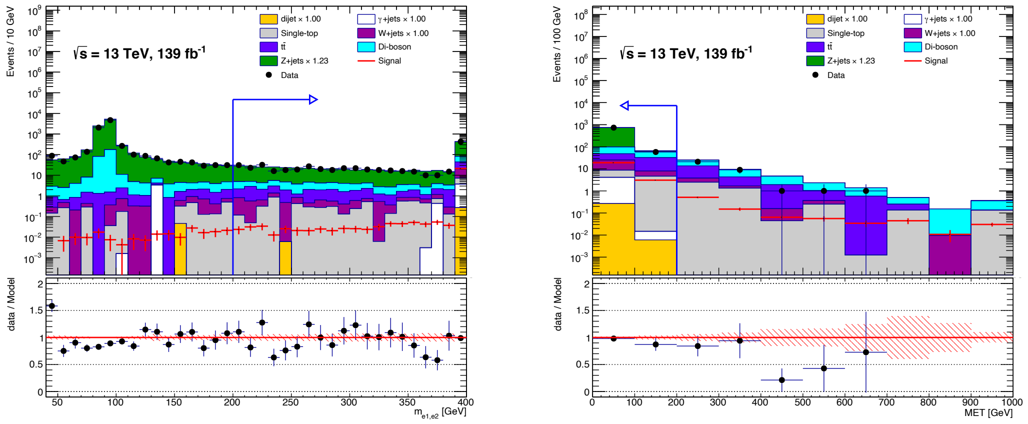

(a) Di-electron mass

(b) $E_{\mathrm{T}}^{\mathrm{miss}}$

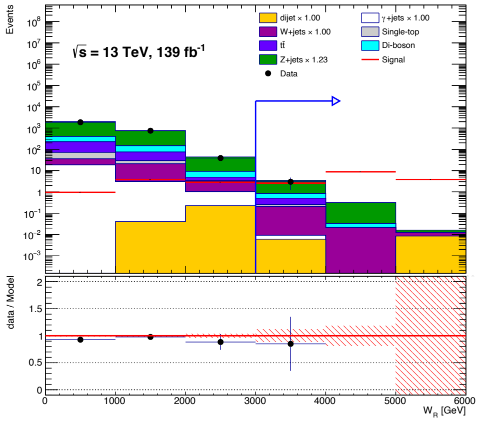

(c) m_{eeJ}

Figure 5.6: Distributions of variables used in thee additional selection in two electron channel. The red histograms represent the shape of the reference signal events of $(m(W_{\mathrm{R}}),\ m(N_{\mathrm{R}})) = (5\ \mathrm{TeV},\ 500\ \mathrm{GeV})$. Overflowed and underflowed events are merged in the closest bin in each distribution. Blue vertical line and horizontal arrow show the value and direction of a certain cut to define SR2e, respectively. All cuts enumerated in Table 5.1 except a variable shown in each sub-label are applied. (a) shows the di-electron mass distribution. (b) shows the $E_{\mathrm{T}}^{\mathrm{miss}}$ distribution. (c) shows the distribution of invariant mass of a large-R jet and two electrons which corresponds to W_{R} mass. The number Z+jets yield is normalized with a normalization factor shown in the legend which is obtained by a dedicated CR. The ratios of data over MC and statistical uncertainties are displayed as black points and red hashed histograms in the bottom panels, respectively.

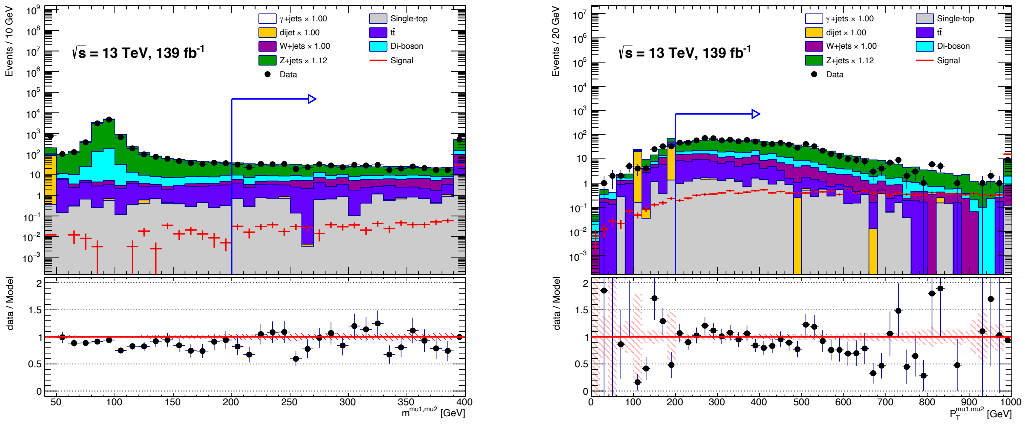

(a) Di-muon mass

(b) Di-muon p_{T}

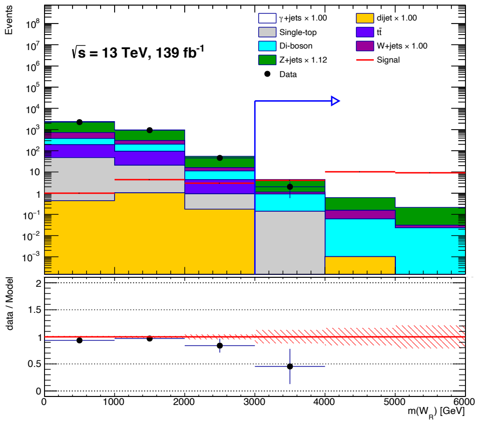

(c) $m_{\mu\mu J}$

Figure 5.8: Distributions of variables used in the additional selection in two muon channel. The red histograms represent the shape of the reference signal events of $(m(W_{\mathrm{R}}),\ m(N_{\mathrm{R}})) = (5\ \text{TeV},\ 500\ \text{GeV})$. Overflowed and underflowed events are merged in the closest bin in each distribution. Blue vertical line and horizontal arrow show the value and direction of a certain cut to define SR2mu, respectively. All cuts enumerated in Table 5.1 except a variable shown in each sub-label are applied. (a) shows the di-muon mass distribution. (b) shows the di-muon p_{T} distribution. (c) shows the distribution of invariant mass of a large-R jet and two muons which corresponds to W_{R} mass. The number of Z+jets yield is normalized with a normalization factor which is obtained by a dedicated CR. The ratios of data over MC and statistical uncertainties are displayed as black points and red histograms in the bottom panels, respectively.

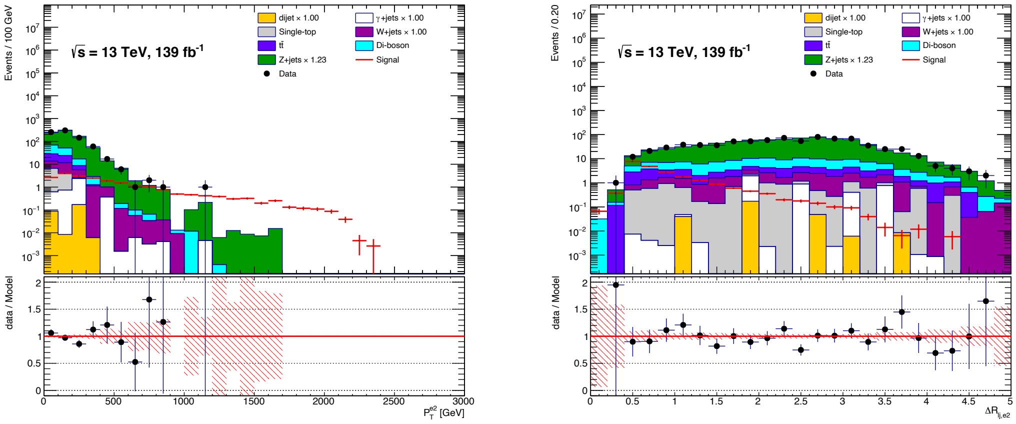

(a) Sub-leading electron p_{T} (b) ΔR between large-R jet and sub-leading electron

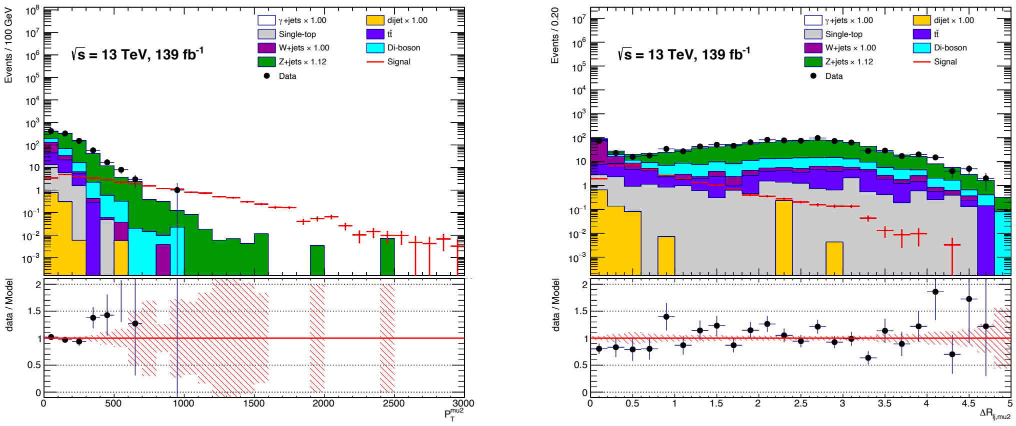

(c) Sub-leading muon p_{T} (d) ΔR between large-R jet and sub-leading muon

Figure 5.9: Distributions of variables related to the sub-leading leptons. The red histograms represent the shape of the reference signal events of $(m(W_{\mathrm{R}}),\ m(N_{\mathrm{R}}))$ = (5 TeV, 500 GeV). Overflowed and underflowed events are merged in the closest bin in each distribution. (a) shows the sub-leading electron p_{T} distribution. (b) shows the ΔR between large-R jet and sub-leading electron distribution. (c) shows the sub-leading muon p_{T} distribution. (d) shows the ΔR between large-R jet and sub-leading muon distribution. The number of Z+jets yield is normalized with a normalization factor which is obtained by a dedicated CR. The ratios of data over MC and statistical uncertainties are displayed as black points and red histograms in the bottom panels, respectively.

5.5 Binning in signal regions

The signal sensitivities are improved by modifying the binning of the final discriminant observable of $m(W_\mathrm{R})$ taking into account the W_R mass resolution of the signal events and the stability of the background estimation. For both electron and muon final states, the expected exclusion limits are evaluated for the following three different configurations.

A: 1-bin signal regions.

B: 2-bin signal regions with a fixed bin width of 1 TeV: [3,4] TeV and > 4 TeV.

C: 3-bin signal regions with a fixed bin width of 1 TeV: [3,4] TeV, (4,5] TeV and > 5 TeV.

These configurations are visualized in Figure 5.10.

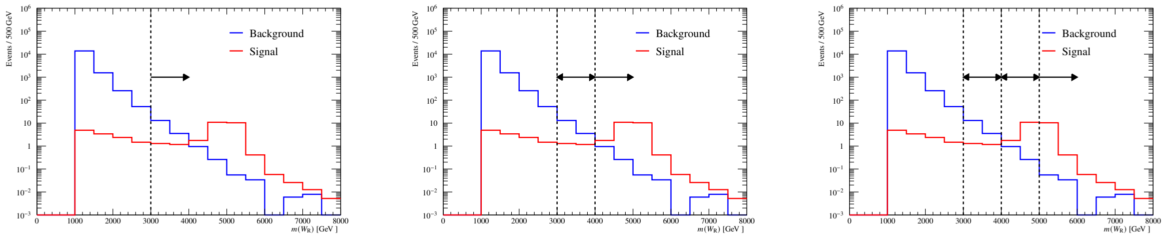

(a) Configuration A (b) Configuration B (c) Configuration C

Figure 5.10: The schematic views of configuration A, B and C are visualized in (a), (b) and (c), respectively. The black dashed lines and arrows indicate the thresholds and widths of bins. Blue and red histograms show the W_R mass distributions of background and signal, respectively. The signal with the mass point of $(m(W_\mathrm{R}), m(N_\mathrm{R}))$ = (5 TeV, 50 GeV) is used as a benchmark mass point. The all background distributions are given by one electron channel.

The expected limits with each configuration are visualized in Figure 5.11. The differences between configurations A to B are large, about 700 GeV and 500 GeV gain in $m(W_\mathrm{R})$ is expected for electron and muon channel, respectively. On the other hand, the difference between configurations B to C is relatively small, about a few hundreds GeV. Especially in the muon channel, the maximum gain is only about 100 GeV. The improvement in the region with the smallest N_R in the electron channel is the largest. This is due to the large reduction in the number of background events in the heaviest W_R mass region in the one electron channel.

Seemingly, configuration C appears to be the best, but as the number of bins is increased, the number of background events becomes too small in the bin with the heaviest $m(W_\mathrm{R})$, making it difficult to perform background estimation. Especially in one electron channel, the number of W+jets MC sample in above 5 TeV is expected to be exactly zero and that requires smoothing or other processing of the $m(W_\mathrm{R})$ distribution. To avoid such a processing in this analysis, the 2-bin signal region with a fixed bin width of 1 TeV (Configuration B) is chosen for all signal regions.

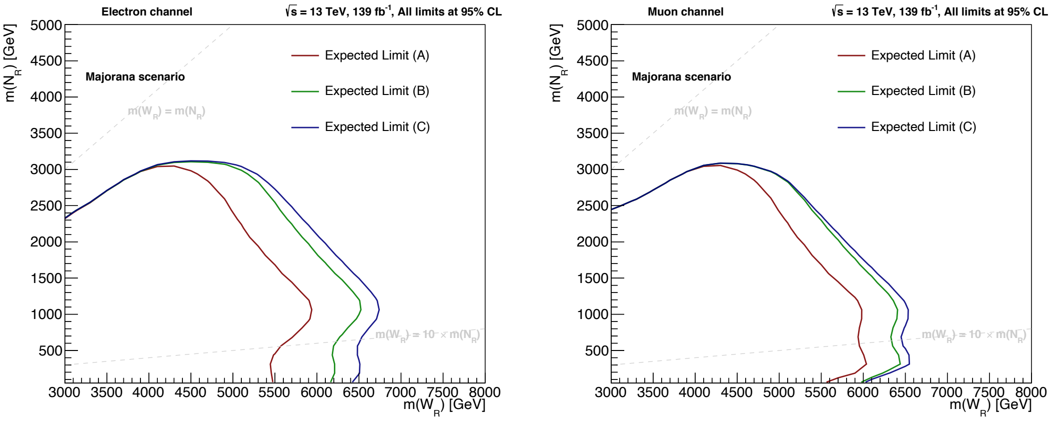

(a) Electron

(b) Muon

Figure 5.11: (a) The expected 95 % CL upper limits for electron channel. (b) The expected 95 % CL upper limits for muon channel. Only statistical uncertainties are considered in every plots. The expected exclusions with configuration (A), (B) and (C) are shown as red, green and blue lines, respectively.

6 Background estimation

In this section, the methods of background estimation are described. The number of events for the major background processes in SRs are estimated by applying correction factors to the simulated events. These correction factors are obtained by adjusting the number of background events in the simulation to those in the observed data in specific control regions (CRs). The correction factor is called a normalization factor (NF) and this method is called the “semi-data driven method”:

$$N^{\text{post-fit}}_{\text{SR, MC}} = \frac{N_{\text{CR, data}}}{N^{\text{pre-fit}}_{\text{CR, MC}}} \times N^{\text{pre-fit}}_{\text{SR, MC}} = NF \times N^{\text{pre-fit}}_{\text{SR, MC}}.$$

Estimating background is assumed that the ratio of CR to SR is well modeled by the simulation. Each major background has unique CRs and its NF is calculated individually while taking into account the impact of systematic uncertainties, which are discussed in more details in Section 7.3. For minor background processes, the number of events is estimated based only on MC.

In the following discussion, “pre-fit” and “post-fit” are defined as the state before and after the NFs are multiplied by the major background events, respectively.

Validation regions (VRs) are also used for the purpose to test background event estimations. There are following two types of VRs.

Extra VRs

For each major background, the assumption that the ratio of CR to SR is well modeled by the MC must be checked. This is a so-called shape modeling check and the extra VRs are defined for this purpose. NFs in extra VRs can be different from those obtained the CRs. Since extra VRs are set to have completely orthogonal phase spaces with the SRs, the signal contamination is negligibly small.

Standard VRs

They are defined in regions between SRs and CRs and used for the purpose of confirming that the NFs obtained in CRs work properly. The same NFs are applied in the standard VRs as SRs.

As introduced in Section 5, the names of the SRs are defined based on the number of leptons, i.e. SR1e, SR2e, and SR2mu. The names of CRs and standard VRs are also based on the number of leptons, lepton flavor and the name of background process estimated in that region. The definitions of extra VRs follow those of actual CRs/SRs. Therefore, their names depend on the target background process and which region is mimicked.

The detail of background estimation method for SR1e, SR2e and SR2mu is explained in the following sections. The schematic pictures of the all SRs, CRs and standard VRs are shown in Figure 6.1.

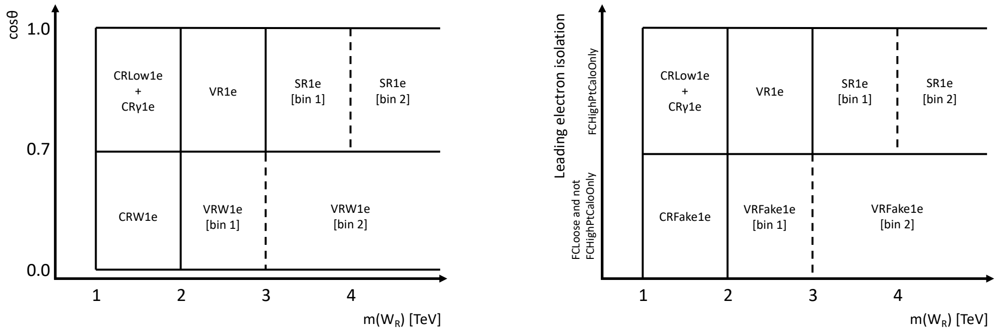

(a) Regions relating W+jets process

(b) Regions relating QCD multi-jet process

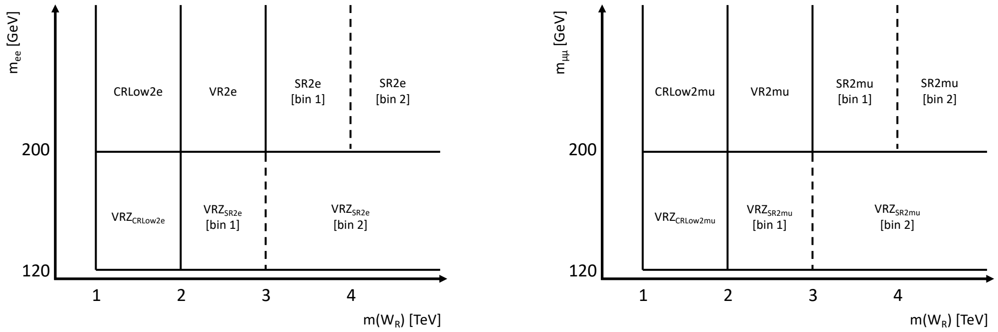

(c) Regions relating $Z(\to ee)$+jets process

(d) Regions relating $Z(\to \mu\mu)$+jets process

Figure 6.1: Schematic views of region definitions. (a) shows the regions relating for W+jets estimation. (b) shows the regions relating QCD multi-jet estimation. (c) shows the regions relating $Z(\to ee)$+jets estimation. (d) shows the regions relating $Z(\to \mu\mu)$+jets estimation.

6.1 Background estimation method for SR1e

The dominant SM background processes in SR1e are W+jets (40%), QCD multi-jet with a misidentified electron (20%) and γ+jets with an electron from photon conversion (20%). To estimate these background contributions, CRLow1e, CRW1e, CRFake1e and CRγ1e are defined as shown in Figure 6.1(a), 6.1(b) and Table 6.1.

The QCD multi-jet and γ+jets events in SR1e contain a high-p_{T} fake electron and high-p_{T} large-R jet produced back-to-back in x-y plane, and there is no additional jet in the event. For this event topology, the leading order di-jet and γ+jets MC samples are relatively reliable except for the prediction of their cross-sections. So, not only for W+jets but also for QCD multi-jet and γ+jets, their contributions in SR1e are estimated by the semi-data driven method using MC samples to predict their normalization factors.

The W+jets normalization factor is mainly determined in CRW1e which has low-$\cos\theta$ region $[0.0, 0.7]$. As shown in Figure 5.5(c), W+jets occupancy is quite high in that region. Given the lower $\cos\theta$, the momentum of the electron and neutrino from W-boson decay is relatively balanced.

Table 6.1: Definitions of signal and control regions for one electron channel. The selection cuts to define CRs are shown with the underlines with respect to SR1e. The other cuts are the same as SR1e. The last column shows a variable for binning and the number of bins.

Variable	SR1e	CRLow1e	CRW1e	CRFake1e	CRγ1e
Electron isolation	`FCHighPtCaloOnly`	`FCHighPtCaloOnly`	`FCHighPtCaloOnly`	$\underline{\texttt{FCLoose}\text{ and not }\texttt{FCHighPtCaloOnly}}$	`FCHighPtCaloOnly`
$\cos\theta$	> 0.7	> 0.7	$\underline{[0.0, 0.7]}$	> 0.7	> 0.7
`Ambiguity`	N/A	$\underline{== -1}$	N/A	N/A	$\underline{> -1}$
W_{R} mass in TeV	> 3.0	$\underline{[1.0, 2.0]}$	$\underline{[1.0, 2.0]}$	$\underline{[1.0, 2.0]}$	$\underline{[1.0, 2.0]}$
Number of bins	2 in W_{R} mass	1	1	1	1

The QCD multi-jet contribution is mainly estimated in CRFake1e which requires the inverted electron isolation criteria. A prompt electron from the W/Z decay is well isolated. However a fake electron in the QCD multi-jet events deposits its energy in wider calorimeter regions as shown in Figure 6.2(a). Thus, the QCD multi-jet occupancy in CRFake1e is pretty high. On the other hand, most of the fake electrons in γ+jets events are electrons from the photon conversion. Thus, they satisfy the `FCHighPtCaloOnly` isolation condition.

There are different properties in the associated tracks between a electron derived from the photon conversion and a prompt electron. Utilizing them, CRγ1e is introduced to estimate γ+jets events. As shown in Figure 6.2(b), the purity of γ+jets is high in the bin with `Ambiguity` = 2. On the other hand, almost no γ+jets remain in the bin with `Ambiguity` = -1. CRγ1e is defined to have `Ambiguity` != -1.

CRLow1e is introduced to give an additional constraint to the normalization factors and to reflect the features of the most proximate regions with SR1e. CRLow1e is the exactly same phase space with CRγ1e except the requirement of electron `Ambiguity` == -1. This helps to disentangle γ+jets from W+jets and makes it easy to estimate them independently.

Finally the obtained normalization factors are transferred to the high-$m(W_{\mathrm{R}})$ regions assuming the MC simulation of $m(W_{\mathrm{R}})$ distribution is well modeled. To confirm it, a standard VR, VR1e, with intermediate mass interval between SR1e and CRLow1e is defined. Also, VRW1e and VRFake1e are defined for verification of transfers of W+jets and QCD multi-jet normalization factor to low- to high-mass regions with high purity regions, respectively. The definitions of them are summarized in Table 6.2.

Table 6.2: Definitions of standard validation regions for one electron channel. The selection cuts to define VRs are shown with the underlines with respect to SR1e. The other cuts are the same as SR1e. The last column shows a variable for binning and the number of bins.

Variable	VR1e	VRW1e	VRFake1e
Electron isolation	`FCHighPtCaloOnly`	`FCHighPtCaloOnly`	$\underline{\texttt{FCLoose}\text{ and not }\texttt{FCHighPtCaloOnly}}$
$\cos\theta$	> 0.7	$\underline{[0.0, 0.7]}$	> 0.7
W_{R} mass in TeV	$\underline{(2.0, 3.0]}$	$\underline{> 2.0}$	$\underline{> 2.0}$
Number of bins	1	2 in W_{R} mass	2 in W_{R} mass

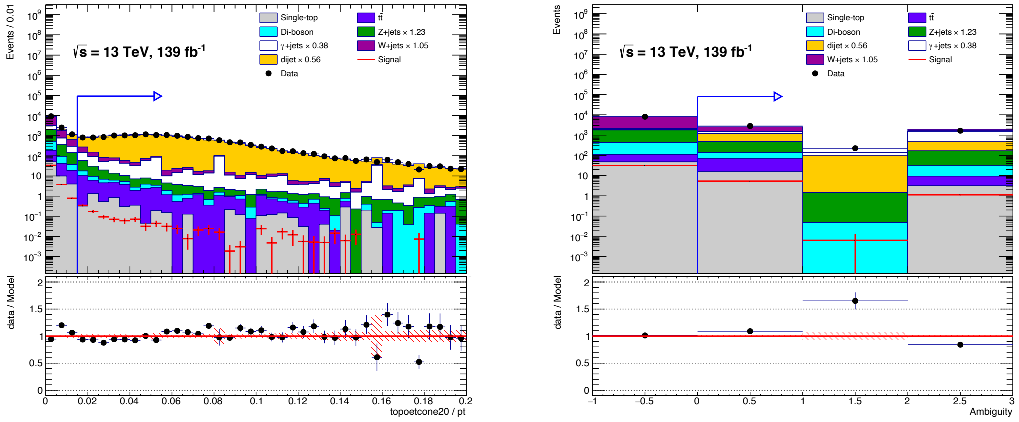

(a) Energy spreadness of the electron

(b) `Ambiguity` of the electron

Figure 6.2: Pre-fit distributions of variables to define CRFake1e and CRγ1e. (a) shows the distribution of the spreadness of energy deposition from the electron. (b) shows the `Ambiguity` of the electron. Blue vertical lines and horizontal arrows in (a) and (b) indicate the value and direction of CRFake1e and CRγ1e, respectively. The number of W+jets, QCD multi-jet, γ+jets and Z+jets yields are normalized with normalization factors which are obtained by dedicated CRs. The ratio of data over MC and statistical uncertainties are displayed as black points and red histograms in the bottom panels, respectively.

6.1.1 Validation of W+jets estimation with extra VRs

To check the W+jets estimation along the $\cos\theta$ and W_{R} mass distributions, extra VRs (VRW$_{\mathrm{SR1e}}$, VRW$_{\mathrm{CRLow1e}}$ and VRW$_{\mathrm{CRW1e}}$) are defined as summarized in Table 6.3. They require the electron $p_{\mathrm{T}} < 200$ GeV and $E_{\mathrm{T}}^{\mathrm{miss}} > 200$ GeV (c.f. $p_{\mathrm{T}} > 200$ GeV and $E_{\mathrm{T}}^{\mathrm{miss}} < 200$ GeV in SR1e). Since the $\cos\theta$ calculation assumes the $W \rightarrow e\nu$ process and $E_{\mathrm{T}}^{\mathrm{miss}}$ derived only from the neutrino, $\cos\theta$ is biased towards negative values in these regions as shown in Figure 6.3(a). The p_{T} requirement for electrons in the object selection ($p_{\mathrm{T}} > 25$ GeV) reduces events with $\cos\theta \simeq -1$. For VRW$_{\mathrm{SR1e}}$ and VRW$_{\mathrm{CRLow1e}}$, $-1 \leq \cos\theta < -0.7$ is required, while $-0.7 \leq \cos\theta < 0.0$ for VRW$_{\mathrm{CRW1e}}$. The invariant mass of a neutrino and a large-R jet, $m_{\nu,J}$, is used for low- to high-mass extrapolation instead of the mass of an electron and a large-R jet system. To increase the data statistics, the mass threshold between VRW$_{\mathrm{CRLow1e}}$ and VRW$_{\mathrm{SR1e}}$ is set at 2 TeV. The contributions of QCD multi-jet and γ+jets are negligible in these regions due to the large-$E_{\mathrm{T}}^{\mathrm{miss}}$ requirement. The purity of W+jets in VRW$_{\mathrm{SR1e}}$ is greater than 90%. The fit to these extra VRs are performed just to confirm the W+jets estimation strategy works well, and they are not involved in the actual CRs + SRs fits.

6.1.2 Validation of QCD multi-jet estimation with extra VRs

To check the QCD multi-jet estimation strategy assuming the simulated lepton isolation efficiency for the fake electrons agrees with the data, extra VRs are defined: VRFake$_{\mathrm{SR1e}}$, VRFake$_{\mathrm{CRLow1e}}$ and VRFake$_{\mathrm{CRFake1e}}$, as summarized in Table 6.4. The electron is required to satisfy the `LHMedium` identification but failing the `LHTight` to ensure an orthogonality with SR1e. To increase the data statistics, the mass threshold between VRFake$_{\mathrm{CRFake1e}}$ and VRFake$_{\mathrm{SR1e}}$ is set at 2 TeV. As shown in Figure 6.3(b), the contributions of

Table 6.3: Definitions of extra validation regions for the W+jets estimation. The other cuts are the same as SR1e. The last column indicates the number bins and variable for binning.

Variable	$\mathrm{VRW}_{\mathrm{SR1e}}$	$\mathrm{VRW}_{\mathrm{CRLow1e}}$	$\mathrm{VRW}_{\mathrm{CRW1e}}$	SR1e
Electron p_{T} in GeV	< 200	< 200	< 200	> 200
$E_{\mathrm{T}}^{\mathrm{miss}}$ in GeV	> 200	> 200	> 200	< 200
$\cos\theta$	< -0.7	< -0.7	$[-0.7, 0.0)$	> 0.7
W_{R} mass in TeV	> 2.0	$[1.0, 2.0]$	$[1.0, 2.0]$	> 3.0
Number of bins	2 in $m_{\nu,J}$ mass	1	1	2 in W_{R} mass

W+jets and γ+jets are negligible in these regions due to the inverted electron identification. The purity of QCD multi-jet is about 92 % in $\mathrm{VRFake}_{\mathrm{SR1e}}$. The fit to these extra VRs are performed just to confirm the estimation strategy works well, and they are not involved in the actual CRs + SRs fits.

Table 6.4: Definitions of extra validation regions for QCD multi-jet estimation. The other cuts are the same as SR1e. The last column indicates the number of bins and variable for binning.

Variable	$\mathrm{VRFake}_{\mathrm{SR1e}}$	$\mathrm{VRFake}_{\mathrm{CRLow1e}}$	$\mathrm{VRFake}_{\mathrm{CRFake1e}}$	SR1e
Electron identification	`Medium` and not `Tight`	`Medium` and not `Tight`	`Medium` and not `Tight`	`Tight`
Electron isolation	`FCHighPtCaloOnly`	`FCHighPtCaloOnly`	`FCLoose` and not `FCHighPtCaloOnly`	`FCHighPtCaloOnly`
W_{R} mass in TeV	> 2.0	$[1.0, 2.0]$	$[1.0, 2.0]$	> 3.0
Number of bins	2 in W_{R} mass	1	1	2 in W_{R} mass

6.1.3 Validation of γ+jets estimation with extra VRs

While the γ+jets normalization factor is well determined in CRγ1e, the distribution of W_{R} mass relays on MC simulation, thus the following points need to be verified. The fits to following extra VRs are performed just to confirm the γ+jets estimation strategy works fine, and they are not involved in the actual CRs + SRs fits.

6.1.3.1 Data to MC agreement in high-W_{R} mass

To validate the reliability of the γ+jets MC event shapes, following extra VRs with a photon instead of an electron are defined: SR1ph, VR1ph, CRLow1ph and CRFake1ph as summarized in Table 6.5. W+jets occupancy is negligibly small in every regions because it requires the number of electron exactly zero. Therefore any regions to control W+jets are not needed. The γ+jets accounts for about 54 % in SR1ph. The sub-dominant background process is QCD multi-jet which is normalized in CRFake1ph.

6.1.3.2 Photon to electron fake factor

In case the photon-to-electron fake factor depending on a photon p_{T} and η in simulation does not agree with data, it gives mis-modeling of W_{R} mass distribution in SR1e, even if the $m_{\gamma,J}$ modeling of the γ+jets

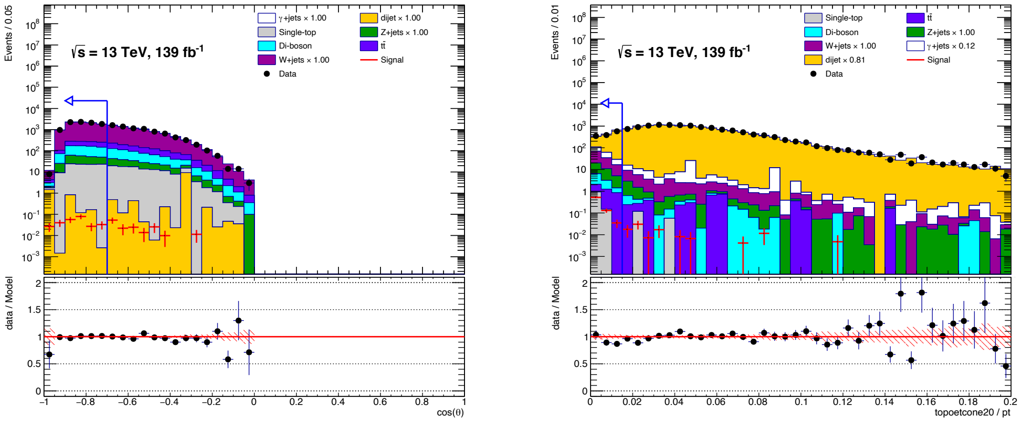

(a) cos θ

(b) Energy spreadness of the electron

Figure 6.3: Pre-fit distributions of variables to define $\mathrm{VRW}_{\mathrm{CRLow1e}}$ and $\mathrm{VRFake}_{\mathrm{CRLow1e}}$. (a) shows the distribution of the electron decay angle computed by assuming the standard model W boson decay. As show in Table 4.4, since the electron requires p_{T} greater than 25 GeV, the number of events with cos $\theta \simeq -1$ is small. (b) shows the distribution of the spreadness of energy deposition from the electron. Blue vertical lines and horizontal arrows in (a) and (b) indicate the value and direction of $\mathrm{VRW}_{\mathrm{CRLow1e}}$ and $\mathrm{VRFake}_{\mathrm{CRLow1e}}$, respectively. The number of W+jets and QCD multi-jet yields are normalized. These normalization factors are obtained by dedicated CRs. Red hashed histograms shown in the bottom panels correspond only statistical uncertainties.

Table 6.5: Definitions of extra validating regions for γ+jets estimation. Other cuts are the same as SR1e. The last column indicates the number of bins and variable for binning.

Variable	SR1ph	VR1ph	CRLow1ph	CRFake1ph	SR1e
Number of (e, γ)	(0, 1)	(0, 1)	(0, 1)	(0, 1)	(1, N/A)
Photon isolation	`FCTightCaloOnly`	`FCTightCaloOnly`	`FCTightCaloOnly`	`FCLoose` and not `FCTightCaloOnly`	`FCHighPtCaloOnly`
W_{R} mass in TeV	> 3.0	(2.0, 3.0]	[1.0, 2.0]	[1.0, 2.0]	> 3.0
Number of bins	2 in $m_{\gamma,J}$ mass	1	1	1	2 in W_{R} mass

MC is good. To confirm the photon-to-electron fake factor is well modeled and does not affect the W_{R} reconstruction, following two set of extra VRs are employed.

- Check the MC to data agreement in regions with optimized cos θ and isolation cuts to enhance γ+jets events with $\Delta\eta$ to be from 2.0 to 3.0 for ensuring an orthogonality with actual SR/CR. $\mathrm{VR}\gamma_{\mathrm{SR1e}}$, $\mathrm{VR}\gamma_{\mathrm{CRLow1e}}$, $\mathrm{VR}\gamma_{\mathrm{CRW1e}}$ and $\mathrm{VR}\gamma_{\mathrm{CRFake1e}}$ are defined as summarized in Table 6.6. The occupancy of γ+jets in $\mathrm{VR}\gamma_{\mathrm{SR1e}}$ is about 42 % and it is the dominant background process.
- Check the MC to data agreement in the exactly same regions with above optimized phase spaces except a requirement of a photon instead of an electron. $\mathrm{VR}\gamma_{\mathrm{SR1ph}}$, $\mathrm{VR}\gamma_{\mathrm{CRFake1ph}}$ and $\mathrm{VR}\gamma_{\mathrm{CRFake1ph}}$ are defined as summarized in Table 6.7. W+jets occupancy is negligibly small in every regions because it require the number of electron exactly zero. Therefore there is no region to control W+jets yields. The occupancy of γ+jets in $\mathrm{VR}\gamma_{\mathrm{SR1ph}}$ is about 63 % and it is enough to check the estimation strategy.

In case of similar MC to data agreements even in high-W_{R} mass regions are observed, it can be concluded that photon to electron fake factor is well modeled by MC.

Table 6.6: Definitions of extra validation regions for the γ+jets estimation. Other cuts are the same as SR1e. The last column indicates the number of bins and variable for binning.

Variable	$\mathrm{VR}\gamma_{\mathrm{SR1e}}$	$\mathrm{VR}\gamma_{\mathrm{CRLow1e}}$	$\mathrm{VR}\gamma_{\mathrm{CRW1e}}$	$\mathrm{VR}\gamma_{\mathrm{CRFake1e}}$	SR1e
$\Delta\eta_{el,J}$	[2.0, 3.0]	[2.0, 3.0]	[2.0, 3.0]	[2.0, 3.0]	< 2.0
Electron isolation	`FCHighPtCaloOnly`	`FCHighPtCaloOnly`	`FCHighPtCaloOnly`	`FCLoose` and not `FCHighPtCaloOnly`	`FCHighPtCaloOnly`
$\cos\theta$	> 0.7	> 0.7	[0.0, 0.7]	> 0.7	> 0.7
W_{R} mass in TeV	> 2.0	[1.0, 2.0]	[1.0, 2.0]	[1.0, 2.0]	> 3.0
Number of bins	2 in $m_{\gamma,J}$ mass	1	1	1	2 in W_{R} mass

Table 6.7: Definitions of extra validation regions for the γ+jets estimation. Other cuts are the same as SR1e. The last column indicates the number of bins and variable for binning.

Variable	$\mathrm{VR}\gamma_{\mathrm{SR1ph}}$	$\mathrm{VR}\gamma_{\mathrm{CRLow1ph}}$	$\mathrm{VR}\gamma_{\mathrm{CRFake1ph}}$	SR1e
Number of (e, γ)	(0, 1)	(0, 1)	(0, 1)	(1, N/A)
Photon isolation	`FCTightCaloOnnly`	`FCTightCaloOnly`	`FCLoose` and not `FCTightCaloOnly`	FCHighPtCaloOnly
W_{R} mass in TeV	> 2.0	[1.0, 2.0]	[1.0, 2.0]	> 3.0
Number of bins	2 in W_{R} mass	1	1	2 in W_{R} mass

6.2 Background estimation method for SR2e

The dominant SM background in SR2e is $Z(\rightarrow ee)$+jets (85%). The normalization factor for Z+jets is treated as a free parameter and obtained from the data in CRLow2e. The other backgrounds are estimated by the MC simulation. To check the extrapolation from low- to high-W_{R} mass region, a standard VR named VR2e between CRLow2e and SR2e, is prepared. The estimated normalization factor for Z+jets in CRLow2e is also used in SR1e and VR1e, since p_{T} regimes of truth Z boson for them are similar. The extra VRs, namely $\mathrm{VRZ}_{\mathrm{SR2e}}$ and $\mathrm{VRZ}_{\mathrm{CRLow2e}}$, are prepared by requiring di-electron mass 120 GeV $< m_{e1,e2} <$ 200 GeV to verify the extrapolation from low- to high-W_{R} mass with little signal contamination. The purity of Z+jets in $\mathrm{VRZ}_{\mathrm{SR2e}}$ is about 98 % as shown in Figure 5.6(a). The studies in these extra VRs are found in Section 8.4. The definitions of all regions related to two electron channels are summarized in Table 6.8.

Table 6.8: Definitions of regions for the two electron channel. The selection cuts to define CR/VRs are shown with the underlines with respect to SR2e. The last column indicates the number of bins and variable for binning.

Variable	SR2e	VR2e	CRLow2e	$\mathrm{VRZ}_{\mathrm{SR2e}}$	$\mathrm{VRZ}_{\mathrm{CRLow2e}}$
Di-electron mass in GeV	> 200	> 200	> 200	$\underline{[120, 200]}$	$\underline{[120, 200]}$
W_{R} mass in TeV	> 3.0	$\underline{(2.0, 3.0]}$	$\underline{[1.0, 2.0]}$	$\underline{> 2.0}$	$\underline{[1.0, 2.0]}$
Number of bins	2 in W_{R} mass	1	1	2 in W_{R} mass	1

6.3 Background estimation method for SR2mu

The dominant SM background in SR2mu is $Z(\rightarrow \mu\mu)$+jets (80%). The normalization factor for Z+jets is treated as a free parameter and obtained from the data in CRLow2mu. The other backgrounds are estimated by the MC simulation. To check the extrapolation from low- to high-W_{R} mass region, a standard VR named VR2mu between CRLow2mu and SR2mu, is prepared. The extra VRs, namely VRZ$_{\mathrm{SR2mu}}$ and VRZ$_{\mathrm{CRLow2mu}}$, are prepared to verify the extrapolation from low- to high-W_{R} mass with little signal contamination as shown in Figure 5.8(a). The studies in these extra VRs are found in Section 8.4. The definitions of all regions related to two muon channels are summarized in Table 6.9.

Table 6.9: Definitions of regions for two muon channel. The selection cuts to define CR/VRs are shown with the underlines with respect to SR2mu. The last column indicates the number of bins variable for binning.

Variable	SR2mu	VR2mu	CRLow2mu	VRZ$_{\mathrm{SR2mu}}$	VRZ$_{\mathrm{CRLow2mu}}$
Di-muon mass in GeV	> 200	> 200	> 200	$\underline{[120, 200]}$	$\underline{[120, 200]}$
W_{R} mass in TeV	> 3.0	$\underline{(2.0, 3.0]}$	$\underline{[1.0, 2.0]}$	$\underline{>2.0}$	$\underline{[1.0, 2.0]}$
Number of bins	2 in W_{R} mass	1	1	2 in W_{R} mass	1

6.4 Summary of background estimation method

The fractions of the background components in CRs and standard VRs and SRs are visualized in Figure 6.4 and 6.5.

In this section, various fit configurations described above are summarized. Two different “main” fits are performed to search for signals in electron channel and muon channel. In addition, seven independent fits with extra VRs are performed to verify estimation strategies. They are put together in Table 6.10.

In the SR+CR fit for the electron channel, the floating normalization factors for W+jets, QCD multi-jet and γ+jets are applied to only regions with the suffix ”1e”. The Z+jets normalization is floated in both regions with the suffix “1e” and “2e”, and treated as fully correlated between them. In the muon channel, only the Z+jets normalization is treated as free. The separate fits to electron and muon channels are performed, and they are not combined for the final result. For most extra VR studies, thanks to high purity, it is enough to float the target background process and give a fixed cross-section uncertainty, i.e. only W+jets is floated in W+jets extra VRs.

The normalization factors to be considered in each fit are put together in Table 6.11.

Table 6.10: Summary of the background estimation strategies. There are 9 different fit configurations. Two of them are performed to derive final results. The other fits are performed independently to validate the strategies.

Fit configuration	Normalization factors obtained in	Normalization factors applied to	Fit result in
Electron SR+CR fit	CRLow1e, CRW1e, CRFake1e and CRLow2e	SR1e, VR1e, SR2e and VR2e	Section 9.1.1
Extra VRs for W+jets	VRW$_{\text{CRLow1e}}$ and VRW$_{\text{CRW1e}}$	VRW$_{\text{SR1e}}$	Section 8.1
Extra VRs for QCD multi-jet	VRFake$_{\text{CRLow1e}}$ and VRFake$_{\text{CRFake1e}}$	VRFake$_{\text{SR1e}}$	Section 8.2
Extra VRs for γ+jets	CRLow1ph and CRFake1ph VRγ_{CRLow1e}, VRγ_{CRW1e} and VRγ_{CRFake1e} VRγ_{CRLow1ph} and VR$\gamma_{\text{CRFake1ph}}$	SR1ph and VR1ph VRγ_{SR1e} VRγ_{SR1ph}	Section 8.3.1 Section 8.3.2 Section 8.3.2
Extra VRs for $Z(\rightarrow ee)$+jets	VRZ$_{\text{CRLow2e}}$	VRZ$_{\text{SR2e}}$	Section 8.4.1
Muon SR+CR fit	CRLow2mu	SR2mu and VR2mu	Section 9.1.2
Extra VRs for $Z(\rightarrow \mu\mu)$+jets	VRZ$_{\text{CRLow2mu}}$	VRZ$_{\text{SR2mu}}$	Section 8.4.2

Table 6.11: The normalization factors considered in each fit, and the regions for which the given normalization factor is applied.

Fit configuration	Normalization factor	To be applied to
Electron SR+CR fit	W+jets QCD multi-jet γ+jets Z+jets	CRLow1e, CRW1e, VRW1e, CRFake1e, VR1e and SR1e CRLow1e, CRW1e, CRFake1e, VRFake1e, VR1e and SR1e CRLow1e, CRW1e, CRFake1e, VR1e and SR1e CRLow1e, CRW1e, CRFake1e, VR1e, SR1e, CRLow2e and SR2e
Extra VRs for W+jets	W+jets	VRW$_{\text{CRLow1e}}$, VRW$_{\text{CRW1e}}$ and VRW$_{\text{SR1e}}$
Extra VRs for QCD multi-jet	QCD multi-jet	VRFake$_{\text{CRLow1e}}$, VRFake$_{\text{CRFake1e}}$ and VRFake$_{\text{SR1e}}$
Extra VRs for γ+jets	γ+jets QCD multi-jet	CRLow1ph, CRFake1ph and SR1ph
	γ+jets QCD multi-jet W+jets	VRγ_{CRLow1e}, VRγ_{CRW1e}, VRγ_{CRFake1e} and VRγ_{SR1e}
	γ+jets QCD multi-jet	VR$\gamma_{\text{CRFake1ph}}$, VR$\gamma_{\text{CRFake1ph}}$ and VRγ_{SR1ph}
Extra VRs for $Z(\rightarrow ee)$+jets	Z+jets	VRZ$_{\text{CRLow2e}}$ and VRZ$_{\text{SR2e}}$
Muon SR+CR fit	Z+jets	CRLow2mu, VR2mu and SR2mu
Extra VRs for $Z(\rightarrow \mu\mu)$+jets	Z+jets	VRZ$_{\text{CRLow2mu}}$ and VRZ$_{\text{SR2mu}}$

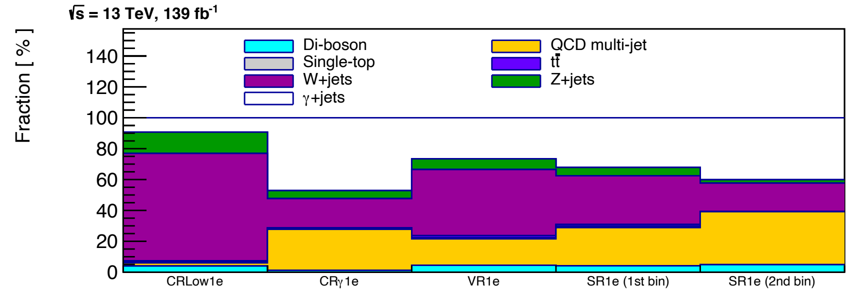

(a) CRLow1e, CRγ1e, VR1e, SR1e

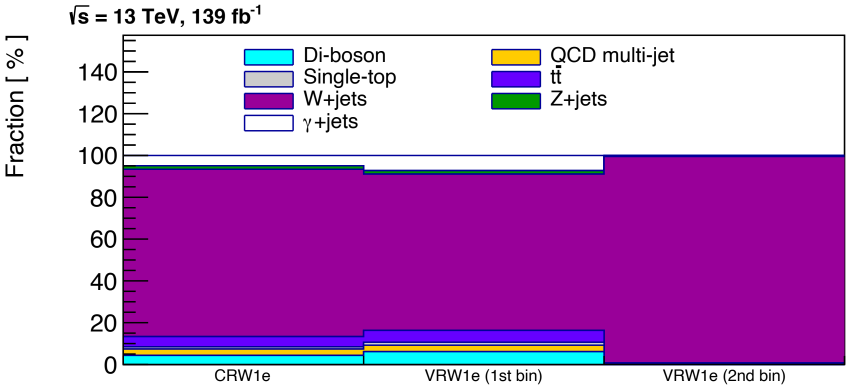

(b) CRW1e, VRW1e

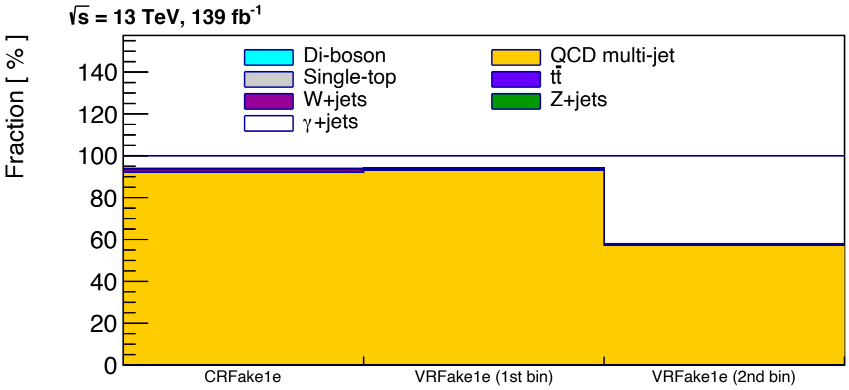

(c) CRFake1e, VRFake1e

Figure 6.4: Breakdown of the pre-fit SM components in each region for one electron channel.

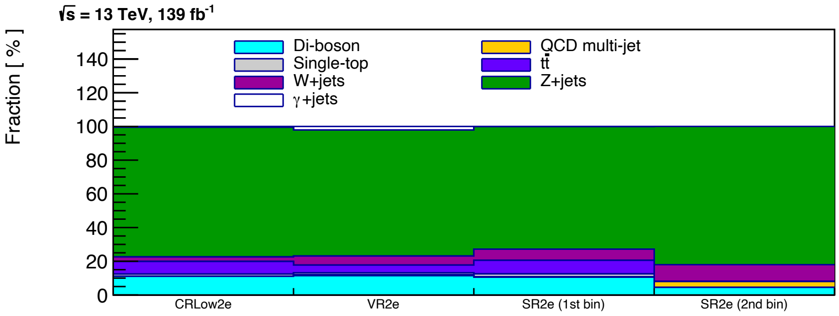

(a) CRLow2e, VR2e, SR2e

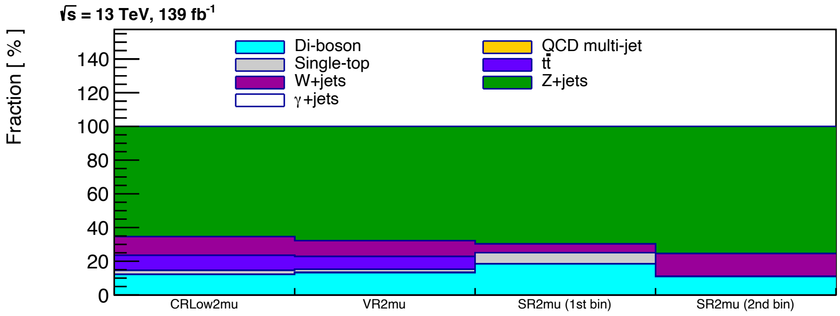

(b) CRLow2mu, VR2mu, SR2mu

Figure 6.5: Breakdown of the pre-fit SM components in each region for two lepton channels.

7 Statistical analysis

The profile Log Likelihood Ratio (LLR) approach is used to estimate the number of background in SRs (background only fit), determine an upper bound on BSM events (model-independent fit) and exclude a certain signal hypothesis (model-dependent fit) [107]. In the fitting procedure, the maximization of a LLR is executed taking into account the effects of systematic uncertainties. The purpose of each fitting configuration is described below.

Background only fit

The purpose is to estimate the backgrounds in SRs and VRs without any signal assumptions. Only CRs are used to constrain the normalization and nuisance parameters. Any potential signal contamination is assumed to be neglected in all regions. Results can be found in Section 9.1.

Model-independent fit

The purpose is to set model-independent limits on the number of BSM events in a certain SR. Both CRs and a SR are used in the fit. The signal contribution is considered only in the SR. Results can be found in Section 9.2.

Model-dependent fit

The purpose is to set limits on a specific model of BSM physics. Both CRs and SRs are used in the fit. The potential signal contribution is also taken into account in all regions. Results can be found in Section 9.3.

7.1 Likelihood function

A likelihood function is defined by Poisson terms which describe the statistical fluctuations of data convoluted with Gaussian terms which describe systematic uncertainties:

$$L(\boldsymbol{n}|\boldsymbol{\mu}, \boldsymbol{s}, \boldsymbol{b}, \boldsymbol{\theta}) = \prod_{i\, \in\, \{\text{Regions}\}} P_i \times \prod_{j\, \in\, \{\text{Systematic sources}\}} G(\theta_j),$$

where P_i is a poisson probability distribution for a certain region i. $G(\theta_j)$ is a gaussian probability distribution of a certain systematic uncertainty j. Each systematic uncertainty θ_j is usually given in units of the standard deviation. Each poisson probability density distribution P_i can be decomposed with the number of observed events n_i and the expected number of events λ_i:

$$P_i = P(n_i|\lambda_i) = \frac{\lambda_i^{n_i}}{n_i!} e^{-\lambda_i},$$

where λ_i is given by:

$$\lambda_i(\boldsymbol{\mu}, s_i, \boldsymbol{b}, \boldsymbol{\theta}) = s_i(\boldsymbol{\theta}) \cdot \mu_s + \sum_{k\, \in\, \{\text{Background with NF}\}} b_{i,k}(\boldsymbol{\theta}) \cdot \mu_k + \sum_{l\, \in\, \{\text{Background without NF}\}} b_{i,l}(\boldsymbol{\theta}),$$

and each parameter is defined below.

- i corresponds to a region (SR1e, CRW1e, CRFake1e etc.) and bin number (first and second bin in SR1e etc.).
- k corresponds to a background component with a normalization factor μ_k (W+jets, QCD multi-jet, γ+jets, Z+jets for electron CRs/SRs fit).
- l corresponds to a background component without a normalization factor ($t\bar{t}$, diboson, single top).
- s_i corresponds to the number of signal in region i.
- $b_{i,k}$ and $b_{i,l}$ correspond to the number of background k and l in region i, respectively.
- μ_s corresponds to a normalization factor for signal, which is called a signal strength.
- μ_k corresponds to a normalization factor for background k.
- $\boldsymbol{\theta}$ corresponds to a set of the nuisance parameters which describe the systematic uncertainties.

The mean of standard deviation of all probability density distribution is set to 0 and $\theta = \pm 1$ corresponds to $\pm 1\sigma$ variation. Since $\boldsymbol{s}$ and $\boldsymbol{b}$ depend only on a set of systematic uncertainty $\boldsymbol{\theta}$, the likelihood function can be denoted as $L(\mu, \boldsymbol{\theta})$.

In actual fitting procedure, for easy calculation, the logarithm of the likelihood is used. μ and $\boldsymbol{\theta}$ are treated as parameters of LLR, and a set of parameters that maximizes LLR is considered as post-fit values. If the numbers of background and signal do not depend strongly on a certain systematic source ($\lambda_i|_{\theta_n=0} \sim \lambda_i|_{\theta_n=\pm 1}$), 1σ variation of each systematic uncertainty can be interpreted as $1/2$ variation of the log likelihood function.

$$\begin{aligned}
LLR &= \Delta \log L(\mu, \boldsymbol{\theta}) = \log \frac{L(\mu, \boldsymbol{\theta})|_{\theta_n=0}}{L(\mu, \boldsymbol{\theta})|_{\theta_n=\pm 1}} \\
&= \log L(\mu, \boldsymbol{\theta})|_{\theta_n=0} - \log L(\mu, \boldsymbol{\theta})|_{\theta_n=\pm 1} \\
&= \sum_{i \,\in\, \{\text{Regions}\}} \log P_i|_{\theta_n=0} - \sum_{i \,\in\, \{\text{Regions}\}} \log P_i|_{\theta_n=\pm 1} \\
&\quad + \sum_{j \,\in\, \{\text{Systematic sources}\}} \log G_j\big|_{\theta_n=0} - \sum_{j \,\in\, \{\text{Systematic sources}\}} \log G_j\big|_{\theta_n=\pm 1} \\
&= \sum_i \left(n_i \log \frac{\lambda_i|_{\theta_n=0}}{\lambda_i|_{\theta_n=\pm 1}} - \lambda_i|_{\theta_i=0} + \lambda_i|_{\theta_i=\pm 1} \right) - \frac{1}{2} \\
&= \sum_i \left\{ n_i \log \left(\frac{n_i}{n_i \pm m_i} \right) - n_i + n_i \pm m_i \right\} - \frac{1}{2} \\
&= \sum_i \left\{ n_i \sum_{k=1}^{\infty} \frac{(-1)^{k+1}}{k} \left(\frac{\mp m_i}{n_i \pm m_i} \right)^k \pm m_i \right\} - \frac{1}{2} \\
&\sim \sum_i \left\{ \mp n_i \left(\frac{m_i}{n_i \pm m_i} \right) \pm m_i \right\} - \frac{1}{2} \\
&\sim -\frac{1}{2}
\end{aligned}$$

where m_i represents the variation of yield with respect to the systematic source θ_i. Maclaurinś expansion was used to remove a logarithmic function.

The post-fit error of each nuisance parameter is implemented by varying the log likelihood by $1/2$.

7.2 Hypothesis test

The profile likelihood ratio [108] is defined as:

$$LLR(\mu_s) = \frac{L(\boldsymbol{n}|\mu_s, \hat{\hat{\boldsymbol{\theta}}})}{L(\boldsymbol{n}|\hat{\mu_s}, \hat{\boldsymbol{\theta}})}$$

where $L(\boldsymbol{n}|\hat{\mu_s}, \hat{\boldsymbol{\theta}})$ is the maximum likelihood obtained by varying both μ_s and $\boldsymbol{\theta}$ (unconditional fit), $\hat{\theta}$ and $\hat{\mu_s}$ return the maximum likelihood, and $L(n|\mu_s, \hat{\hat{\boldsymbol{\theta}}})$ is the maximum likelihood obtained by floating $\boldsymbol{\theta}$ with a fixed μ_s (conditional fit), $\hat{\hat{\boldsymbol{\theta}}}$ corresponds to $\boldsymbol{\theta}$ returns the maximum likelihood for a given μ_s. In the latter case, the value of $\boldsymbol{\theta}$ depends on the value of μ_s. $LLR(\mu_s)$ is less than or equal to 1. A test statistics q_{μ_s} [108] is defined as:

$$q_{\mu_s} = -2\log LLR(\mu_s)$$

Signal-like data has more likely to exhibit a low test-statistic (q_{μ_s} close to 0) and background-like data has a large q_{μ_s} for $\mu_s = 1$. On the other hand, for $\mu_s = 0$, signal-like data has a large q_{μ_s} and the background-like data has a small q_{μ_s}.

The p-value p_{μ_s} for a given μ_s is calculated as the cumulative probability of q_{μ_s} above the observed test statistics $q_{\mu_s}^{\mathrm{obs}}$ as follows:

$$p_{\mu_s} = P(q_{\mu_s} > q_{\mu_s}^{\mathrm{obs}}|\mu_s') = \int_{q_{\mu_s}^{\mathrm{obs}}}^{\infty} f(q_{\mu_s}|\mu_s')dq_{\mu_s}$$

where $f(q_{\mu_s}|\mu_s')$ is a probability density function (PDF) of μ_s under the assumption of the signal strength μ_s'. In this analysis, the approximation method defined in Ref. [108] is used instead of the toy Monte Carlo to obtain the PDF. The p-value with the signal plus background hypothesis is called p_{s+b} and the p-value with the background only hypothesis is quoted as $1 - p_b$ as follows:

$$\begin{aligned} p_{s+b} &= P(q_{\mu_s} > q_{\mu_s}^{\mathrm{obs}}|\mu_s = 1) = \int_{q_{\mu_s}^{\mathrm{obs}}}^{\infty} f(q_{\mu_s}|\mu_s = 1)dq_{\mu_s}, &(7.1)\\ 1 - p_b &= P(q_{\mu_s} > q_{\mu_s}^{\mathrm{obs}}|\mu_s = 0) = \int_{q_{\mu_s}^{\mathrm{obs}}}^{\infty} f(q_{\mu_s}|\mu_s = 0)dq_{\mu_s}. &(7.2)\end{aligned}$$

where both parameters depends on the value of μ_s for the test statistics. CL_{s+b} is defined as the case of $q_{\mu_s} = q_1$ in equation 7.1 and CL_b and p_0 are defined as the case of $q_{\mu_s} = q_0$ in equation 7.2. In case of the $p_0 > 0.5$, 0.5 is assigned to p_0 instead. CL_s is defined as

$$CL_s = \frac{CL_{s+b}}{CL_b}.$$

The exclusion of a signal hypothesis at the 95% confidence level is defined to be CL_s less than 0.05 [109]. By dividing CL_{s+b} by CL_b, the integrity of background estimations can also be taken into account in the signal hypothesis tests.

7.3 Systematic uncertainties

There are three types of systematic uncertainties for event yields expectations: ”experimental uncertainty”, ”theoretical uncertainty” and ”ad-hoc uncertainty”. The details of all the uncertainties are explained in the following. Correlations between the different regions and bins are taken into account, and they can vary the shape of the variables used to define the regions, such as W_{R} mass and $\cos\theta$.

7.3.1 Experimental uncertainty

The experimental uncertainties associated with the reconstruction and calibration of each object are discussed in this section. The variations of the event yields in all regions are included and correlated. They are treated as nuisance parameters as described in Section 7.1.

Jets

As discussed in Section 4.4, the jets used in this analysis are calibrated for energy scale, energy resolution and mass scale. More than 100 independent systematic sources are considered [94]. However, they are grouped up to skim the size of uncertainties. Compared to other experimental uncertainties, the high p_{T} jets have large variation and can have a significant impact on the evaluation of signal sensitivities.

Leptons

The uncertainties for the electron and muon calibrations are included. Not only the variations of scale and resolution of the lepton momentum but also variations of the identification and isolation efficiencies are taken into account [99, 100]. The size of these uncertainties are generally smaller than the jet uncertainties.

Flavour tagging

As discussed in Section 4.5, the flavor tagging depends on many variables and is calibrated. The uncertainties on the calibration of the efficiencies for $b-$, $c-$ and light-flavor are included [110]. In particular, these uncertainties are large for signal samples with heavy N_{R} since one-third of the events have a top quark and a bottom quark in the final states originated from $N_{\mathrm{R}} \to \ell^{\pm} W_{\mathrm{R}}^{*} \to \ell^{\pm} q q'$ decay process.

Luminosity

The size of uncertainty on luminosity is obtained by using the LUCID-2 introduced in Section 2.2.1. The uncertainty of the combined 2015 – 2018 integrated luminosity is 1.7% [53].

Pile-up reweighting

As discussed in Section 3.3, the uncertainty on the pile-up re-weighting is included. Up- and down-type variations are given by applying (1/0.99) and (1/1.07) as a scale factor, respectively [68]. This uncertainty does not give a big impact on signal sensitivities.

$E_{\mathrm{T}}^{\mathrm{miss}}$ soft term

As discussed in Section 4.10, the calibration to scale and resolution is performed for the soft term that is one of the components of $E_{\mathrm{T}}^{\mathrm{miss}}$. The uncertainty sources derived from them are included [105].

Monte Carlo sample statistics

Since MC is used to estimate background events, the statistical uncertainties of the simulated events also affect the signal sensitivity. Especially in regions where tight cuts are applied, such as signal regions, they can have significant impacts.

7.3.2 Theoretical uncertainty

For major background components, theoretical uncertainties are assigned for the shape variations of $m(W_\mathrm{R})$, $\cos\theta$ distributions as well as the electron isolation efficiency and electron ambiguity type, which are used to categorize events into SRs, VRs and CRs. Two different methods are employed to evaluate them.

- **As as event-by-event weight**
  Theoretical uncertainties which can vary the W_R mass shape are evaluated by fitting the variation-to-nominal ratio with a liner function. Although all $m(W_\mathrm{R})$ distribution is binned in 4 different mass intervals, the liner function is fitted to more finer binned shape. Since the linear function is a function of W_R mass, a variation is given as weight for each event.

- **As an uncertainty of the transfer factor**
  Theory uncertainties can also be estimated as variations of a transfer factor (TF) from Region 1 (R1) to Region 2 (R2):

  $$\Delta_{\text{variation}} = \frac{(N_{\mathrm{R2}}/N_{\mathrm{R1}})_{\text{variation}}}{(N_{\mathrm{R2}}/N_{\mathrm{R1}})_{\text{nominal}}}.$$

  $\Delta_{\text{variation}}$ is estimated for each major MC sample, region and systematic source separately. For the simplicity, only one background component is assumed to exists in R1 and R2. In that case, the expected number of data events in R1 can be expressed by:

  $$\begin{aligned} N_{\mathrm{R1,data}} &= \frac{N_{\mathrm{R2,data}}}{N_{\mathrm{R2,MC}}} \times N_{\mathrm{R1,MC}} = NF \times N_{\mathrm{R1,MC}} \\ &= \frac{N_{\mathrm{R1,MC}}}{N_{\mathrm{R2,MC}}} \times N_{\mathrm{R2,data}} = TF \times N_{\mathrm{R2,data}}. \end{aligned}$$

  Here, NF (a normalization factor) is the parameter estimated by the fit denoted as μ_k in equation 7.1. The systematic variation is applied to TF i.e.

  $$TF \to \Delta_{\text{variation}} \times TF.$$

  The uncertainty sources that vary the MC expectations in R1 and R2 to the same direction are canceled by taking the ratio (TF) in advance. That is why the theoretical uncertainties are not applied to the R1, where the variation sample is normalized to the nominal sample. R1 can be selected arbitrarily, and for each background, a region of high purity is used.

The types of theoretical uncertainties vary depending on the background processes, but most of them come from the same sources. As shown in Section 3.3.1, the inclusive cross-section can differ depending on the choice of PDF, factorization scale (μ_F), renormalisation scale (μ_R) and strong coupling constant (α_s).

There are more than 100 variations available for selecting PDFs, depending on the form of the function form. Envelops of them are taken and the size of PDF variations are evaluated with the largest and smallest variations with respect to the nominal as the up- and down-type, respectively. The uncertainties of the renormalization and factorization scale variation are evaluated by multiplying 2 and 1/2 to the nominal

μ_F and μ_R. Uncertainties on the α_s are given at different value ($\alpha_s = 0.118$ for nominal, $\alpha_s = 0.119$ for up-type, $\alpha_s = 0.117$ for down-type).

$V(W, Z, \gamma)$+jets

The matching of jets by matrix elements and parton showering (CKKW) is accounted for in the event produced by the SHERPA event generator. The nominal value is 20 GeV, but 15 GeV and 30 GeV are used as variation. The error for soft gluon emission (QSF) is also taken into account by varying to 2 and 1/2 with respect to the nominal value. These theoretical uncertainties for V+jets are the largest systematic uncertainties.

QCD multi-jet

Parameters of PYTHIA 8 are tuned for high p_{T} events depending on the multi-parton interaction parameters and initial and final state radiation parameters with PROFESSOR MC tune system [111]. By using variations along the principle directions of the covariance matrix of the parameters at the tuned minimum, systematic uncertainties are evaluated. These uncertainties provide good coverage of the experimental and modelling uncertainties.

Other backgrounds ($t\bar{t}$, di-boson, single-top)

Minor backgrounds have a fixed flat 50 % cross-section uncertainty to cover possible yield variations in all regions. These uncertainties are conservative and it is confirmed that they do not affect the signal sensitivities so much.

Signal

The cross section uncertainties are derived by varying scale variations and PDF sets. The size of fraction of them are about 10 % and 20 % depending on the W_{R} mass, respectively. In both variations, a large amount of change is expected as the W_{R} mass increases.

In addition to the above stuffs, a possible uncertainty due to the choice of generator is accounted to the major background processes. The nominal and alternative generators are given in Table 3.3 and Table 7.1, respectively. The size of uncertainty is obtained by comparing them and symmetrization with respect to the nominal is performed to make it both-side uncertainty.

Table 7.1: Simulated background samples with an alternative generator. The corresponding event generator, parton shower, cross-section normalization, PDF set used for the matrix element and set of tuned parameters are shown for each sample.

Physics process	Generator	PDF set	Cross-section normalization	Parton shower	Tune
$W(\to \ell\nu)$ + jets	MADGRAPH_aMC@NLO	NNPDF3.0NLO	NLO	PYTHIA 8.230	A14
$Z(\to \ell\ell)$ + jets	MADGRAPH_aMC@NLO	NNPDF3.0NLO	NLO	PYTHIA 8.230	A14
γ+jets	PYTHIA 8.230	NNPDF2.3LO	LO	PYTHIA 8.230	A14
QCD multi-jet	SHERPA	CT14	NNLO	SHERPA	SHERPA

7.3.3 Ad-hoc uncertainty

The experimental and theoretical uncertainties are generally large enough to account for variations of MC shapes. However, there are some additional uncertainties to cover mis-modeling found in extra VRs or possible shape variations for the non-calibrated variable of the electron `Ambiguity`.

Mis-modeling of QCD multi-jet MC in extra VR

A data-to-MC disagreement is observed in QCD multi-jet extra VRs with high-W_R mass and this might exist in SR1e. To cover them, the slope of the data-to-MC ratio against the W_R mass distribution is included only for QCD multi-jet. More details are discussed in Section 8.2.

Possible shape variation for electron `Ambiguity`

Even the electron `Ambiguity` is used to define the CRγ1e and CRLow1e to disentangle γ+jets from W+jets, it is a non-calibrated variable. The possible shape variations of W+jets, QCD multi-jet and γ+jets are included by comparing MC with data.

Possible shape variation for high-p_T muon

As described in Section 4.7, higher muon p_T leads larger uncertainty. However, MC does not include perfect detector simulation, so possible shape variation is considered as a systematic uncertainty. This becomes larger as W_R mass increases. Since minor backgrounds have flat 50% cross section uncertainties, this systematic uncertainty is assigned only to Z+jets.

7.3.4 Summary of systematic uncertainties

Figure 7.1 shows the relative size of individual systematic uncertainties and total uncertainties by taking into account the correlations on the background prediction in SR1e, SR2e and SR2mu. The dominant systematic uncertainty in SRs is the theoretical uncertainty. Because the total uncertainties takes correlations between various systematic uncertainties into account, there are some regions in which the total uncertainty is smaller than the individual systematic uncertainties. Since SR1e and SR2e are fitted simultaneously, systematic uncertainties are correlated. On the other hand, SR2mu is a single SR in muon channel.

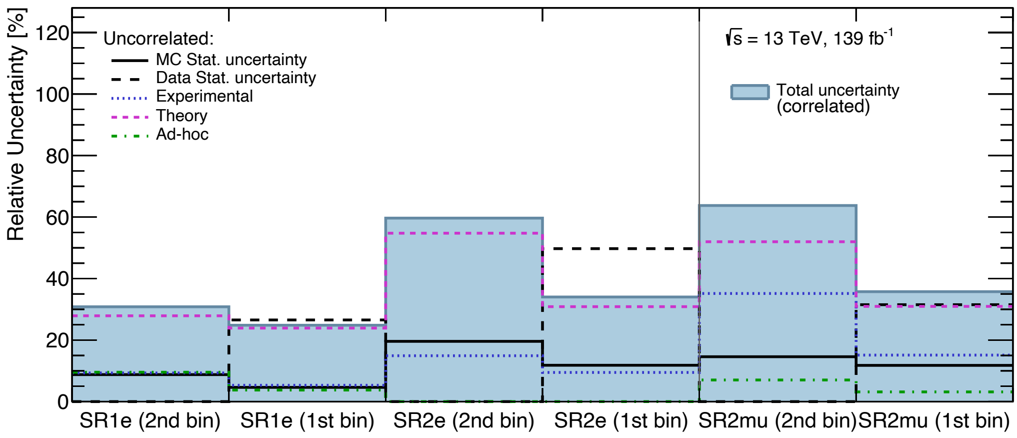

Figure 7.1: Breakdown of the systematic uncertainties on the background prediction and total uncertainties by taking into account the correlations.

8 Extra VRs fit result

This chapter shows the results of the background only fit to the extra VRs introduced in Chapter 6. Summary of purposes for each extra VRs fit can be found in Table 8.1. To get straight to the point, reasonable data-to-MC agreements are observed in all the extra VRs fits. This means that good background estimation in every SRs can be anticipated.

Table 8.1: Summary of purposes of extra VRs fits. Details and region definitions can be found and fit results can be found in corresponding section.

Process	Purpose	Details in	Results in
W+jets	To confirm that W+jets estimation with the $\cos\theta$ and $m(W_R)$ distributions reproduces data well in the regions with the inverted electron p_T and E_T^{miss}.	Section 6.1.1	Section 8.1
QCD multi-jet	To confirm that QCD multi-jet estimation with the electron isolation and $m(W_R)$ distributions reproduces data well in the regions with the inverted electron identification.	Section 6.1.2	Section 8.2
γ+jets	To confirm that the $m(W_R)$ distribution of γ+jets MC reproduces data well in high purity phase spaces, which require a photon instead of an electron.	Section 6.1.3.1	Section 8.3.1
	To confirm that the $m(W_R)$ distribution of γ+jets MC reproduces the data well regardless of the photon-to-electron fake factor.	Section 6.1.3.2	Section 8.3.2
$Z(\rightarrow ee)$+jets	To confirm that $Z(\rightarrow ee)$+jets estimation with the $m(W_R)$ distribution reproduces data well in the regions with the different di-electron mass interval.	Section 6.2	Section 8.4.1
$Z(\rightarrow \mu\mu)$+jets	To confirm that $Z(\rightarrow \mu\mu)$+jets estimation with the $m(W_R)$ distribution reproduces data well in the regions with the different di-muon mass interval.	Section 6.3	Section 8.4.2

8.1 W+jets

As discussed in Section 6.1.1, a background only fit to $\mathrm{VRW}_{\mathrm{CRLow1e}}$ and $\mathrm{VRW}_{\mathrm{CRW1e}}$ with a full set of systematic uncertainties is performed to obtain the normalization factor for W+jets. This normalization factor is then applied to the W+jets samples in $\mathrm{VRW}_{\mathrm{SR1e}}$. The impacts of fitted systematic uncertainties are transferred into $\mathrm{VRW}_{\mathrm{SR1e}}$ as well.

The post-fit background yield in each region is shown in Table 8.2 with the number of observed data. The fitted normalization factor for W+jets is 1.00 ± 0.05. The observed number of data in the first and second bin of $\mathrm{VRW}_{\mathrm{SR1e}}$ are 253 and 20, respectively. While the total post-fit MC event in them are 250.3 ± 26.5 and 13.1 ± 1.6 which correspond to agreements within 2σ as shown in Figure 8.1. Since W+jets normalization factor has large anti-correlations with the cross section uncertainties of $t\bar{t}$ and di-boson as shown in Figure 8.2, the error of total post-fit yield becomes smaller than the error of individual process.

Table 8.2: Results of background-only fit to $\mathrm{VRW}_{\mathrm{CRW1e}}$ for integrated luminosity of 139 fb^{-1}. The errors are statistical plus systematic uncertainties. Uncertainties on the fitted yields are symmetric by construction, where the negative error is truncated when reaching to zero event yield. "–" indicates exactly zero event is expected. The most bottom row shows the total pre-fit MC events.

channel	$\mathrm{VRW}_{\mathrm{CRW1e}}$	$\mathrm{VRW}_{\mathrm{CRLow1e}}$	$\mathrm{VRW}_{\mathrm{SR1e}}$ (1st bin)	$\mathrm{VRW}_{\mathrm{SR1e}}$ (2nd bin)
Observed events	7774	9247	253	20
Fitted bkg events	7783.3 ± 86.4	9237.6 ± 99.9	250.3 ± 26.5	13.1 ± 1.6
Fitted W+jets events	6668.4 ± 378.9	8127.7 ± 387.9	215.5 ± 27.7	12.4 ± 1.4
Fitted $t\bar{t}$ events	481.6 ± 277.8	403.0 ± 236.3	8.2 ± 5.1	–
Fitted di-boson events	400.2 ± 202.1	465.4 ± 235.4	21.8 ± 11.0	0.4 ± 0.4
Fitted Z+jets events	115.5 ± 57.8	143.4 ± 72.3	2.3 ± 1.2	0.1 ± 0.1
Fitted single-top events	107.4 ± 60.9	95.5 ± 53.4	2.6 ± 1.6	0.2 ± 0.2
Fitted QCD multi-jet events	$10.3^{+24.1}_{-10.3}$	2.6 ± 1.6	$0.0^{+0.0}_{-0.0}$	$0.0^{+0.0}_{-0.0}$
Fitted γ+jets events	–	–	–	–
Pre-fit background events	7921.0	9283.9	252.4	13.2

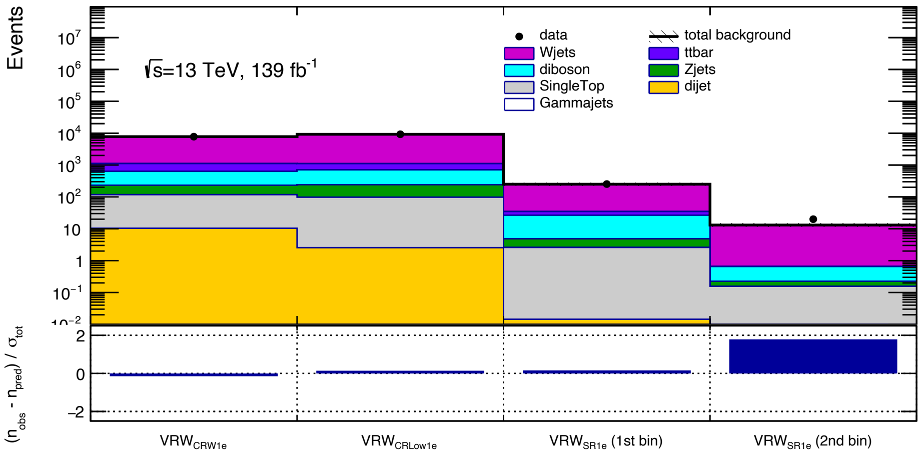

Figure 8.1: Data vs post-fit MC expectation of W+jets extra VRs. The bottom panel shows the ratio of difference between observed data and post-fit MC expectation divided by the total uncertainty σ_{tot}.

The main sources of the uncertainties are theoretical uncertainties and MC statistics in the highest-W_{R} mass bins. Since the upper cut for lepton p_{T} is applied, the impact of jet energy scale is relatively significant.

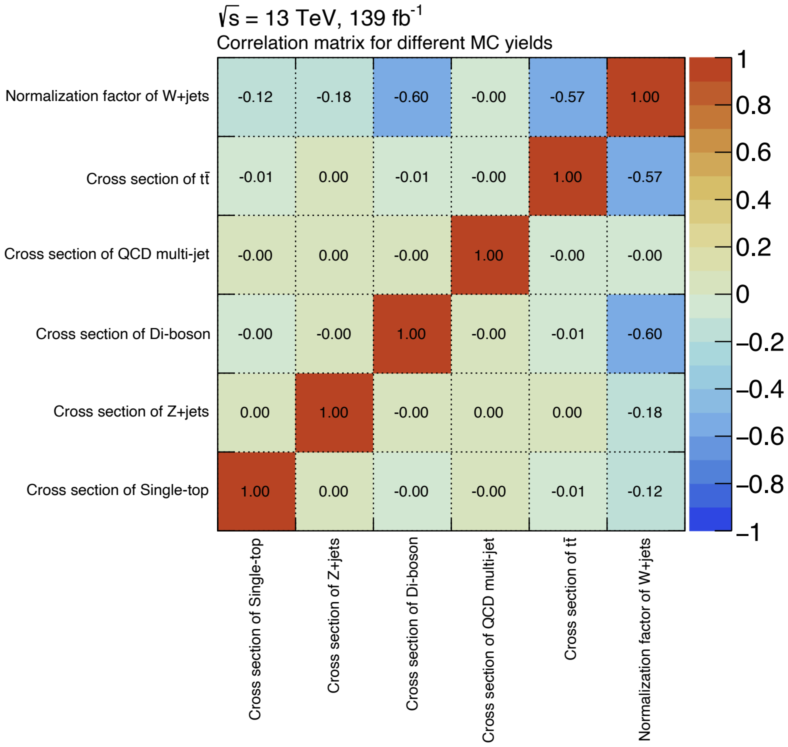

Figure 8.2: Post-fit correlation matrix of the W+jets normalization factor and cross section uncertainties for minor backgrounds obtained by the extra W+jets VRs fit. Since the γ+jets yields are exactly zero in all regions, cross section uncertainty for that is not shown.

8.2 QCD multi-jet

As discussed in Section 6.1.2, a background only fit to $\text{VRFake}_{\text{CRLow1e}}$ and $\text{VRFake}_{\text{CRFake1e}}$ with a full set of systematic uncertainties is performed to obtain the normalization factor for QCD multi-jet. This normalization factor is then applied to the QCD multi-jet sample in $\text{VRFake}_{\text{SR1e}}$. The impacts of fitted systematic uncertainties are transferred into $\text{VRFake}_{\text{SR1e}}$ as well.

The post-fit background yield in each region is shown in Table 8.3 with the number of observed events in data. The fitted normalization factor for QCD multi-jet is 0.82 ± 0.02. The observed number of data in the first and second bin of $\text{VRFake}_{\text{SR1e}}$ are 58 and 6, respectively. While the total fitted MC event in them are 928.6 ± 161.8 and 126.7 ± 44.5 which correspond to agreements within 1σ as shown in Figure 8.3.

In the region of W_{R} mass up to 3 TeV, MC agrees data within 1σ, however there is a positive slope in the data to MC ratio as shown in the bottom panel of Figure 8.3, which may lead to underestimation of the number of MC events in the region above 3 TeV. To avoid this, data to MC ratio is fitted with a linear function to obtain possible shape variation only to QCD multi-jet events.

The main sources of the uncertainties are theoretical uncertainties and MC statistics in the highest-W_{R} mass bins. Electron energy scales and jet energy resolution uncertainties are also significant.

Table 8.3: Results of $\mathrm{VRFake}_{\mathrm{CRFake1e}}$ for integrated luminosity of 139 fb^{-1}. The errors are statistical plus systematic uncertainties. Uncertainties on the fitted yields are symmetric by construction, where the negative error is truncated when reaching to zero event yield. "–" indicates exactly zero event is expected.

channel	$\mathrm{VRFake}_{\mathrm{CRFake1e}}$	$\mathrm{VRFake}_{\mathrm{CRLow1e}}$	$\mathrm{VRFake}_{\mathrm{SR1e}}$ (1st bin)	$\mathrm{VRFake}_{\mathrm{SR1e}}$ (2nd bin)
Observed events	1538	11945	995	168
Fitted bkg events	1538.2 ± 39.5	11945.4 ± 109.3	928.6 ± 161.8	126.7 ± 44.5
Fitted QCD multi-jet events	1263.0 ± 69.3	11887.8 ± 134.4	922.4 ± 162.0	126.1 ± 44.5
Fitted γ+jets events	29.7 ± 17.3	17.4 ± 9.4	1.3 ± 0.8	0.1 ± 0.1
Fitted W+jets events	179.1 ± 90.0	29.3 ± 14.7	3.4 ± 2.0	0.4 ± 0.3
Fitted Z+jets events	47.1 ± 23.7	6.7 ± 3.4	0.4 ± 0.2	0.1 ± 0.1
Fitted di-boson events	12.4 ± 6.4	1.7 ± 0.9	0.1 ± 0.1	$0.0^{+0.0}_{-0.0}$
Fitted $t\bar{t}$ events	5.3 ± 3.3	2.4 ± 1.5	1.0 ± 0.8	–
Fitted single-top events	1.7 ± 1.1	$0.1^{+0.2}_{-0.1}$	–	–
Pre-fit background events	2811.8	15216.7	1179.8	157.5

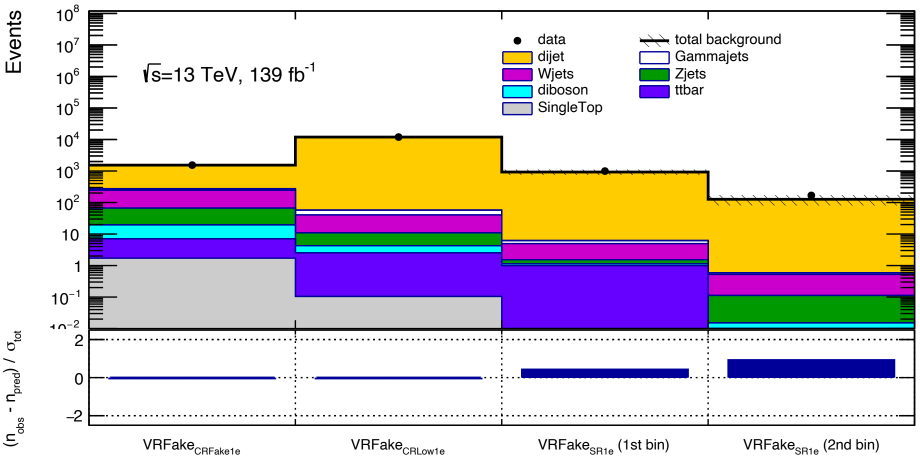

Figure 8.3: Data vs post-fit MC expectation of QCD multi-jet extra VRs. Bottom panel shows the ratio of difference between observed data and post-fit MC expectation divided by the total uncertainty σ_{tot}. A positive slope is observed from $\mathrm{VRFake}_{\mathrm{CRLow1e}}$ to $\mathrm{VRFake}_{\mathrm{SR1e}}$.

8.3 γ+jets

Validations of the γ+jets estimation method are made in two steps. First, the modeling of γ+jets MC is checked in the regions with the exactly same phase spaces to actual CRs and SR except requiring a photon instead of an electron. Then a possible mis-modeling of the photon to electron fake factor is studied with two different sets of extra VRs.

8.3.1 Data to MC agreement in high-W_R mass

As discussed in Section 6.1.3.1, a background only fit to CRLow1ph and CRFake1ph with a full set of systematic uncertainties are performed to obtain the normalization factors for QCD multi-jet and γ+jets. These normalization factors are then applied to the QCD multi-jet and γ+jets events in SR1ph, respectively. The impacts of fitted systematic uncertainties are transferred into SR1ph as well.

The post-fit background yields in each region is shown in Table 8.4 with the number of event in data. The fitted normalization factors for QCD multi-jet and γ+jets are 0.56 ± 0.02 and 0.19 ± 0.06, respectively. The number of observed data in the first and second bins of SR1ph are 33 and 5, respectively. While the total MC events in them are 27.5 ± 4.6 and 3.4 ± 0.9 which correspond to agreements within 1σ as shown in Figure 8.4.

Table 8.4: Results of background-only fit to CRLow1ph and CRFake1ph for integrated luminosity of 139 fb^{-1}. The errors are statistical plus systematic uncertainties. Uncertainties on the fitted yields are symmetric by construction, where the negative error is truncated when reaching to zero event yield. "–" indicates exactly zero event is expected. The most bottom row shows the total pre-fit MC events.

channel	CRFake1ph	CRLow1ph	VR1ph	SR1ph (1st bin)	SR1ph (2nd bin)
Observed events	6904	11500	327	33	5
Fitted bkg events	6903.9 ± 83.1	11500.2 ± 107.2	365.2 ± 34.5	27.5 ± 4.6	3.4 ± 0.9
Fitted γ+jets events	1729.9 ± 86.2	7839.7 ± 201.2	243.7 ± 25.3	16.5 ± 2.9	1.8 ± 0.5
Fitted QCD multi-jet events	5125.9 ± 130.4	3586.1 ± 154.6	119.9 ± 21.8	11.0 ± 3.6	1.5 ± 0.8
Fitted $t\bar{t}$ events	16.6 ± 11.4	7.5 ± 6.3	0.1 ± 0.1	–	–
Fitted W+jets events	19.5 ± 9.7	42.9 ± 21.5	1.0 ± 0.6	0.1 ± 0.0	0.0 ± 0.0
Fitted Z+jets events	8.9 ± 4.5	18.8 ± 9.4	0.3 ± 0.1	0.0 ± 0.0	–
Fitted single-top events	2.5 ± 1.8	2.9 ± 2.0	0.3 ± 0.2	–	–
Fitted di-boson events	0.7 ± 0.4	2.4 ± 1.3	–	–	–
Pre-fit background events	18136.2	47230.8	1482.7	105.4	12.3

The shape modeling of the γ+jets MC is reliable in the phase space requiring only one large-R jet and a photon, except for its normalization. The normalization can be determined properly from data in the CRs.

8.3.2 Photon to electron fake factor

As discussed in Section 6.1.3.2, two sets of extra VRs are prepared, one is the regions with $\Delta\eta$ from 2.0 to 3.0 to ensure an orthogonality with the actual CRs and SR and the other one is further requesting a photon instead of an electron, to ensure that the photon to electron fake factor is well modeled in MC and does not affect the W_R mass reconstruction. In the following, data-to-MC agreements obtained by those two independent fits are depicted.

- A background only fit to VR$\gamma_{\mathrm{CRLow1e}}$, VR$\gamma_{\mathrm{CRW1e}}$ and VR$\gamma_{\mathrm{CRFake1e}}$ with a full set of systematic uncertainties is performed to obtain the normalization factors for W+jets, QCD multi-jet and γ+jets. These normalization factors are then applied to the corresponding background processes. The impacts of fitted systematic uncertainties are transferred into VRγ_{SR1e} as well.

  The post-fit background yield in each region is shown in Table 8.5 with the number of events in data. The fitted normalization factors for W+jets, QCD multi-jet and γ+jets are 0.97 ± 0.11, 0.43 ± 0.02

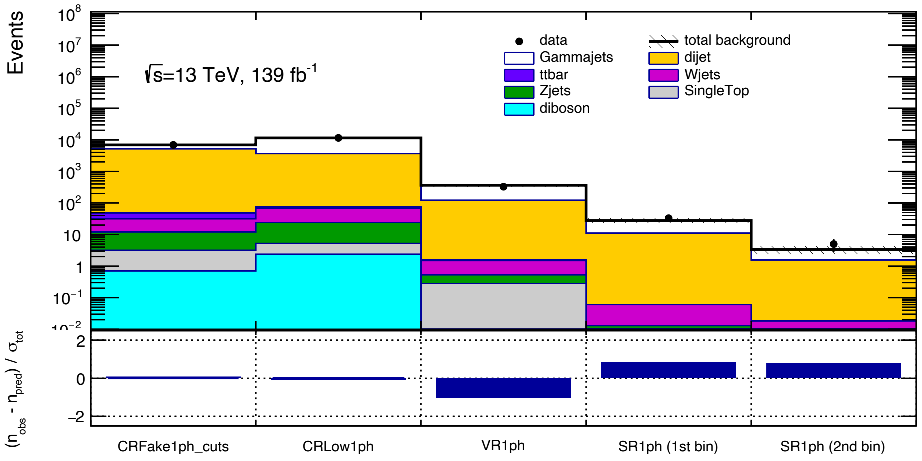

Figure 8.4: Data vs post-fit MC expectation of γ+jets extra VRs with the exactly same phase space with SR1e except requiring a photon instead of an electron. Bottom panel shows the ratio of difference between observed data and post-fit MC expectation divided by the total uncertainty σ_{tot}.

and 0.24 ± 0.01, respectively. The number of observed data in the first and second bin of VRγ_{SR1e} are 26 and 3, respectively. While the total MC events in them are 27.7 ± 7.7 and 1.7 ± 0.6 which correspond to agreements within 1σ as shown in Figure 8.5.

Table 8.5: Results of background-only fit to VRγ_{CRLow1e} and VRγ_{CRFake1e} for integrated luminosity of 139 fb^{-1}. The errors are statistical plus systematic uncertainties. Uncertainties on the fitted yields are symmetric by construction, where the negative error is truncated when reaching to zero event yield. "–" indicates exactly zero event is expected. The most bottom row shows the total pre-fit MC events.

channel	VRγ_{CRW1e}	VRγ_{CRFake1e}	VRγ_{CRLow1e}	VRγ_{SR1e} (1st bin)	VRγ_{SR1e} (2nd bin)
Observed events	4709	3811	796	26	3
Fitted bkg events	4708.8 ± 68.8	3810.9 ± 61.8	796.0 ± 28.1	27.7 ± 7.7	1.7 ± 0.6
Fitted γ+jets events	630.4 ± 413.5	537.0 ± 265.9	242.7 ± 118.9	12.6 ± 8.1	0.7 ± 0.4
Fitted W+jets events	2943.1 ± 500.1	268.4 ± 93.8	234.6 ± 82.2	6.2 ± 3.5	0.3 ± 0.3
Fitted QCD multi-jet events	285.0 ± 64.5	2747.6 ± 195.1	104.9 ± 18.4	3.1 ± 1.0	0.4 ± 0.2
Fitted Z+jets events	495.4 ± 67.4	228.7 ± 37.4	187.9 ± 33.4	5.2 ± 1.9	0.3 ± 0.2
Fitted $t\bar{t}$ events	153.5 ± 90.1	9.9 ± 6.3	5.4 ± 3.7	–	–
Fitted di-boson events	168.0 ± 84.5	17.4 ± 9.8	17.8 ± 9.7	0.7 ± 0.4	0.0 ± 0.0
Fitted single-top events	33.4 ± 19.0	2.0 ± 1.5	2.7 ± 1.7	–	–
Pre-fit background events	8201.1	9379.7	1788.2	73.5	4.5

- A background only fit to VRγ_{CRLow1ph} and VR$\gamma_{\text{CRFake1ph}}$ with a full set of systematic uncertainties is performed to obtain the normalization factors for QCD multi-jet and γ+jets. These normalization factors are than applied to the corresponding background processes. The impacts of fitted systematic uncertainties are transferred into VRγ_{SR1ph} as well.

The post-fit background yield in each region is shown in Table 8.6 with the number of events in data. The fitted normalization factors for QCD multi-jet and γ+jets are 0.49 ± 0.03 and 0.12 ± 0.01, respectively. The number of observed data in the first and second bin of VRγ_{SR1ph} are 48 and 4,

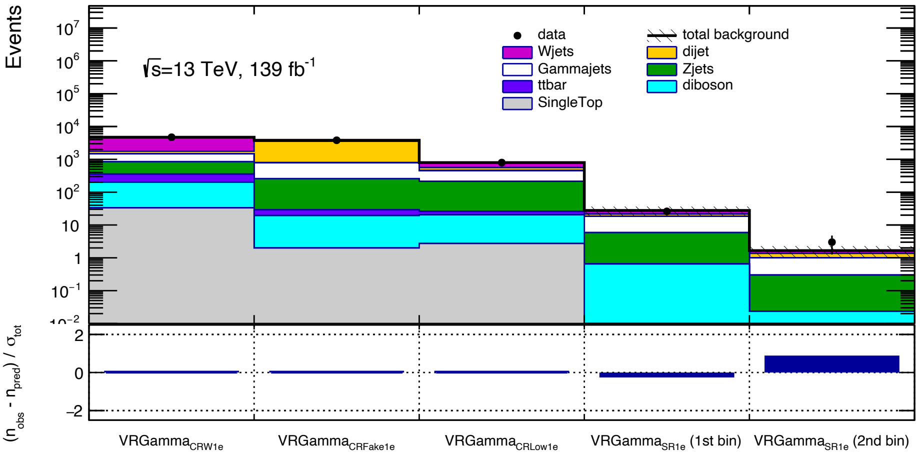

Figure 8.5: Data vs post-fit expectation of γ+jets extra VRs with different $\Delta\eta$ interval compared to SR1e. Bottom panel shows the ratio of difference between observed data and post-fit MC expectation divided by the total uncertainty σ_{tot}.

respectively. While the total MC events in them are 59.2 ± 7.3 and 4.6 ± 1.0 which correspond to agreements within 1σ as shown in Figure 8.6.

Table 8.6: Results of background-only fit to VRγ_{CRLow1ph} and VR$\gamma_{\text{CRFake1ph}}$ for integrated luminosity of 139 fb^{-1}. The errors are statistical plus systematic uncertainties. Uncertainties on the fitted yields are symmetric by construction, where the negative error is truncated when reaching to zero event yield. "–" indicates exactly zero event is expected. The most bottom row shows the total pre-fit MC events.

channel	VR$\gamma_{\text{CRFake1ph}}$	VRγ_{CRLow1ph}	VRγ_{SR1ph} (1st bin)	VRγ_{SR1ph} (2nd bin)
Observed events	7281	1312	48	4
Fitted bkg events	7281.0 ± 85.4	1312.0 ± 36.3	59.2 ± 7.3	4.6 ± 1.0
Fitted γ+jets events	1516.9 ± 225.5	860.1 ± 92.4	39.4 ± 6.5	2.9 ± 0.8
Fitted QCD multi-jet events	5723.6 ± 246.7	444.1 ± 82.8	19.7 ± 4.2	1.7 ± 0.7
Fitted W+jets events	23.6 ± 11.9	2.9 ± 1.9	–	–
Fitted Z+jets events	5.9 ± 3.0	2.9 ± 1.5	0.1 ± 0.1	–
Fitted $t\bar{t}$ events	9.4 ± 5.8	1.5 ± 1.5	–	–
Fitted di-boson events	0.7 ± 0.3	0.3 ± 0.2	–	–
Fitted single-top events	1.0 ± 0.5	0.2 ± 0.1	–	–
Pre-fit background events	24102.9	7960.4	363.0	27.5

Consequently, it is confirmed that the photon to electron fake factor is well modeled by MC and the W_{R} mass can be correctly reconstructed using MC even when a fake electron is requested.

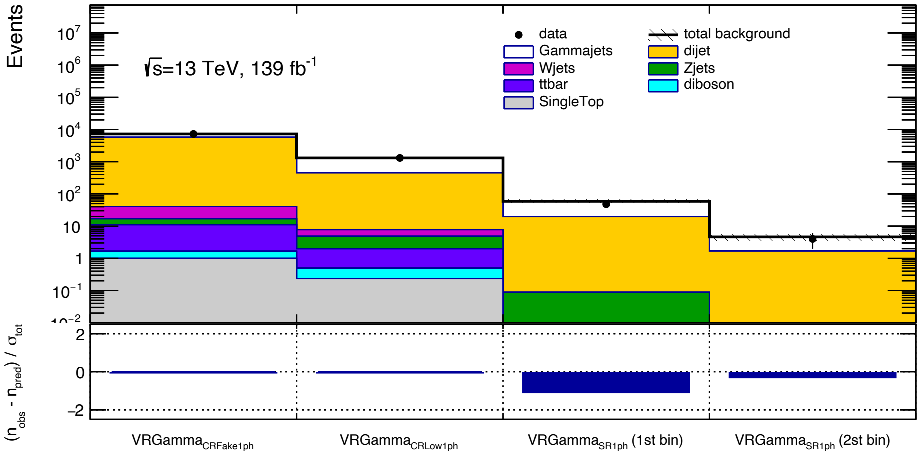

Figure 8.6: Data vs post-fit MC expectation of γ+jets extra VRs defined in Table 6.7. Bottom panel shows the ratio of difference between observed data and post-fit MC divided by the total uncertainty. σ_{tot}.

8.4 Z+jets

8.4.1 $m(W_\mathrm{R})$ modeling of $Z(\rightarrow ee)$ sample

A background only fit to VRZ$_{\text{CRLow2e}}$ with a full set of systematic uncertainties is performed to obtain the normalization factor for $Z(\rightarrow ee)$+jets. This normalization factor is then applied to the Z+jets events in VRZ$_{\text{SR2e}}$. The impacts of fitted systematic uncertainties are transferred into VRZ$_{\text{SR2e}}$ as well.

The post-fit background yield in each region is shown in Table 8.7 with the number of events in data. The fitted normalization factor for $Z(\rightarrow ee)$+jets is 1.27 ± 0.09. The number of observed data in the first and second bin of VRZ$_{\text{SR2e}}$ are 17 and 1, respectively. While the total fitted MC event in them are 14.7 ± 3.9 and 1.2 ± 0.7 which correspond to agreements within 1σ as shown in Figure 8.7.

8.4.2 $m(W_\mathrm{R})$ mass modeling of $Z(\rightarrow \mu\mu)$ sample

A background only fit to VRZ$_{\text{CRLow2mu}}$ with a full set of systematic uncertainties is performed to obtain the normalization factor for $Z(\rightarrow \mu\mu)$+jets. This normalization factor is then applied to the Z+jets events in VRZ$_{\text{SR2mu}}$. The impacts of fitted systematic uncertainties are transferred into VRZ$_{\text{SR2mu}}$ as well.

The post-fit background yield in each region is shown in Table 8.8 with the number of events in data. The fitted normalization factor for $Z(\rightarrow \mu\mu)$+jets is 1.17 ± 0.04. The number of observed data in the first and second bin of VRZ$_{\text{SR2mu}}$ are 23 and 2, respectively. While the total fitted MC event in them are 22.3 ± 5.7 and 3.7 ± 2.2 which correspond to agreements within 1σ as shown in Figure 8.8.

Table 8.7: Results of background-only fit to $\mathrm{VRZ}_{\mathrm{CRLow2e}}$ for integrated luminosity of 139 fb^{-1}. The errors are statistical plus systematic uncertainties. Uncertainties on the fitted yields are symmetric by construction, where the negative error is truncated when reaching to zero event yield. "–" indicates exactly zero event is expected. The most bottom row shows the total pre-fit MC events.

channel	$\mathrm{VRZ}_{\mathrm{CRLow2e}}$	$\mathrm{VRZ}_{\mathrm{SR2e}}$ (1st bin)	$\mathrm{VRZ}_{\mathrm{SR2e}}$ (2nd bin)
Observed events	358	17	1
Fitted bkg events	358.0 ± 18.9	14.7 ± 3.9	1.2 ± 0.7
Fitted Z+jets events	321.1 ± 22.6	13.3 ± 3.9	1.2 ± 0.7
Fitted di-boson events	21.2 ± 10.6	0.8 ± 0.4	0.1 ± 0.0
Fitted $t\bar{t}$ events	8.8 ± 4.9	0.2 ± 0.1	–
Fitted W+jets events	2.0 ± 1.0	0.4 ± 0.2	0.0 ± 0.0
Fitted single-top events	1.5 ± 1.0	–	–
Fitted QCD multi-jet events	–	0.0 ± 0.0	–
Fitted γ+jets events	3.4 ± 1.9	–	–
Pre-fit background events	289.1	11.8	1.0

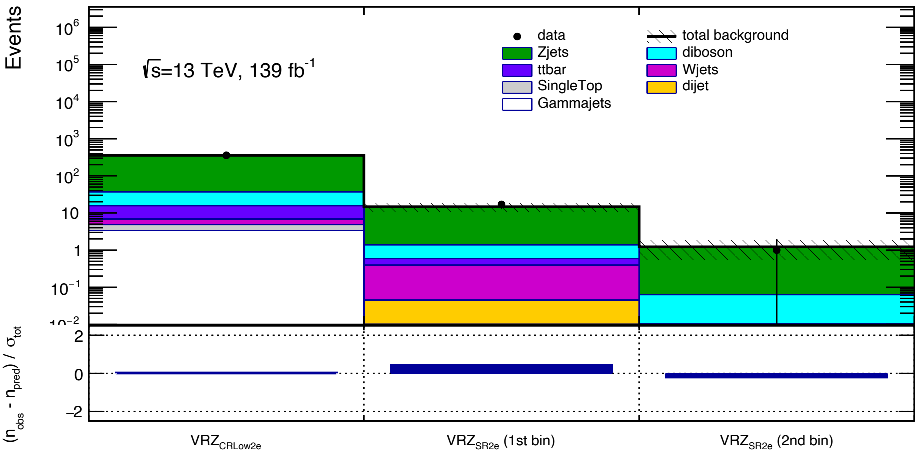

Figure 8.7: Data vs post-fit MC expectation of $Z(\rightarrow ee)$+jets extra VRs. Bottom panel shows the ratio of difference between observed data and post-fit MC expectation divided by the total uncertainty σ_{tot}.

Table 8.8: Results of background-only fit to $\mathrm{VRZ}_{\mathrm{CRLow2mu}}$ for integrated luminosity of 139 fb^{-1}. The errors are statistical plus systematic uncertainties. Uncertainties on the fitted yields are symmetric by construction, where the negative error is truncated when reaching to zero event yield. "–" indicates exactly zero event is expected. The most bottom row shows the total pre-fit MC events.

channel	$\mathrm{VRZ}_{\mathrm{CRLow2mu}}$	$\mathrm{VRZ}_{\mathrm{SR2mu}}$ (1st bin)	$\mathrm{VRZ}_{\mathrm{SR2mu}}$ (2nd bin)
Observed events	399	23	2
Fitted bkg events	399.1 ± 20.0	22.3 ± 5.7	3.7 ± 2.2
Fitted Z+jets events	337.6 ± 29.1	19.1 ± 5.8	3.2 ± 2.2
Fitted di-boson events	33.3 ± 16.7	1.8 ± 0.9	0.3 ± 0.2
Fitted $t\bar{t}$ events	18.2 ± 10.7	0.8 ± 0.5	0.2 ± 0.1
Fitted W+jets events	6.8 ± 3.6	0.3 ± 0.3	0.0 ± 0.0
Fitted single-top events	3.1 ± 2.0	0.3 ± 0.2	–
Fitted QCD multi-jet events	0.1 ± 0.1	0.1 ± 0.1	–
Fitted γ+jets events	–	–	–
Pre-fit background events	412.9	23.1	3.8

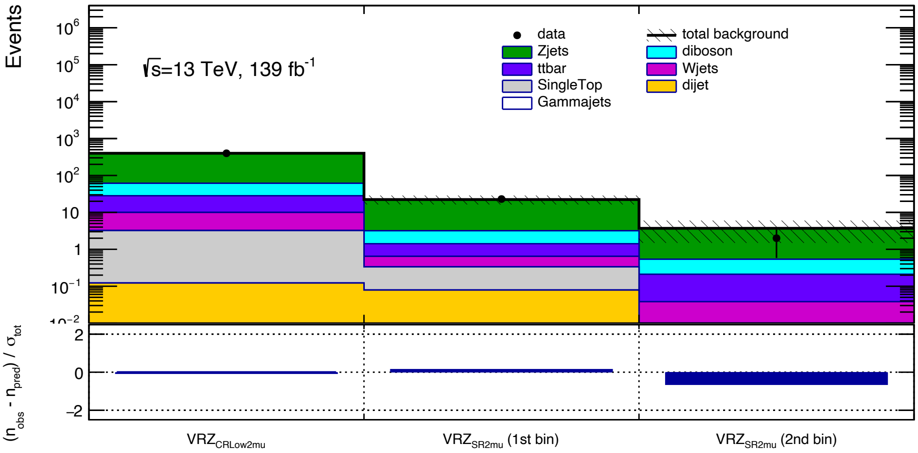

Figure 8.8: Data vs post-fit MC expectation of $Z(\rightarrow \mu\mu)$+jets extra VRs. Bottom panel shows the ratio of difference between observed data and post-fit MC expectation divided by the total uncertainty. σ_{tot} represents the total uncertainty.

9 Results

The background estimation methods explained in Section 6 have been performed in extra VRs in Section 8. Generally good MC to data consistencies are observed in the post-fit level.

Results of simultaneous fit with three different fitting configurations are presented in this section. Section 9.1 shows the results of background only fits to electron and muon final state separately. The results of model independent fit are reported in Section 9.2 followed by model dependent fit results in Section 9.3.

9.1 Search for the signal with background only fits

9.1.1 Electron final states

As discussed in Section 6.1 and 6.2, a background only fit to CRW1e, CRFake1e, CRγ1e, CRLow1e and CRLow2e with a full set of systematic uncertainties is performed to estimate normalization factors for W+jets, QCD multi-jet, γ+jets and Z+jets. These normalization factors are then applied in heavier mass regions. As summarized in Table 6.11, W+jets, QCD multi-jet and γ+jets normalization factors are applied to one electron regions only, while Z+jets normalization factor is transferred into both one and two electron channels.

The post-fit yield in each region is shown in Table 9.1-9.4 with the number of events in data. The fitted normalization factors for W+jets, QCD multi-jet, γ+jets and Z+jets are 1.05 ± 0.03, 0.56 ± 0.01, 0.38 ± 0.06 and 1.23 ± 0.10, respectively. The number of observed data in the first and second bin of SR1e are 10 and 0, respectively, while the total fitted MC in them are 11.9 ± 2.9 and 0.8 ± 0.3, respectively. The number of observed data in the first and second bin of SR2e are 3 and 0, while the total fitted MC in them are 3.5 ± 1.2 and 0.3 ± 0.2, respectively. As shown in Figure 9.1, the MC reproduces the data very well in all regions. These results indicate no signal is found in the all SRs.

Table 9.1: Results of background-only fit to CRLow1e, CRW1e, CRFake1e and CRLow2e for integrated luminosity of 139 fb^{-1}. The errors are statistical plus systematic uncertainties. Uncertainties on the fitted yields are symmetric by construction, where the negative error is truncated when reaching to zero event yield. "–" indicates exactly zero event is expected. The most bottom row shows the total pre-fit MC events.

channel	CRW1e	VRW1e (1st bin)	VRW1e (2nd bin)
Observed events	5631	37	0
Fitted bkg events	5634.9 ± 74.7	34.5 ± 7.1	0.4 ± 0.2
Fitted W+jets events	4856.1 ± 173.8	28.8 ± 6.8	0.4 ± 0.2
Fitted $t\bar{t}$ events	172.3 ± 108.1	1.2 ± 0.8	–
Fitted di-boson events	251.2 ± 125.7	2.49 ± 1.72	–
Fitted γ+jets events	95.1 ± 38.3	$0.6^{+0.9}_{-0.6}$	–
Fitted Z+jets events	111.8 ± 31.8	0.6 ± 0.3	$0.0^{+0.0}_{-0.0}$
Fitted single-top events	60.5 ± 35.3	$0.3^{+0.6}_{-0.3}$	–
Fitted QCD multi-jet events	87.6 ± 16.2	0.5 ± 0.23	$0.0^{+0.0}_{-0.0}$
Pre-fit background events	5827.4	36.4	0.4

Table 9.2: Results of background-only fit to CRLow1e, CRW1e, CRFake1e and CRLow2e for integrated luminosity of 139 fb^{-1}. The errors are statistical plus systematic uncertainties. Uncertainties on the fitted yields are symmetric by construction, where the negative error is truncated when reaching to zero event yield. "–" indicates exactly zero event is expected. The most bottom row shows the total pre-fit MC events.

channel	CRFake1e	VRFake1e (1st bin)	VRFake1e (2nd bin)
Observed events	14988	809	101
Fitted bkg events	14987.9 ± 122.6	716.4 ± 109.7	101.2 ± 46.7
Fitted QCD multi-jet events	13834.6 ± 151.5	673.4 ± 109.6	66.5 ± 34.7
Fitted W+jets events	348.4 ± 16.3	8.3 ± 2.2	0.6 ± 0.4
Fitted γ+jets events	626.9 ± 86.2	28.2 ± 5.1	32.9 ± 15.5
Fitted Z+jets events	121.7 ± 10.4	3.8 ± 0.9	0.7 ± 0.4
Fitted $t\bar{t}$ events	27.6 ± 16.7	1.2 ± 0.8	0.3 ± 0.2
Fitted di-boson events	23.8 ± 12.1	1.1 ± 0.8	0.2 ± 0.1
Fitted single-top events	5.1 ± 2.7	0.3 ± 0.2	–
Pre-fit background events	26883.4	1291.5	206.5

Table 9.3: Results of background only fit to CRLow1e, CRW1e, CRFake1e, CRγ1e and CRLow2e for integrated luminosity of 139 fb^{-1}. The errors are statistical plus systematic uncertainties. Uncertainties on the fitted yields are symmetric by construction, where the negative error is truncated when reaching to zero event yield. "–" indicates exactly zero event is expected. The most bottom row shows the total pre-fit MC events.

channel	CRLow1e	CRγ1e	VR1e	SR1e (1st bin)	SR1e (2nd bin)
Observed events	7988	4611	239	10	0
Fitted bkg events	7983.1 ± 89.6	4611.3 ± 68.1	249.4 ± 34.7	11.9 ± 2.9	0.8 ± 0.3
Fitted W+jets events	5849.6 ± 159.7	1502.9 ± 120.2	140.7 ± 33.3	5.6 ± 2.7	0.3 ± 0.2
Fitted γ+jets events	278.8 ± 51.5	1365.5 ± 155.2	31.6 ± 5.4	2.0 ± 0.5	0.2 ± 0.1
Fitted QCD multi-jet events	89.1 ± 53.7	1101.6 ± 38.8	29.1 ± 4.8	2.2 ± 0.8	0.2 ± 0.1
Fitted Z+jets events	1350.9 ± 108.4	482.6 ± 39.1	29.4 ± 6.0	1.1 ± 0.5	$0.0^{+0.0}_{-0.0}$
Fitted di-boson events	309.9 ± 156.7	87.8 ± 44.4	13.5 ± 6.9	0.7 ± 0.4	0.1 ± 0.1
Fitted $t\bar{t}$ events	58.8 ± 38.0	52.9 ± 32.9	3.0 ± 1.8	0.2 ± 0.1	–
Fitted single-top events	46.0 ± 28.6	18.1 ± 10.5	2.0 ± 2.0	$0.1^{+0.2}_{-0.1}$	–
Pre-fit background events	7886.9	7509.1	309.4	16.5	1.3

Table 9.4: Results of background-only fit to CRLow1e, CRW1e, CRFake1e and CRLow2e for integrated luminosity of 139 fb^{-1}. The errors are statistical plus systematic uncertainties. Uncertainties on the fitted yields are symmetric by construction, where the negative error is truncated when reaching to zero event yield. "–" indicates exactly zero event is expected. The most bottom row shows the total pre-fit MC events.

channel	CRLow2e	VR2e	SR2e (1st bin)	SR2e (2nd bin)
Observed events	751	39	3	0
Fitted bkg events	751.8 ± 27.5	43.4 ± 7.4	3.5 ± 1.2	0.3 ± 0.2
Fitted Z+jets events	622.5 ± 50.8	34.8 ± 7.6	2.7 ± 1.2	0.3 ± 0.2
Fitted $t\bar{t}$ events	28.8 ± 17.8	1.0 ± 0.5	0.2 ± 0.2	–
Fitted W+jets events	17.8 ± 8.9	2.1 ± 1.1	0.2 ± 0.1	$0.0^{+0.0}_{-0.0}$
Fitted single-top events	8.4 ± 4.9	$0.2^{+0.3}_{-0.2}$	0.0 ± 0.0	–
Fitted γ+jets events	3.1 ± 1.5	0.8 ± 0.4	$0.0^{+0.0}_{-0.0}$	–
Fitted di-boson events	71.3 ± 35.2	4.3 ± 2.1	0.3 ± 0.2	–
Fitted QCD multi-jet events	–	0.2 ± 0.1	–	–
Pre-fit background events	638.3	36.9	3.0	0.3

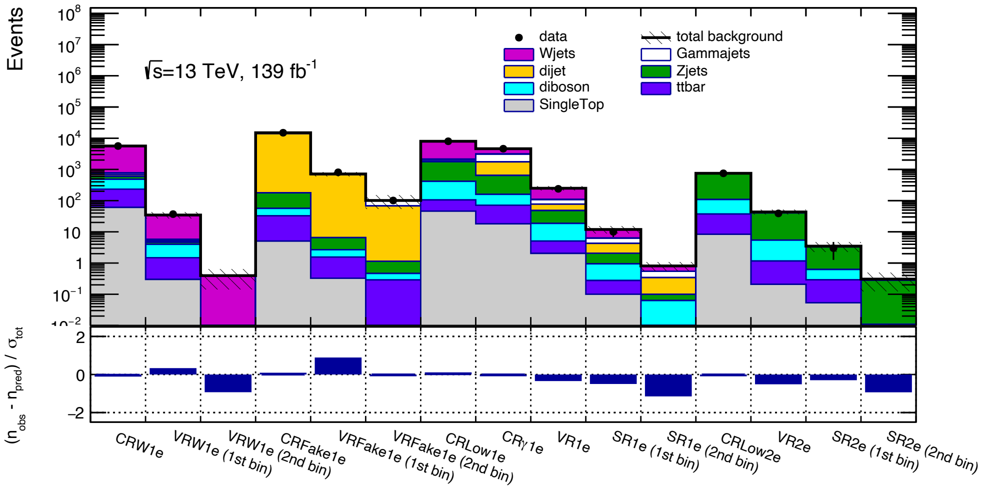

Figure 9.1: Data vs post-fit MC expectation of CR/VR/SR for electron channel. Bottom panel shows the difference between observed data and post-fit MC expectation divided by the total uncertainty σ_{tot}.

9.1.2 Muon final states

As discussed in Section 6.3, a background only fit to CRLow2mu with a full set of systematic uncertainties is performed to estimate a normalization factor for Z+jets. This normalization factor is then applied in heavier mass regions.

The post-fit yields in each region is shown in Table 9.5 with the number of events in data. The fitted normalization factor is 1.12 ± 0.18. The number of observed data in the first and second bin of SR2mu are 2 and 0, respectively. While the total fitted MC in them are 4.5 ± 1.9 and 0.8 ± 0.6, respectively. As shown in Figure 9.2, the MC reproduces the data very well in all regions. This result indicates no signal is found in the SR2mu.

Table 9.5: Results of background-only fit to CRLow2mu for integral luminosity of 139 fb^{-1}. The errors are statistical plus systematic uncertainties. Uncertainties on the fitted yields are symmetric by construction, where the negative error is truncated when reaching to zero event yield. "–" indicates exactly zero event is expected. The most bottom row shows the total pre-fit MC events.

channel	CRLow2mu	VR2mu	SR2mu (1st bin)	SR2mu (2nd bin)
Observed events	950	46	2	0
Fitted bkg events	950.2 ± 31.1	54.4 ± 10.9	4.5 ± 1.9	0.8 ± 0.6
Fitted Z+jets events	644.5 ± 102.9	38.1 ± 12.1	3.2 ± 1.9	0.6 ± 0.6
Fitted di-boson events	108.2 ± 54.3	6.7 ± 3.4	0.8 ± 0.4	0.1 ± 0.1
Fitted W+jets events	98.1 ± 52.3	4.7 ± 2.9	$0.2^{+0.2}_{-0.2}$	0.1 ± 0.1
Fitted $t\bar{t}$ events	78.0 ± 46.3	3.8 ± 2.2	–	–
Fitted single-top events	20.4 ± 12.0	0.9 ± 0.6	$0.3^{+0.3}_{-0.3}$	–
Fitted QCD multi-jet events	0.9 ± 0.5	0.2 ± 0.2	–	–
Fitted γ+jets events	–	–	–	–
Pre-fit background events	882.3	50.4	4.1	0.8

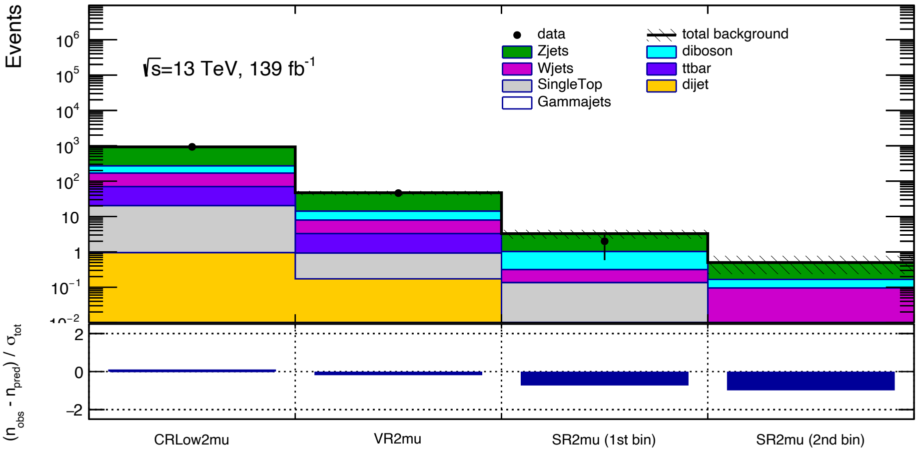

Figure 9.2: Data vs post-fit MC expectation of CR/VR/SR for muon channel. Bottom panel shows the ratio of difference between observed data and post-fit MC expectation divided by the total uncertainty σ_{tot}.

9.2 Upper limits on BSM events with model independent fits

In the background only fits described in the previous section, any SR is not convoluted in the likelihood function given in equation 7.1. Instead of such an approach, a single bin SR where the W_R mass is greater than 3 TeV is introduced to evaluate the number of possible BSM events using the p_0-value, called model-independent fit. The p_0-value is obtained with the background only hypothesis as explained in Section 7.2. Model-independent fits are performed to all three SRs and p_0-values for them are obtained to be 0.5. These results mean that the observed events are consistent with the background only hypothesis or the existence of the deficits. In this analysis, the deficits are observed as shown in Table 9.3, 9.4 and 9.5. No BSM events are found.

Then, the hypothesis tests for various μ_s are performed and Figure 9.3 shows CL_s, CL_b and CL_{s+b} described in Section 7.2. The upper limit of expected (observed) BSM events at p-value (CL_s) of 0.05 for expected (observed) events, where the expected (observed) line and horizontal line at 0.05 intersect in Figure 9.3, are expressed as S^{95}_{exp} (S^{95}_{obs}) in Table 9.6, respectively. The visible cross section, which is defined as the number of observed events divided by luminosity, are also shown in Table 9.6.

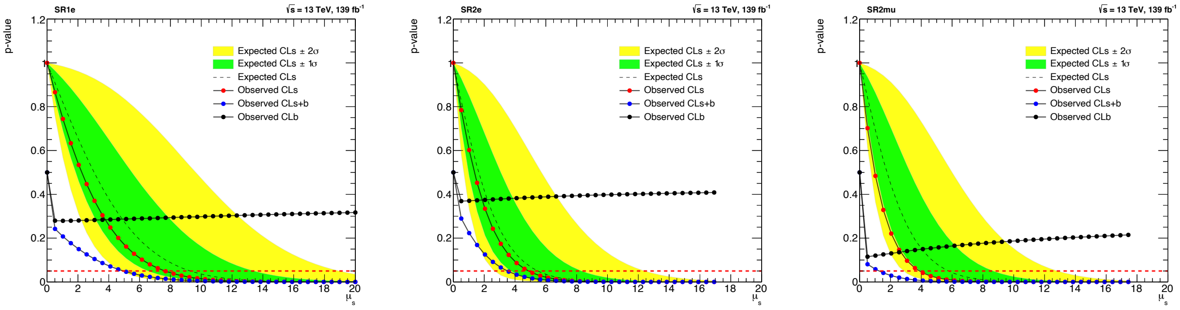

(a) One electron SR
(b) Two electron SR
(c) Two muon SR

Figure 9.3: Expected and observed CL_s (red), observed CL_{s+b} (blue), and observed CL_b (black) as a function of the signal strength μ_s for (a) one electron, (b) two electron and (c) two muon channel. The expected CL_s value with $\pm 1\sigma$ (green band) and $\pm 2\sigma$ (yellow band) are overlaid. The red horizontal lines indicate the p-value at 0.05.

Table 9.6: p_0-value, expected 95% CL upper limit on the number of BSM events (S^{95}_{exp}) with $\pm 1\sigma$ excursions, observed 95% CL upper limit on the number of BSM events (S^{95}_{obs}) and visible cross section for SR1e, SR2e and SR2mu.

Signal region	$p_0(\mu_s = 0)$	S^{95}_{exp}	S^{95}_{obs}	$\langle\epsilon\sigma\rangle^{95}_{\mathrm{obs}}$[fb]
SR1e	0.5	$9.3^{+4.1}_{-2.7}$	7.6	0.06
SR2e	0.5	$5.5^{+2.8}_{-1.8}$	4.9	0.04
SR2mu	0.5	$5.8^{+2.9}_{-1.8}$	3.9	0.03

9.3 Exclusion limits on signal events with model dependent fits

In order to determine whether a particular signal model is rejected at 95% confidence level, model dependent fits are performed. As explained in Section 1.3, the right-handed neutrinos are Majorana particles and

50% of signal events have same-sign lepton pairs, called Majorana scenario. The CR/SR definitions and the handling of the normalization factors are exactly the same as those for background-only fits discussed in Section 9.1, except that the multi-bins SRs are convoluted into the likelihood and a signal sample is included. The compatibility of the observed data with background-only or signal-plus-background hypothesis is checked using the CLs prescription as explained in Secion 7.2. The upper limit on the given cross section for various W_R and N_R hypothesis are obtained.

The excluded phase space in the two-dimensional plane of W_R and N_R masses obtained from the upper limits are shown in Figure 9.4. W_R mass is excluded up to 6.4 TeV for N_R mass at 1.0 TeV at the 95% confidence level for both electron and muon channels.

9.4 Discussion

9.4.1 Comparison to the other LHC results

Figures 9.5(a) and 9.5(b) show the comparisons between the results already published with the data delivered by LHC and the result of this analysis for the Majorana scenario. The exclusion limits are improved by 1.5 TeV and 1.4 TeV in heavier W_R mass for N_R mass at around 200 GeV compared to the previous publication with 80 $\mathrm{fb}^{-1}$by ATLAS [34] for electron and muon channels, respectively.

There are some reasons of these improvement except for the data increasement. The optimization of binning in SRs discussed in Section 5.5 improves the ratio of the number of signal events to the number of background in the highest W_R mass region. This enables to search for high-mass W_R signals which have small cross sections. Re-optimizations of two lepton channels improve the ratio of the number of signal events to the number of background. In addition, by adding SR1e for electron channel and deactivating the muon-jet overlap removal and any isolation requirement for the sub-leading muon for muon channel, the sensitivity is improved in the region of N_R mass below 100 GeV. This region is investigated for the first time in the ATLAS. This is a benefit of using large-R jets formed by combining small-R jets as explained in Section 4.11.

Since the LRSM model assumes that the neutrinos are Majorana particles, 50% of the signal events are generated to have same-sign lepton pairs and the other 50% to have opposite-sign lepton pairs. On the other hand, in case Dirac particles are considered, called Dirac scenario, all lepton pairs in the final state are opposite-sign. The exclusion limits for the Dirac scenario by using the exactly same analytical methods as the Majorana scenario are evaluated by selecting only events with a lepton pair of opposite-sign in the truth level for signal samples and doubling the cross section as shown in Figures 9.5(c) and 9.5(d). W_R mass is excluded up to 6.4 TeV for N_R mass at 1.0 TeV at the 95 % confidence level for both electron and muon channel. The exclusion limits are improved by 1.7 TeV and 1.6 TeV at N_R mass of 500 GeV comparing to the previous publication with 36 $\mathrm{fb}^{-1}$by ATLAS [34] for electron and muon channel, respectively. Interpretations of Dirac scenario were not done in the previous ATLAS boosted [34] and latest CMS analyses [38]. These comparisons clearly show that the exclusion limits set by this analysis gives the best sensitivities in most of the phase space.

9.4.2 Comparison to the non-LHC experiments

Figure 9.6 shows the observed upper limits in the region with $m(N_\mathrm{R}) < 1000$ GeV. In that region, the exclusion limit of this analysis is almost independent of $m(W_\mathrm{R})$ and up to roughly $m(W_\mathrm{R}) = 6.2$ TeV is excluded. Compared to the results obtained in the non-LHC experiments, the most stringent limits are obtained with respect to the $m(W_\mathrm{R})$ except in the region of $m(N_\mathrm{R}) < 50$ GeV where N_R is less likely to decay to the off-shell W_R. Even in comparison with the expected results that would be obtained with ILC, more restrict limit is obtained in the most phase space.

9.4.3 Cross section and coupling constant upper limits

The upper limits on the product of the cross section for W_R production from proton collision, $\sigma(pp \to W_\mathrm{R})$, and the branching fractions, $B(W_\mathrm{R} \to \ell\ell q\bar{q}')$, for given $m(N_\mathrm{R})$ hypothesis are scanned with respect to the $m(W_\mathrm{R})$. The upper limits are visualized in Figure 9.7 for $m(N_\mathrm{R}) = 50$ GeV and 1 TeV with the results by ATLAS dijet resonance search with 139 fb^{-1} [113]. The cross section upper limit in dijet resonance is scaled by multiplying $B(W_\mathrm{R} \to \ell\ell q\bar{q}')$ over $B(W_\mathrm{R} \to q\bar{q}')$ by taking into account the unitarity of the mixing matrix for right-handed particles. The $m(W_\mathrm{R})$ where the observed limit and theoretical cross section intersect corresponds to the maximum exclusion limit for a given $m(N_\mathrm{R})$ at 95% CL. Comparing to the dijet resonance results, restrictions with heavier W_R mass of about 1.0 to 1.5 TeV are observed depending on the N_R mass.

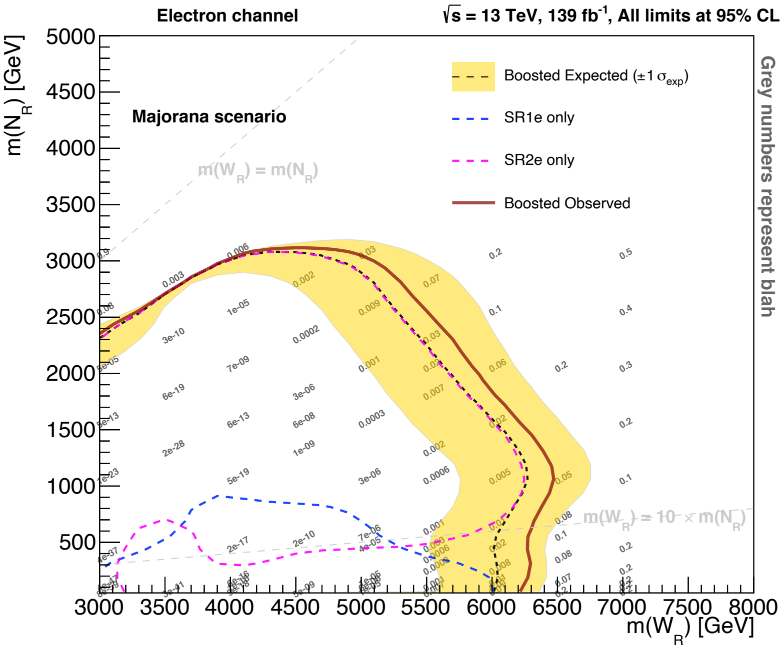

(a) Electron channel

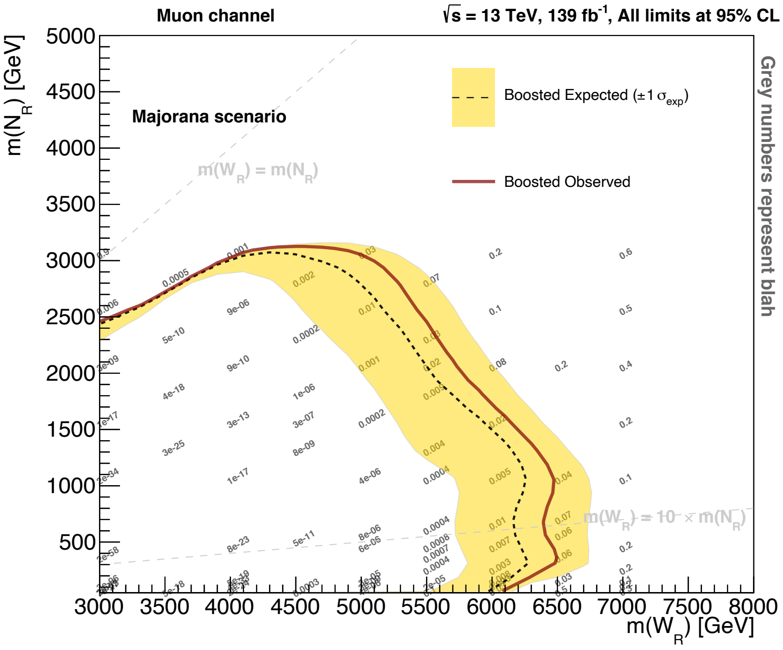

(b) Muon channel

Figure 9.4: The expected and observed 95 % CL upper limits: (a) electron channel. (b) muon channel. Black, blue and pink dashed lines represent the expected CL upper limits for combined expected, SR1e only and SR2e only, respectively. Dark red solid line represents the observed CL upper limit. Yellow band represents the one standard-deviation of the expected limit. Each gray number shows the CLs value for each signal mass point.

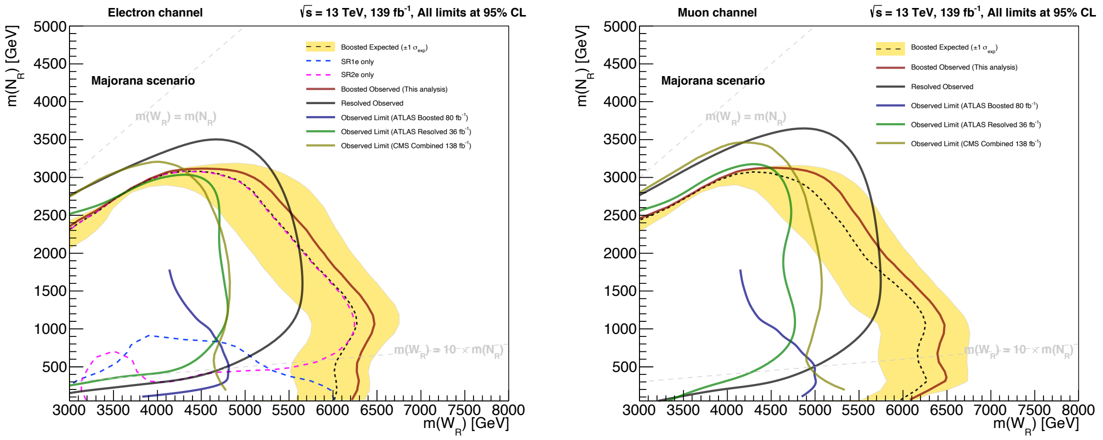

(a) Majorana electron neutrino

(b) Majorana muon neutrino

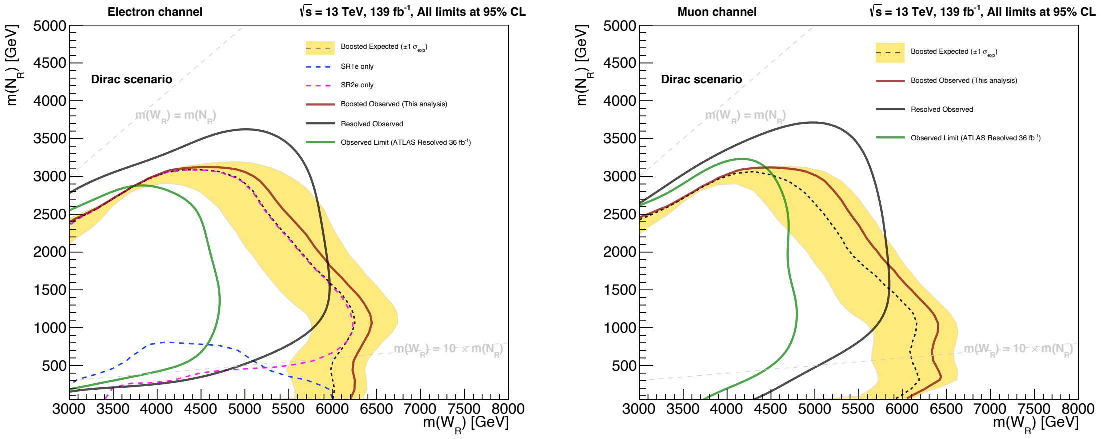

(c) Dirac electron neutrino

(d) Dirac muon neutrino

Figure 9.5: The expected and observed 95 % CL upper limits: (a) Majorana electron neutrino scenario. (c) Dirac electron scenario. (b) Majorana muon neutrino scenario. (d) for Dirac muon neutrino scenario. Black, blue and pink dashed lines represent the expected CL upper limits for combined expected, SR1e only and SR2e only, respectively. Yellow band represents the one standard-deviation of the expected limit. Red, black, yellow, green and blue solid lines represent the observed CL upper limits for this analysis, ATLAS resolved analysis with 139 fb^{-1} [112], CMS analysis [38] with 138 fb^{-1}, ATLAS resolved analysis [33] with 36 fb^{-1}and the ATLAS boosted analysis [34] with 80 fb^{-1}, respectively.

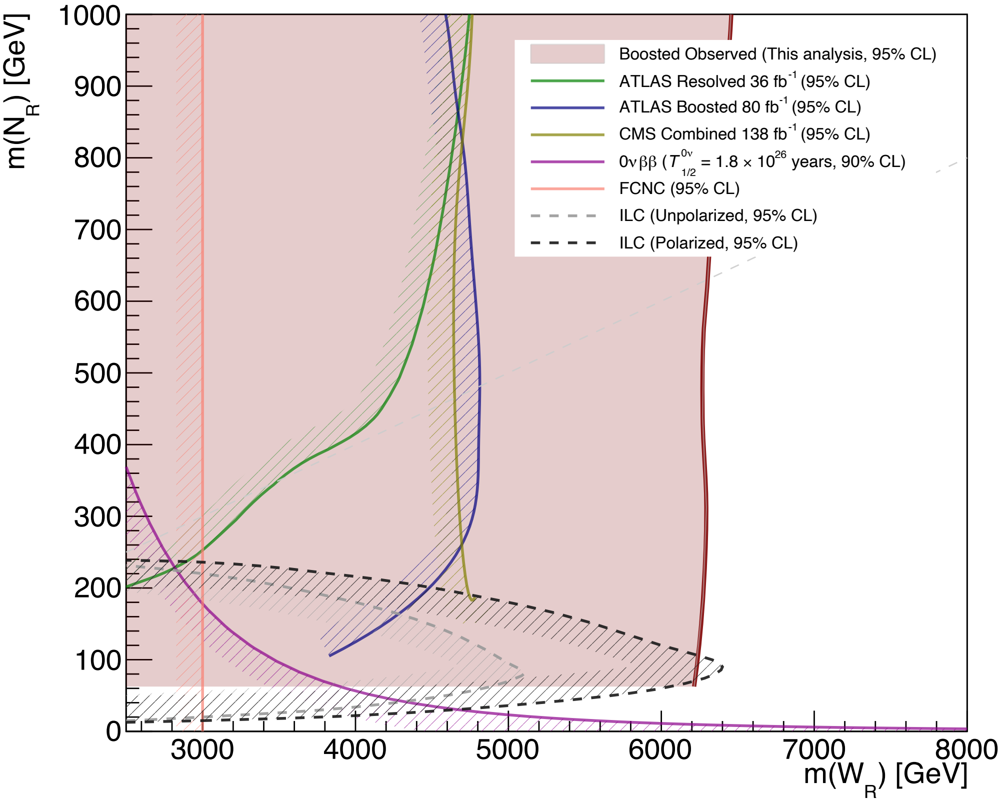

Figure 9.6: Observed and expected exclusion region in W_R mass and N_R mass plane. Sold dark red line represents the observed 95% CL limit of this analysis. Black and gray exclusion lines represent the expected results from ILC with and without the initial beam polarization at $\sqrt{s}$ = 500 GeV [46], respectively. 90% exclusion from the neutrino less double beta decay [41] and 95% exclusion from the meson mixing [39] are shown as purple and pale red lines, respectively. 95% exclusion with ATLAS resolved analysis with 36 fb^{-1} [33], ATLAS boosted analysis with 80 fb^{-1} [34] and CMS analysis with 138 fb^{-1} [38] are shown as green, blue and dark yellow lines, respectively.

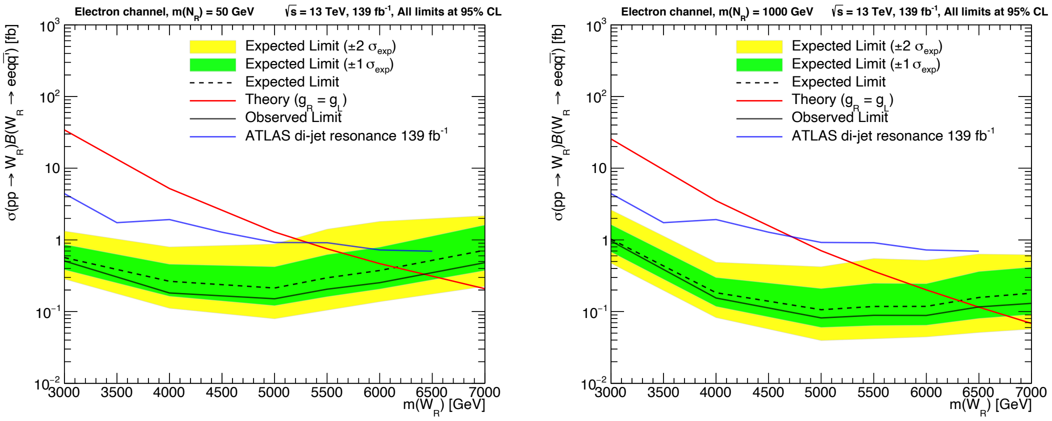

(a) Electron channel, $m(N_\mathrm{R}) = 50$ GeV

(b) Electron channel, $m(N_\mathrm{R}) = 1000$ GeV

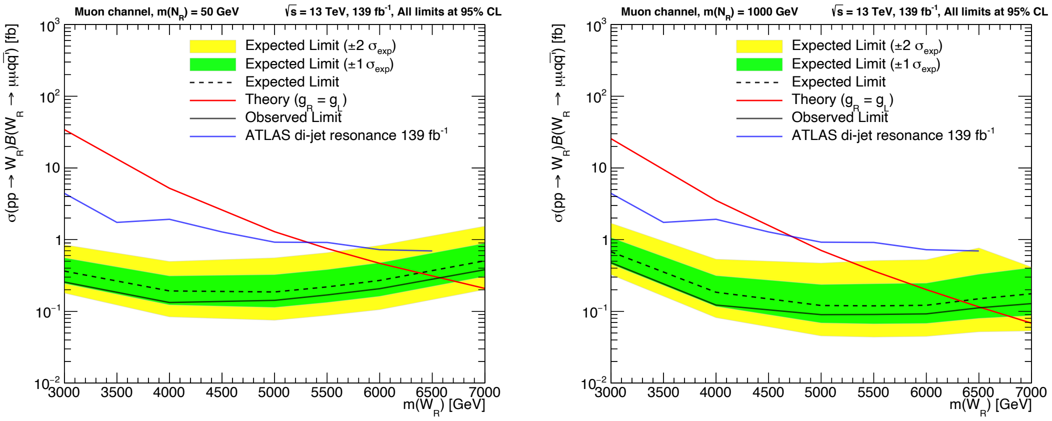

(c) Muon channel, $m(N_\mathrm{R}) = 50$ GeV

(d) Muon channel, $m(N_\mathrm{R}) = 1000$ GeV

Figure 9.7: Upper limits for the cross section of $pp \to W_\mathrm{R} \to \ell\ell qq'$ for (a) shows the limit for $m(N_\mathrm{R}) = 50$ GeV in the electron final state, (b) shows the limit for $m(N_\mathrm{R}) = 1000$ GeV in the electron final state, (c) shows the limit for $m(N_\mathrm{R}) = 50$ GeV in the muon final state, and (d) shows the limit for $m(N_\mathrm{R}) = 1000$ GeV in the muon final state. Red bold, black bold and black dashed lines denote theoretical cross section, observed cross section upper limit and expected cross section upper limit, respectively. Observed cross section limits of ATLAS dijet resonance search with 139fb^{-1} [113] are also displayed as blue sold lines. Yellow and green bands indicate the 1 σ and 2 σ coverage of the expected upper limits.

10 Conclusion

This thesis has been presented a search for right-handed neutrino N_R and right-handed W boson W_R in final states with two same flavour leptons and a large-R jet using proton-proton collisions at $\sqrt{s} = 13$ TeV with the ATLAS detector. The data is collected in 2015-2018 corresponding to the integrated luminosity of 139 fb^{-1}.

To extend the searchable region, event selections are re-optimized from the previous analysis. Furthermore, for electron channel, a new signal region requiring exactly one electron is introduced to cover lower N_R mass region. Two different SRs are orthogonal between each other and they are statistically combined to evaluate final sensitivities. For muon channel, the object selection and overlap removal are optimized as well. The sub-leading muon from N_R decay is not required to pass any isolation criteria and overlap removal with jets is deactivated.

The background estimation methods have been developed to estimate dominant backgrounds by preparing dedicated control regions. Extrapolations from CRs to SRs are validated by using regions with similar phase spaces, called extra VRs, for each background. The post-fit results reasonably agree with observed data in all extra VRs showing the methods work well. Finally, the search for the signal has been performed and the observed data is consistent with the post-fit background yield within one standard deviation. No excess is observed in the all signal regions.

No excess is observed in every signal regions. Hence, the exclusion limits are set. In the scenario where the neutrinos are Majorana particles, W_R mass is excluded up to 6.4 TeV at the N_R mass of 1.0 TeV for both electron and muon channels. Compared to the previous results, it corresponds to the expansion of exclusion limits by 1.5 TeV and 1.4 TeV for electron and muon channels, respectively. The exclusion limits for Dirac particle scenario are also evaluated and it is observed that the exclusion power is comparable to that of the Majorana particles. In addition, the search sensitivity is successfully extended to N_R mass below 100 GeV for the first time in the ATLAS experiment.

Acknowledgements

I have received a lot of advice and help from many people during the course of this research. First, I am very grateful to my advisor, Prof. Junichi Tanaka, for not only supporting my research but also helping me to continue my life at CERN. I am also very grateful to Dr. Takuya Nobe for not only giving me many attentive supports at every step of research processes but also providing me with a lot of supports to make living at CREN a pleasant experience. I want to express my gratitude to Dr. Yuji Enari, Dr. Yasukuki Okumura, Dr. Koji Terashi, Dr. Tatuya Mashbuchi, Dr. Ryu Sawada, Dr. Tomoyuki Saito, Prof. Masaya Ishino, Dr. Saito Masahiko, Dr. Morinaga Masahiro, and Dr. Ryu Sawada not only provided important comments and suggestions at the analysis meetings, but also helped me by correcting my slides and practicing my presentation for the conference, which enabled me to proceed with the analysis in the right direction.

Dr. Matthias Saimpert, Dr. Merve Nazlim Agaras, Dr. Flavia de Almeida Dias, and Dr. Tamara Vazquez Schroeder led the analysis in ATLAS and provided many comments at group and sub-group meetings.

I would also like to thank the members of the analysis group, Dr. Neofytos Themistokleous, Dr. Benjamin Michael Wynne, Dr. Christos Lepnodopoulos, and Dr. Edson Carquin Leopez, who were very helpful in our weekly discussions. I would like to thank them all.

I am grateful to Dr. Shion Chen, Dr. Tomoya Iizawa, Dr. Tomohiro Inada, Dr. Maeda Junpei, and many students who spent their research lift with me for their help during my stay at CERN, which has been a very comfortable experience.

I would also like to thank the ICEPP secretaries for all the administrative work they did for me, including travel arrangements to CERN, which allowed me to concentrate on my research. Finally, I would like to thank my family for their constant support even though I was far away from my hometown, and for their continuous support in everything I did. Thanks to many people, I was able to make the most of my three years in the doctoral program.

Bibliography

[1] M. K. Gaillard, P. D. Grannis and F. J. Sciulli, *The standard model of particle physics*, Reviews of Modern Physics **71** (1999) S96, ISSN: 1539-0756, URL: `http://dx.doi.org/10.1103/RevModPhys.71.S96` (cit. on p. 7).

[2] *TEXample.net, Standard model of physics*, URL: `http://www.texample.net/tikz/examples/model-physics/` (cit. on p. 7).

[3] S. L. Glashow, *Partial-symmetries of weak interactions*, Nuclear Physics **22** (1961) 579, ISSN: 0029-5582, URL: `https://www.sciencedirect.com/science/article/pii/0029558261904692` (cit. on p. 9).

[4] S. Weinberg, *A Model of Leptons*, Phys. Rev. Lett. **19** (21 1967) 1264, URL: `https://link.aps.org/doi/10.1103/PhysRevLett.19.1264` (cit. on p. 9).

[5] A. Salam, *Weak and Electromagnetic Interactions*, Conf. Proc. C **680519** (1968) 367 (cit. on pp. 9, 13).

[6] Y. e. a. Fukuda, *Evidence for Oscillation of Atmospheric Neutrinos*, Phys. Rev. Lett. **81** (8 1998) 1562, URL: `https://link.aps.org/doi/10.1103/PhysRevLett.81.1562` (cit. on p. 15).

[7] Q. R. e. a. Ahmad, *Measurement of the Rate of $\nu_e + d \longrightarrow p + p + e^-$ Interactions Produced by ^8B Solar Neutrinos at the Sudbury Neutrino Observatory*, Phys. Rev. Lett. **87** (7 2001) 071301, URL: `https://link.aps.org/doi/10.1103/PhysRevLett.87.071301` (cit. on p. 15).

[8] B. Pontecorvo, *Electron and Muon Neutrinos*, Zh. Eksp. Teor. Fiz. **37** (1959) 1751 (cit. on p. 15).

[9] Z. Maki, M. Nakagawa and S. Sakata, *Remarks on the Unified Model of Elementary Particles*, Progress of Theoretical Physics **28** (1962) 870, ISSN: 0033-068X, eprint: `https://academic.oup.com/ptp/article-pdf/28/5/870/5258750/28-5-870.pdf`, URL: `https://doi.org/10.1143/PTP.28.870` (cit. on p. 15).

[10] *Violation of CP invariance, C asymmetry, and baryon asymmetry of the universe*, Journal of Experimental and Theoretical Physics Letters (1967) 24 (cit. on p. 16).

[11] V. Kuzmin, V. Rubakov and M. Shaposhnikov, *On anomalous electroweak baryon-number non-conservation in the early universe*, Physics Letters B **155** (1985) 36, ISSN: 0370-2693, URL: `https://www.sciencedirect.com/science/article/pii/0370269385910287` (cit. on p. 17).

[12] V. Kuzmin, V. Rubakov and M. Shaposhnikov, *Anomalous electronweak baryon number non-conservation and GUT mechanism for baryogenesis*, Physics Letters B **191** (1987) 171, ISSN: 0370-2693, URL: `https://www.sciencedirect.com/science/article/pii/0370269387913402` (cit. on p. 17).

[13] *The Statistical Theory of Anomalous Fermion Number Nonconservation*, Nuclear Physics B **308** (1988) 885 (cit. on p. 17).

[14] F. R. Klinkhamer and N. S. Manton, *A saddle-point solution in the Weinberg-Salam theory*, Phys. Rev. D **30** (10 1984) 2212, URL: `https://link.aps.org/doi/10.1103/PhysRevD.30.2212` (cit. on p. 18).

[15] P. Minkowski, *$\mu \to e\gamma$ at a rate of one out of 109 muon decays?*, Physics Letters B **67** (1977) 421, ISSN: 0370-2693, URL: `https://www.sciencedirect.com/science/article/pii/037026937790435X` (cit. on pp. 18, 19).

[16] T. Yanagida, *Horizontal Symmetry and Masses of Neutrinos*, Progress of Theoretical Physics **64** (1980) 1103, ISSN: 0033-068X, eprint: `https://academic.oup.com/ptp/article-pdf/64/3/1103/5394376/64-3-1103.pdf`, URL: `https://doi.org/10.1143/PTP.64.1103` (cit. on p. 18).

[17] R. N. Mohapatra and G. Senjanovi ć, *Neutrino Mass and Spontaneous Parity Nonconservation*, Phys. Rev. Lett. **44** (14 1980) 912, URL: `https://link.aps.org/doi/10.1103/PhysRevLett.44.912` (cit. on pp. 18, 19).

[18] T. P. Cheng and L.-F. Li, *Neutrino masses, mixings, and oscillations in SU(2)×U(1) models of electroweak interactions*, Phys. Rev. D **22** (11 1980) 2860, URL: `https://link.aps.org/doi/10.1103/PhysRevD.22.2860` (cit. on p. 18).

[19] J. Schechter and J. W. F. Valle, *Neutrino masses in SU(2) $\bigotimes$ U(1) theories*, Phys. Rev. D **22** (9 1980) 2227, URL: `https://link.aps.org/doi/10.1103/PhysRevD.22.2227` (cit. on p. 18).

[20] R. Foot, H. Lew, X. G. He and G. C. Joshi, *Seesaw Neutrino Masses Induced by a Triplet of Leptons*, Z. Phys. C **44** (1989) 441 (cit. on p. 18).

[21] M. Fukugita and T. Yanagida, *Baryogenesis Without Grand Unification*, Phys. Lett. B **174** (1986) 45 (cit. on p. 19).

[22] J. C. Pati and A. Salam, *Lepton number as the fourth "color"*, Phys. Rev. D **10** (1 1974) 275, URL: `https://link.aps.org/doi/10.1103/PhysRevD.10.275` (cit. on p. 19).

[23] R. N. Mohapatra and J. C. Pati, *Left-right gauge symmetry and an "isoconjugate" model of* CP *violation*, Phys. Rev. D **11** (3 1975) 566, URL: `https://link.aps.org/doi/10.1103/PhysRevD.11.566` (cit. on p. 19).

[24] G. Senjanovic and R. N. Mohapatra, *Exact left-right symmetry and spontaneous violation of parity*, Phys. Rev. D **12** (5 1975) 1502, URL: `https://link.aps.org/doi/10.1103/PhysRevD.12.1502` (cit. on p. 19).

[25] R. N. Mohapatra and J. C. Pati, *A Natural Left-Right Symmetry*, Phys. Rev. D **11** (1975) 2558 (cit. on p. 19).

[26] G. Senjanovic, *Spontaneous Breakdown of Parity in a Class of Gauge Theories*, Nucl. Phys. B **153** (1979) 334 (cit. on p. 19).

[27] R. Marshak and R. Mohapatra,
Quark-lepton symmetry and B - L as the U(1) generator of the electroweak symmetry group,
Physics Letters B **91** (1980) 222, ISSN: 0370-2693,
URL: `https://www.sciencedirect.com/science/article/pii/0370269380904360`
(cit. on p. 19).

[28] R. N. Mohapatra and R. E. Marshak,
Local B-L Symmetry of Electroweak Interactions, Majorana Neutrinos and Neutron Oscillations,
Phys. Rev. Lett. **44** (1980) 1316, [Erratum: Phys.Rev.Lett. 44, 1643 (1980)] (cit. on p. 19).

[29] R. N. Mohapatra and G. Senjanovi ć,
Neutrino masses and mixings in gauge models with spontaneous parity violation,
Phys. Rev. D **23** (1 1981) 165,
URL: `https://link.aps.org/doi/10.1103/PhysRevD.23.165` (cit. on pp. 19, 20).

[30] A. Maiezza, M. Nemev šek, F. Nesti and G. Senjanovi ć, *Left-right symmetry at LHC*,
Phys. Rev. D **82** (5 2010) 055022,
URL: `https://link.aps.org/doi/10.1103/PhysRevD.82.055022` (cit. on p. 20).

[31] *Majorana neutrinos and the production of the right-handed charged gauge boson*,
Physical Review Letters **50** (1983) 1427, ISSN: 00319007,
URL: `http://link.aps.org/doi/10.1103/PhysRevLett.50.1427` (cit. on pp. 20, 21).

[32] ATLAS Collaboration,
Search for heavy Majorana neutrinos with the ATLAS detector in pp collisions at $\sqrt{s} = 8$ TeV,
JHEP **07** (2015) 162, arXiv: `1506.06020 [hep-ex]` (cit. on p. 21).

[33] ATLAS Collaboration,
Search for heavy Majorana or Dirac neutrinos and right-handed W gauge bosons in final states with two charged leptons and two jets at $\sqrt{s} = 13$ TeV with the ATLAS detector,
JHEP **01** (2019) 016, arXiv: `1809.11105 [hep-ex]` (cit. on pp. 21, 24, 100, 101).

[34] ATLAS Collaboration, *Search for a right-handed gauge boson decaying into a high-momentum heavy neutrino and a charged lepton in pp collisions with the ATLAS detector at $\sqrt{s} = 13$ TeV*,
Phys. Lett. B **798** (2019) 134942, arXiv: `1904.12679 [hep-ex]`
(cit. on pp. 21, 22, 24, 97, 100, 101).

[35] CMS Collaboration, *Search for heavy neutrinos and W_R bosons with right-handed couplings in a left-right symmetric model in pp collisions at $\sqrt{s} = 7$ TeV*, Phys. Rev. Lett. **109** (2012) 261802,
arXiv: `1210.2402 [hep-ex]` (cit. on p. 21).

[36] CMS Collaboration, *Search for a heavy right-handed W boson and a heavy neutrino in events with two same-flavor leptons and two jets at $\sqrt{s} = 13$ TeV*, JHEP **05** (2018) 148,
arXiv: `1803.11116 [hep-ex]` (cit. on p. 21).

[37] CMS Collaboration, *Search for heavy Majorana neutrinos in same-sign dilepton channels in proton–proton collisions at $\sqrt{s} = 13$ TeV*, JHEP **01** (2019) 122, arXiv: `1806.10905 [hep-ex]`
(cit. on p. 21).

[38] CMS Collaboration, *Search for a right-handed W boson and a heavy neutrino in proton–proton collisions at $\sqrt{s} = 13$ TeV*, JHEP **04** (2021) 047, arXiv: `2112.03949 [hep-ex]`
(cit. on pp. 21, 22, 24, 97, 100, 101).

[39] S. Bertolini, A. Maiezza and F. Nesti, *Present and Future K and B Meson Mixing Constraints on TeV Scale Left-Right Symmetry*, Phys. Rev. D **89** (2014) 095028, arXiv: `1403.7112 [hep-ph]` (cit. on pp. 23, 24, 101).

[40] J. Barry and W. Rodejohann, *Lepton number and flavour violation in TeV-scale left-right symmetric theories with large left-right mixing*, JHEP **09** (2013) 153, arXiv: `1303.6324 [hep-ph]` (cit. on p. 23).

[41] M. Agostini et al., *Final Results of GERDA on the Search for Neutrinoless Double-β Decay*, Phys. Rev. Lett. **125** (25 2020) 252502, URL: `https://link.aps.org/doi/10.1103/PhysRevLett.125.252502` (cit. on pp. 23, 24, 101).

[42] O. Azzolini et al., *Final Result on the Neutrinoless Double Beta Decay of* ^{82}Se *with CUPID-0*, Phys. Rev. Lett. **129** (11 2022) 111801, URL: `https://link.aps.org/doi/10.1103/PhysRevLett.129.111801` (cit. on p. 23).

[43] D. Q. Adams et al., *Improved Limit on Neutrinoless Double-Beta Decay in* ^{130}Te *with CUORE*, Phys. Rev. Lett. **124** (12 2020) 122501, URL: `https://link.aps.org/doi/10.1103/PhysRevLett.124.122501` (cit. on p. 23).

[44] A. Gando et al., *Search for Majorana Neutrinos Near the Inverted Mass Hierarchy Region with KamLAND-Zen*, Phys. Rev. Lett. **117** (8 2016) 082503, URL: `https://link.aps.org/doi/10.1103/PhysRevLett.117.082503` (cit. on p. 23).

[45] G. Anton et al., *Search for Neutrinoless Double-β Decay with the Complete EXO-200 Dataset*, Phys. Rev. Lett. **123** (16 2019) 161802, URL: `https://link.aps.org/doi/10.1103/PhysRevLett.123.161802` (cit. on p. 23).

[46] Sudhansu S. Biswal and P. S. Bhupal Dev, *Probing Left-Right Seesaw using Beam Polarization at ee Collider*, Phys. Rev. D (2017), arXiv: `1701.08751v1 [hep-ph]` (cit. on pp. 23, 24, 101).

[47] L. Evans and P. Bryant, *LHC Machine*, Journal of Instrumentation **3** (2008) S08001, URL: `https://doi.org/10.1088/1748-0221/3/08/s08001` (cit. on p. 26).

[48] E. Mobs, *The CERN accelerator complex - August 2018. Complexe des accélérateurs du CERN - Août 2018*, (2018), General Photo, URL: `http://cds.cern.ch/record/2636343` (cit. on p. 26).

[49] T. A. Collaboration, *The ATLAS Experiment at the CERN Large Hadron Collider*, Journal of Instrumentation **3** (2008) S08003, URL: `https://doi.org/10.1088/1748-0221/3/08/s08003` (cit. on pp. 27, 28).

[50] T. C. Collaboration, *The CMS experiment at the CERN LHC*, Journal of Instrumentation **3** (2008) S08004, URL: `https://doi.org/10.1088/1748-0221/3/08/s08004` (cit. on p. 27).

[51] T. A. Collaboration, *The ALICE experiment at the CERN LHC*, Journal of Instrumentation **3** (2008) S08002, URL: `https://doi.org/10.1088/1748-0221/3/08/s08002` (cit. on p. 27).

[52] T. L. Collaboration, *The LHCb Detector at the LHC*, Journal of Instrumentation **3** (2008) S08005, URL: `https://doi.org/10.1088/1748-0221/3/08/s08005` (cit. on p. 27).

[53] G. Avoni et al., *The new LUCID-2 detector for luminosity measurement and monitoring in ATLAS*, Journal of Instrumentation **13** (2018) P07017 (cit. on pp. 27, 29, 76).

[54] ATLAS Collaboration,
ATLAS Central Solenoid: Magnet Project Technical Design Report, Volume 4,
ATLAS-TDR-9; CERN-LHCC-97-021, CERN, 1997,
URL: `https://cds.cern.ch/record/331067` (cit. on pp. 29, 30).

[55] ATLAS Collaboration, *ATLAS Inner Detector: Technical Design Report, Volume 2*, ATLAS-TDR-5, CERN-LHCC-97-017, 1997, URL: `https://cds.cern.ch/record/331064` (cit. on pp. 29, 31).

[56] ATLAS Collaboration, *ATLAS Liquid Argon Calorimeter: Technical Design Report*, ATLAS-TDR-2; CERN-LHCC-96-041, 1996, URL: `https://cds.cern.ch/record/331061` (cit. on p. 30).

[57] ATLAS Collaboration, *ATLAS Tile Calorimeter: Technical Design Report*, ATLAS-TDR-3; CERN-LHCC-96-042, 1996, URL: `https://cds.cern.ch/record/331062` (cit. on pp. 30, 32).

[58] C. W. Fabjan and F. Gianotti, *Calorimetry for particle physics*, Rev. Mod. Phys. **75** (2003) 1243 (cit. on pp. 30, 31).

[59] ATLAS Collaboration, *ATLAS Muon Spectrometer: Technical Design Report*,
ATLAS-TDR-10; CERN-LHCC-97-022, CERN, 1997,
URL: `https://cds.cern.ch/record/331068` (cit. on pp. 32, 33).

[60] ATLAS Collaboration, *ATLAS Level-1 Trigger: Technical Design Report*, ATLAS-TDR-12; CERN-LHCC-98-014, 1998, URL: `https://cds.cern.ch/record/381429` (cit. on p. 33).

[61] ATLAS Collaboration, *2015 start-up trigger menu and initial performance assessment of the ATLAS trigger using Run-2 data*, ATL-DAQ-PUB-2016-001, 2016,
URL: `https://cds.cern.ch/record/2136007` (cit. on p. 33).

[62] ATLAS Collaboration, *Trigger Menu in 2016*, ATL-DAQ-PUB-2017-001, 2017,
URL: `https://cds.cern.ch/record/2242069` (cit. on p. 33).

[63] ATLAS Collaboration, *Trigger Menu in 2017*, ATL-DAQ-PUB-2018-002, 2018,
URL: `https://cds.cern.ch/record/2625986` (cit. on p. 33).

[64] ATLAS Collaboration, *Trigger Menu in 2018*, ATL-DAQ-PUB-2019-001, 2019,
URL: `https://cds.cern.ch/record/2693402` (cit. on p. 33).

[65] ATLAS Collaboration,
Luminosity determination in pp collisions at $\sqrt{s} = 13$ TeV using the ATLAS detector at the LHC,
ATLAS-CONF-2019-021, 2019, URL: `https://cds.cern.ch/record/2677054` (cit. on p. 34).

[66] ATLAS Collaboration,
ATLAS data quality operations and performance for 2015–2018 data-taking,
JINST **15** (2020) P04003, arXiv: `1911.04632 [physics.ins-det]` (cit. on p. 35).

[67] S. Agostinelli et al., *GEANT4–a simulation toolkit*, Nucl. Instrum. Meth. A **506** (2003) 250 (cit. on p. 35).

[68] W. Buttinger, *Using Event Weights to account for differences in Instantaneous Luminosity and Trigger Prescale in Monte Carlo and Data*, tech. rep., CERN, 2015,
URL: `https://cds.cern.ch/record/2014726` (cit. on pp. 35, 76).

[69] G. Altarelli and G. Parisi, *Asymptotic freedom in parton language*, Nuclear Physics B **126** (1977) 298, ISSN: 0550-3213, URL: `https://www.sciencedirect.com/science/article/pii/0550321377903844` (cit. on p. 36).

[70] Y. L. Dokshitzer, *Calculation of the Structure Functions for Deep Inelastic Scattering and e+ e- Annihilation by Perturbation Theory in Quantum Chromodynamics.*, Sov. Phys. JETP **46** (1977) 641 (cit. on p. 36).

[71] V. N. Gribov and L. N. Lipatov, *Deep inelastic e p scattering in perturbation theory*, Sov. J. Nucl. Phys. **15** (1972) 438 (cit. on p. 36).

[72] J. Alwall et al., *The automated computation of tree-level and next-to-leading order differential cross sections, and their matching to parton shower simulations*, JHEP **07** (2014) 079, arXiv: `1405.0301 [hep-ph]` (cit. on p. 36).

[73] A. Alloul, N. D. Christensen, C. Degrande, C. Duhr and B. Fuks, *FeynRules 2.0 - A complete toolbox for tree-level phenomenology*, Comput. Phys. Commun. **185** (2014) 2250, arXiv: `1310.1921 [hep-ph]` (cit. on p. 36).

[74] T. Sjostrand, S. Mrenna and P. Z. Skands, *A Brief Introduction to PYTHIA 8.1*, Comput. Phys. Commun. **178** (2008) 852, arXiv: `0710.3820 [hep-ph]` (cit. on p. 36).

[75] ATLAS Collaboration, *ATLAS Pythia 8 tunes to* 7 *TeV data*, ATL-PHYS-PUB-2014-021, 2014, URL: `https://cds.cern.ch/record/1966419` (cit. on p. 36).

[76] R. D. Ball et al., *Parton distributions for the LHC Run II*, JHEP **04** (2015) 040, arXiv: `1410.8849 [hep-ph]` (cit. on pp. 36, 38).

[77] R. D. Ball et al., *Parton distributions with LHC data*, Nuclear Physics B **867** (2013) 244, ISSN: 0550-3213, URL: `https://www.sciencedirect.com/science/article/pii/S0550321312005500` (cit. on p. 36).

[78] E. Bothmann et al., *Event Generation with Sherpa 2.2*, SciPost Phys. **7** (2019) 034, arXiv: `1905.09127 [hep-ph]` (cit. on pp. 37, 38).

[79] T. Gleisberg and S. Höche, *Comix, a new matrix element generator*, Journal of High Energy Physics **2008** (2008) 039, URL: `https://doi.org/10.1088/1126-6708/2008/12/039` (cit. on p. 37).

[80] F. Cascioli, P. Maierhöfer and S. Pozzorini, *Scattering Amplitudes with Open Loops*, Phys. Rev. Lett. **108** (11 2012) 111601, URL: `https://link.aps.org/doi/10.1103/PhysRevLett.108.111601` (cit. on p. 37).

[81] S. Schumann and F. Krauss, *A parton shower algorithm based on Catani-Seymour dipole factorisation*, Journal of High Energy Physics **2008** (2008) 038, URL: `https://doi.org/10.1088/1126-6708/2008/03/038` (cit. on p. 37).

[82] T. Sjöstrand, S. Mrenna and P. Skands, *A brief introduction to PYTHIA 8.1*, Computer Physics Communications **178** (2008) 852, ISSN: 0010-4655, URL: `https://www.sciencedirect.com/science/article/pii/S0010465508000441` (cit. on pp. 37, 38).

[83] R. D. Ball et al., *Parton distributions with LHC data*, Nucl. Phys. B **867** (2013) 244, arXiv: `1207.1303 [hep-ph]` (cit. on p. 37).

[84] S. Frixione, E. Laenen, P. Motylinski and B. R. Webber, *Angular correlations of lepton pairs from vector boson and top quark decays in Monte Carlo simulations*, Journal of High Energy Physics **2007** (2007) 081, URL: `https://doi.org/10.1088/1126-6708/2007/04/081` (cit. on p. 38).

[85] P. Nason, *A New Method for Combining NLO QCD with Shower Monte Carlo Algorithms*, Journal of High Energy Physics **2004** (2004) 040, URL: `https://doi.org/10.1088/1126-6708/2004/11/040` (cit. on p. 38).

[86] A.-K. Kashani-Poor, *Nearly Kähler reduction*, Journal of High Energy Physics **2007** (2007) 026, URL: `https://doi.org/10.1088/1126-6708/2007/11/026` (cit. on p. 38).

[87] C. Oleari, *The POWHEG BOX*, Nuclear Physics B - Proceedings Supplements **205-206** (2010) 36, Loops and Legs in Quantum Field Theory, ISSN: 0920-5632, URL: `https://www.sciencedirect.com/science/article/pii/S0920563210001994` (cit. on p. 38).

[88] P. Artoisenet, R. Frederix, O. Mattelaer and R. Rietkerk, *Automatic spin-entangled decays of heavy resonances in Monte Carlo simulations*, JHEP **03** (2013) 015. 17 p, Comments: 17 pages, 6 figures, arXiv: `1212.3460`, URL: `https://cds.cern.ch/record/1503431` (cit. on p. 38).

[89] F. Siegert, *A practical guide to event generation for prompt photon production with Sherpa*, Journal of Physics G: Nuclear and Particle Physics **44** (2017) 044007, URL: `https://doi.org/10.1088/1361-6471/aa5f29` (cit. on p. 38).

[90] ATLAS Collaboration, *Performance of the ATLAS track reconstruction algorithms in dense environments in LHC Run 2*, Eur. Phys. J. C **77** (2017) 673, arXiv: `1704.07983 [hep-ex]` (cit. on p. 39).

[91] R. Frühwirth, *Application of Kalman filtering to track and vertex fitting*, Nuclear Instruments and Methods in Physics Research Section A: Accelerators, Spectrometers, Detectors and Associated Equipment **262** (1987) 444, ISSN: 0168-9002, URL: `https://www.sciencedirect.com/science/article/pii/0168900287908874` (cit. on p. 39).

[92] ATLAS Collaboration, *Topological cell clustering in the ATLAS calorimeters and its performance in LHC Run 1*, Eur. Phys. J. C **77** (2017) 490, arXiv: `1603.02934 [hep-ex]` (cit. on p. 40).

[93] ATLAS Collaboration, *Jet energy scale and resolution measured in proton–proton collisions at $\sqrt{s} = 13$ TeV with the ATLAS detector*, Eur. Phys. J. C **81** (2020) 689, arXiv: `2007.02645 [hep-ex]` (cit. on pp. 40, 42).

[94] ATLAS Collaboration, *Jet energy scale measurements and their systematic uncertainties in proton–proton collisions at $\sqrt{s} = 13$ TeV with the ATLAS detector*, Phys. Rev. D **96** (2017) 072002, arXiv: `1703.09665 [hep-ex]` (cit. on pp. 41, 76).

[95] ATLAS Collaboration, *Determination of jet calibration and energy resolution in proton–proton collisions at $\sqrt{s} = 8$ TeV using the ATLAS detector*, Eur. Phys. J. C **80** (2020) 1104, arXiv: `1910.04482 [hep-ex]` (cit. on p. 42).

[96] A. Collaboration, *ATLAS flavour-tagging algorithms for the LHC Run 2 pp collision dataset*, (2022) (cit. on p. 42).

[97] ATLAS Collaboration, *Optimisation and performance studies of the ATLAS b-tagging algorithms for the 2017-18 LHC run*, ATL-PHYS-PUB-2017-013, 2017, URL: `https://cds.cern.ch/record/2273281` (cit. on p. 42).

[98] ATLAS Collaboration, *Electron efficiency measurements with the ATLAS detector using the 2015 LHC proton–proton collision data*, ATLAS-CONF-2016-024, 2016, URL: `https://cds.cern.ch/record/2157687` (cit. on p. 43).

[99] ATLAS Collaboration, *Electron reconstruction and identification in the ATLAS experiment using the 2015 and 2016 LHC proton–proton collision data at* $\sqrt{s} = 13\,TeV$, Eur. Phys. J. C **79** (2019) 639, arXiv: `1902.04655 [hep-ex]` (cit. on pp. 43, 76).

[100] ATLAS Collaboration, *Muon reconstruction performance of the ATLAS detector in proton–proton collision data at* $\sqrt{s} = 13\,TeV$, Eur. Phys. J. C **76** (2016) 292, arXiv: `1603.05598 [hep-ex]` (cit. on pp. 44, 76).

[101] ATLAS Collaboration, *Muon reconstruction and identification efficiency in ATLAS using the full Run 2 pp collision data set at* $\sqrt{s} = 13\,TeV$, Eur. Phys. J. C **81** (2021) 578, arXiv: `2012.00578 [hep-ex]` (cit. on p. 44).

[102] ATLAS Collaboration, *Measurement of the photon identification efficiencies with the ATLAS detector using LHC Run-1 data*, Eur. Phys. J. C **76** (2016) 666, arXiv: `1606.01813 [hep-ex]` (cit. on p. 45).

[103] ATLAS Collaboration, *Measurement of the photon identification efficiencies with the ATLAS detector using LHC Run 2 data collected in 2015 and 2016*, Eur. Phys. J. C **79** (2019) 205, arXiv: `1810.05087 [hep-ex]` (cit. on p. 45).

[104] ATLAS Collaboration, *Photon identification in 2015 ATLAS data*, ATL-PHYS-PUB-2016-014, 2016, URL: `https://cds.cern.ch/record/2203125` (cit. on p. 45).

[105] ATLAS Collaboration, *Performance of missing transverse momentum reconstruction with the ATLAS detector using proton–proton collisions at* $\sqrt{s} = 13\,TeV$, Eur. Phys. J. C **78** (2018) 903, arXiv: `1802.08168 [hep-ex]` (cit. on pp. 47, 76).

[106] ATLAS Collaboration, *Jet reclustering and close-by effects in ATLAS Run 2*, ATLAS-CONF-2017-062, 2017, URL: `https://cds.cern.ch/record/2275649` (cit. on p. 47).

[107] M. Baak et al., *HistFitter software framework for statistical data analysis*, Eur. Phys. J. C **75** (2015) 153, arXiv: `1410.1280 [hep-ex]` (cit. on p. 73).

[108] G. Cowan, K. Cranmer, E. Gross and O. Vitells, *Asymptotic formula for likelihood-based tests of new physics*, The European Physical Journal C **71** (2011), ISSN: 1434-6052, URL: `http://dx.doi.org/10.1140/epjc/s10052-011-1554-0` (cit. on p. 75).

[109] A. L. Read, *Presentation of search results: the* CL_S *technique*, J. Phys. G **28** (2002) 2693 (cit. on p. 75).

[110] ATLAS Collaboration, *Tagging and suppression of pileup jets with the ATLAS detector*, ATLAS-CONF-2014-018, 2014, URL: `https://cds.cern.ch/record/1700870` (cit. on p. 76).

[111] A. Buckley, H. Hoeth, H. Lacker, H. Schulz and J. E. von Seggern, *Systematic event generator tuning for the LHC*, The European Physical Journal C **65** (2009) 331, URL: `https://doi.org/10.1140%5C%2Fepjc%5C%2Fs10052-009-1196-7` (cit. on p. 78).

[112] N. Themistokleous, E. Carquin Lopez, B. M. Wynne and C. Leonidopoulos, *Search for heavy Majorana or Dirac neutrinos and right-handed W gauge bosons in final states with two charged leptons and two jets at sqrt(s)=13 TeV with the ATLAS collaboration*, tech. rep., Internal note for the resolved channel of the ATLAS Heavy Neutrino analysis: CERN, 2021, URL: `https://cds.cern.ch/record/2779297` (cit. on p. 100).

[113] G. Aad et al., *Search for new resonances in mass distributions of jet pairs using 139 fb*$^{-1}$ *of* pp *collisions at* $\sqrt{s} = 13$ *TeV with the ATLAS detector*, JHEP **03** (2020) 145, arXiv: `1910.08447 [hep-ex]` (cit. on pp. 98, 102).